



POLITECNICO
MILANO 1863

SCUOLA DI INGEGNERIA INDUSTRIALE
E DELL'INFORMAZIONE

Jet fragmentation models review, with focus on SAMPSON code numerical investigation against FARO L-14 experiment

TESI DI LAUREA MAGISTRALE IN
NUCLEAR ENGINEERING-INGEGNERIA NUCLEARE

Author: Francesca Longhi

Student ID: 863410
Advisor: Antonio Cammi
Academic Year: 2020-21

Ai miei genitori,
una lanterna luminosa
nelle giornate buie.
Grazie.

Abstract

Following Fukushima severe accident, extensive investigation of event progression was needed to understand underlying phenomena, also employing useful tools such as nuclear severe accident computer codes including ASTEC, MELCOR, MAAP and SAMPSON. The focus of this dissertation relies on the latter, involving a numerical investigation of jet fragmentation model implemented in the code in order to explain pressurization peaks observed during Fukushima accident after core meltdown. Jet fragmentation mechanism is a fundamental event in the framework of fuel-coolant interaction: many studies were conducted to address this issue, focusing on several phenomena involved. Main effects include hydrodynamic and thermal effects, the former regarding Rayleigh-Taylor instabilities at jet leading edge and Kelvin-Helmholtz instabilities at jet column surface, whilst the latter includes boiling effects involving vapor film development at the fuel-coolant interface, internal pressurization effects concerning coolant entrapment in the molten phase and solidification effects during cooling due to thermal stresses. A complete agreement on one definite model, of which Epstein-Fauske and Kim-Corradini are the most accredited ones, has not been reached because of the complexity of the phenomena. Many experiments were performed in order to evaluate models' validity, among which FARO L-14 experiment accomplished at JRC Ispra was selected in order to achieve a numerical investigation of SAMPSON jet fragmentation model, involving DCA and THA modules. Implementation of FARO geometry and experimental conditions were accomplished, followed by DCA and THA stand-alone analysis and coupling essential steps, leading to jet fragmentation model analysis. Unluckily the implemented model was inconsistent with respect to the one presented in the manual: a trivial implementation of the manual model was carried out, leading to a pressure underestimation. A more complex implementation strategy was proposed and fulfilled, leading to a slight overestimation of pressure, coherent with the hypothesis initially made. Further developments may take advantage of implementation improvement, considering essential jet breakup length parameter, as well as integration of more complex models describing crucial phenomena i.e., Kelvin-Helmholtz instabilities, such as the already validated one included in VESUVIUS steam explosions dedicated code.

Estratto in lingua italiana

A seguito dell'incidente di Fukushima, è stata necessaria un'ampia indagine sulla progressione dell'evento per comprendere i fenomeni coinvolti, utilizzando strumenti come i codici informatici per gli incidenti nucleari gravi, tra cui ASTEC, MELCOR, MAAP e SAMPSON. Il focus di questa tesi si basa su quest'ultimo, coinvolgendo un'indagine numerica del modello di frammentazione del getto implementato nel codice, al fine di spiegare i picchi di pressurizzazione osservati durante l'incidente di Fukushima dopo la fusione del nocciolo. Il meccanismo di frammentazione è un fenomeno fondamentale durante l'interazione combustibile-refrigerante: molti studi sono stati condotti per affrontare questo problema, concentrandosi sui diversi fenomeni coinvolti. Gli effetti principali includono quelli idrodinamici e termici, i primi riguardanti le instabilità di Rayleigh-Taylor sulla testa del getto e le instabilità di Kelvin-Helmholtz sulla superficie laterale del getto, mentre i secondi includono effetti di ebollizione che coinvolgono lo sviluppo di un film di vapore all'interfaccia combustibile-refrigerante, effetti di pressurizzazione interna che riguardano l'intrappolamento del refrigerante nella fase fusa, ed effetti di solidificazione dovuti a stress termici. Un accordo su un modello unico, tra cui Epstein-Fauske e Kim-Corradini sono i più accreditati, non è stato raggiunto a causa della complessità del fenomeno. Molti esperimenti sono stati eseguiti per valutare la validità dei modelli, tra cui l'esperimento FARO L-14 realizzato al JRC di Ispra, selezionato per lo studio sul modello di frammentazione SAMPSON coinvolgendo i moduli DCA e THA. L'implementazione della geometria e delle condizioni sperimentali di FARO sono state realizzate, seguite dalle fasi di singola analisi e accoppiamento di DCA e THA, portando all'analisi del modello di frammentazione. Il modello implementato è risultato incoerente rispetto a quello presentato nel manuale: una banale implementazione è stata effettuata, portando ad una sottostima della pressione. Una strategia di implementazione più complessa è stata proposta e realizzata, portando ad una leggera sovrastima della pressione, coerente con le ipotesi fatte. Ulteriori sviluppi trarranno vantaggio da migliorie di implementazione, considerando la lunghezza di rottura del getto, così come l'integrazione di modelli più complessi che descrivono fenomeni cruciali come le instabilità di Kelvin-Helmholtz, come ad esempio quello già validato ed incluso nel codice VESUVIUS dedicato alle esplosioni di vapore.

Contents

Abstract	i
Estratto in lingua italiana	iii
Contents	v
1. Introduction	1
1.1 Background.....	1
1.2 Nuclear reactor safety	3
1.2.1 Defence in Depth	4
1.2.2 Design by Basis Accident	7
1.3 Severe accident.....	8
1.3.1 Core heat up	8
1.3.2 Core melt.....	9
1.3.3 Debris relocation and jet breakup process.....	10
1.4 Simulation codes.....	11
1.4.1 MELCOR.....	12
1.4.2 ASTEC	16
1.4.3 MAAP.....	22
1.4.4 SAMPSON	23
1.4.5 Integral codes comparison	24
1.5 Validation of integral codes	26
2. Jet Fragmentation models	31
2.1 Introduction.....	31
2.2 FCI global process.....	32
2.3 Fragmentation regimes	34
2.3.1 Jet breakup length	37
2.4 Fragmentation mechanisms and models.....	42

2.4.1	Hydrodynamic effects	42
2.4.2	Thermal effects.....	48
2.4.3	Accredited models.....	57
2.5	Concluding remarks	64
3.	SAMPSON CODE.....	67
3.1	Introduction.....	67
3.2	SAMPSON code.....	67
3.3	SAMPSON modules.....	69
3.3.1	FPTA.....	71
3.3.2	FPRA.....	72
3.3.3	FRHA.....	73
3.3.4	MCRA.....	74
3.3.5	THA	75
3.3.6	DCA.....	77
3.3.7	DSA – DCRA.....	78
3.3.8	CVPA.....	80
3.4	Concluding remarks	81
4.	FARO L-14 EXPERIMENT.....	83
4.1	Introduction.....	83
4.2	Jet fragmentation experiments.....	83
4.3	FARO tests	87
4.3.1	FARO test facility	89
4.3.2	FARO L.14	94
4.4	Concluding remarks.....	100
5.	IAE jet fragmentation model numerical investigation.....	103
5.1	Introduction.....	103
5.2	DCA stand-alone analysis	104
5.2.1	DCA model overview	104
5.2.2	FARO L-14 geometry and boundary conditions implementation	106
5.2.3	DCA stand-alone results and discussion	110
5.3	THA stand-alone analysis	114

5.3.1	THA module overview	114
5.3.2	FARO L-14 geometry and boundary conditions implementation	115
5.3.3	THA stand-alone results and discussion	119
5.4	DCA-THA coupling without fragmentation model.....	121
5.4.1	DCA – THA coupling results and discussion	121
5.5	DCA – THA coupling with fragmentation model	130
5.5.1	IAE jet fragmentation model	130
5.5.2	Fragmentation model results and discussion.....	138
5.5.3	Implementation strategy proposed for IAE jet fragmentation model.....	143
5.5.4	Comparison with VESUVIUS steam explosions dedicated code.....	146
5.5.5	Concluding remarks.....	149
6.	Conclusions and future developments	153
	Bibliography.....	159
	List of Figures.....	167
	List of Tables	171
	List of Symbols	173
	List of Acronyms.....	177
	Ringraziamenti.....	183

1. Introduction

1.1 Background

On March 11th 2011, an high magnitude earthquake followed by tsunami struck Japanese east coast, impacting on Fukushima Daiichi nuclear power plant causing TEPCO's station blackout and consequent nuclear severe accident. Investigation for damage extent also in terms of decommissioning is a critical task, such that simulation of this incident by means of computer codes for severe accidents is essential not only for estimation and comprehension of plant state, but also for benchmark studies and future safety systems development. Just after Fukushima events, IAE (Institute of Applied Energy) based in Tokyo Japan began working on SAMPSON modular code, developed in 1990s, for TEPCO's nuclear power plant investigation in terms of reactors state assessment and following decommissioning.

In this framework, the present dissertation aims at analyzing a specific event during core meltdown regarding melted material discharge into lower head: jet breakup and fuel-coolant interaction is a fundamental phenomenon for accident progression understanding. In fact, as shown in figure 1.1, calculations using SAMPSON code for unit 3 were not able to reproduce pressure spikes during debris slumping into lower head. This incapability of SAMPSON simulation of rapid pressurization both in reactor pressure vessel RPV and containment can be explained by lack of debris fragmentation model treatment.

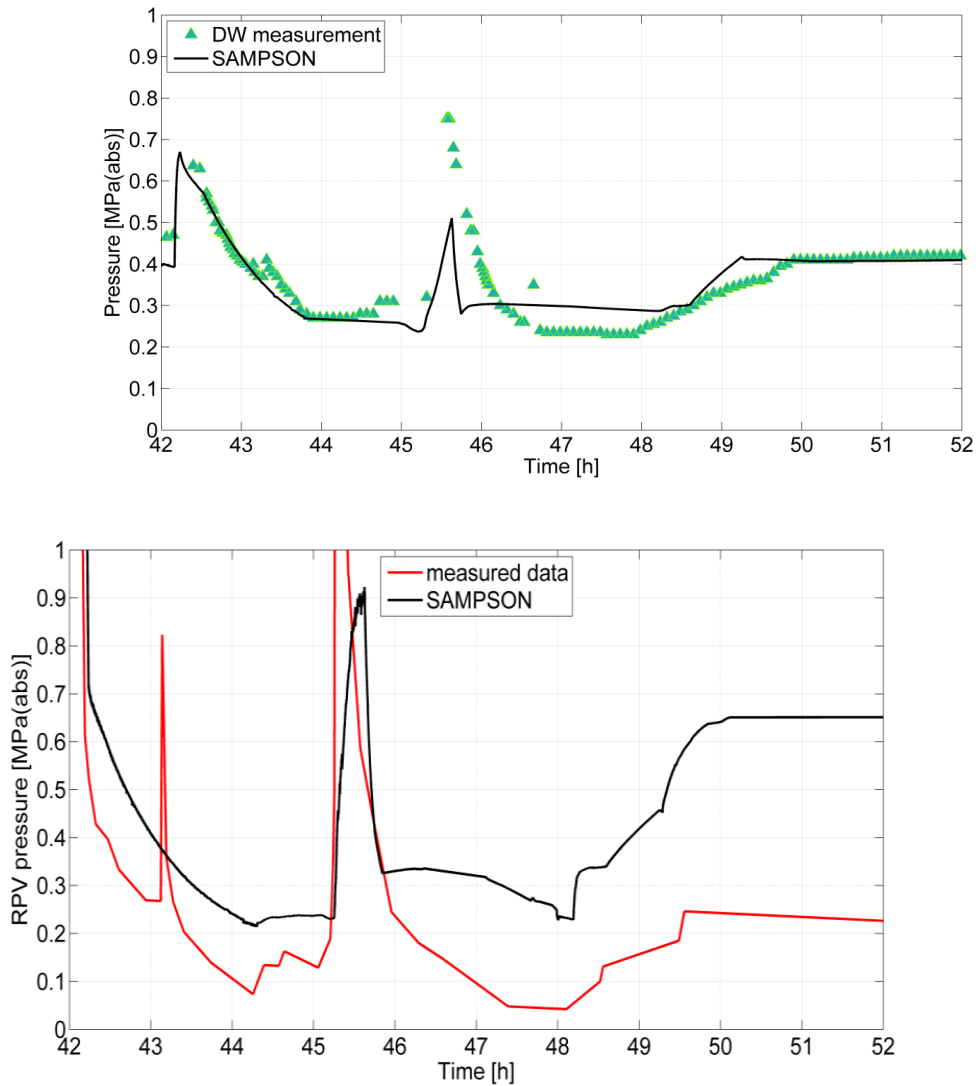


Figure 1.1: SAMPSON simulations without fragmentation model compared to experimental data

This model, which could explain such pressurization in terms of higher heat exchange surface and void creation, was already implemented in SAMPSON but not used for simulation due to lack of numerical verification and validation. In this framework, the objective of this study is IAE jet breakup model investigation using SAMPSON code and comparison with literature models.

In the first part of the present chapter, a brief overview of nuclear safety philosophies will be presented, leading to severe accident definition and description, focusing on issues related to corium discharge in the lower head. Following Three Mile Island (TMI) accident, need for severe accident simulation codes was evident resulting in several computer code development such as MELCOR, MAAP, ASTEC and SAMPSON: a description and comparison of codes will be carried out, pointing out the necessity of validation against experimental works such as KROTOS, FARO, LIVE, OLHF, CORA, OECD: a brief summary of these will be presented at the end of this chapter.

1.2 Nuclear reactor safety

Nuclear safety objective is ensuring plant site, environmental and public health protection from any radiation hazard by means of safety systems, plant management and radiation shielding following ALARP (As Low As Reasonably Possible) principle during both normal operation and accident scenario. Safety regulations have their roots in deterministic and probabilistic approaches: the former concerning conservative calculations and best estimations, whilst the latter dealing with sensitivity studies and risk analysis, both having plant integrity and severe accident avoidance as final goal. Due to its complexity, severe accident phenomenon entails several intertwined disciplines including neutronic physics, material science, thermal hydraulics, chemistry, risk assessment, structural and thermo mechanics hence, a fundamental issue is the safety approach adopted during reactor design, testing and operation. Regarding deterministic philosophies, two main complementary branches

can be distinguished: defence in depth approach and safety design by basis accident, the latter paving the way to nuclear accident definition.

1.2.1 Defence in Depth

Defence in depth exploits the concept of multi-barrier approach and redundancy, employing different levels of equipment and procedures to sustain physical barriers effectiveness between radioactive material and the external environment. [1] This approach guarantees safety against a wide spectrum of events, by means of four physical barriers and five hierarchic levels of defense.

The former are actual protective barriers, whose objective is preventing release of radioactive substances under any circumstances as shown in figure 1.2. They can be divided in:

1. Fuel matrix and cladding, preventing fission gases release;
2. Boundary of reactor coolant system, containing reactor pressure vessel and primary circuit in order to confine fission product escaped from fuel and cladding;
3. Containment building, mainly for prevention and mitigation of nuclear material release to the environment in case of a severe accident.

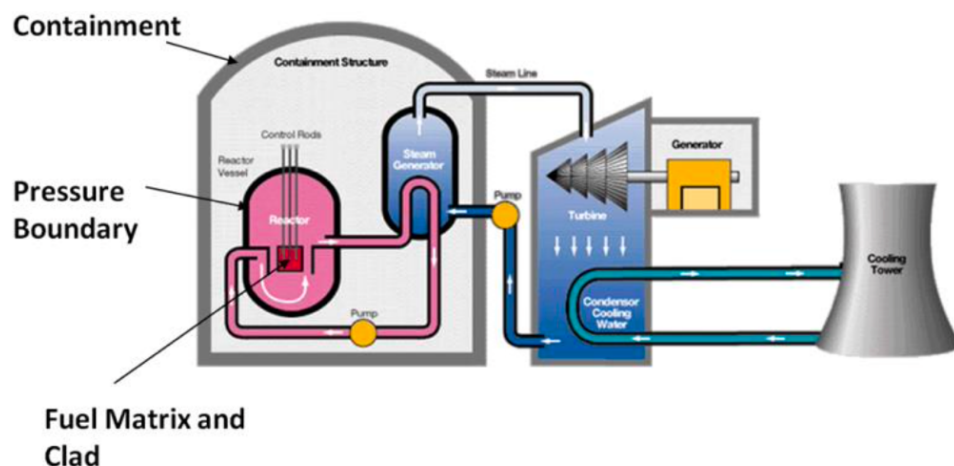


Figure 1.2: physical barriers for a typical nuclear reactor configuration

As already mentioned, defence in depth has a layered structure such that in case of one level failing the subsequent one becomes operative. Five steps in means of prevention, control, mitigation and response are the key features for nuclear reactor defence in depth: a brief overview is reported in table 1.1

Table 1.1: Defence in depth levels

Level	Objective	Main measure
1	Prevention of abnormal operation and failures	Conservative design and high quality standards during construction and operation

2	Control of abnormal operation and detection of failures	Control, limiting and protection systems and other surveillance features
3	Control of accidents within the design basis	Engineered safety features and accident procedures
4	Control of severe plant conditions, including prevention of accident progression and mitigation of the consequences of severe accidents	Complementary measures and accident management
5	Mitigation of radiological consequences following significant releases of radioactive materials	Off-site emergency response

The first level addresses to prevention by means of in-plant design features: negative feedback coefficients for inherent safety and safety margins, reliable materials, high quality components and instrumentation are some examples.

The second level incorporates plant features in order to have control on abnormal behavior which may occur during plant operation and restore normal operating mode. Despite prevention and surveillance, accidents may occur in which case level 3 comes into play, preventing accident conditions worsening and evolution: redundancy is a key feature, aiming at maintaining physical barriers integrity and effectiveness. An equipment example could be the emergency core cooling system (ECCS) in case of loss

of coolant accident (LOCA) preventing core damage. Furthermore, procedures and instrumentation are needed to handle situations not covered by the first three levels, minimizing the risk of an unlikely accident event in terms of magnitude and radioactive material release while also managing the course of the event by means of plant status analysis, heat removal control and core deterioration delay. In case all the above efforts prove insufficient to ensure plant integrity, mitigation of consequences and radioactive release by off-site authorities and organizations are necessary.

1.2.2 Design by Basis Accident

Design by basis accident (DBA) approach refers to the worst possible case scenario regard to which nuclear plants must be designed and built without loss of structural and components integrity to ensure environmental and public safety. In Light Water Reactors (LWR), large LOCA is the typical condition assumed [2], concerning a two-side break in the primary system largest pipe, resulting in reactor core uncovering in very short time; hence, large amount of water is required to prevent core heat up and to provide cooling, resulting in the ECCS system turning on.

LOCA is the reference condition for LWR, even if other transients are taken into account in the DBA such as decrease in coolant mass flow rate, reactivity anomalies and heat removal increase in the secondary system. All of these transients affect the reactor state, resulting in core heat up and eventually its degradation, leading to undesired accident events against which the plant must be able to respond and overcome.

1.3 Severe accident

Severe accidents are defined as those involving at least an initial core damage due to regulatory fuel limits overcoming, leading to IAEA (International Atomic Energy Agency) definition for severe accident: “certain very low probability plant states, that are beyond design basis accident conditions and which may arise owing to multiple failures of safety systems leading to significant core degradation that may jeopardize the integrity of many or all of the barriers to the release of radioactive material”. [3] As already mentioned in paragraph 1.2.2, loss of coolant inventory is the primary cause of core heat up, being the core uncovered leading eventually to failing, hence melting.

1.3.1 Core heat up

In case of coolant loss, film boiling can occur at fuel-cladding surface, leading to rapid clad temperature increase and heat transfer lowering between fuel rods and steam. Hence, fuel temperature increases and zircaloy oxidation phenomena can occur with consequent hydrogen formation, contributing to core heat up and loss of core geometry and integrity.

At early heating up stage concerning temperature range between 1200 K - 1400 K, geometric phenomena such as clad ballooning and embrittlement can take place, as well as chemical ones which may lead to local temperature escalation due to exothermic oxidation reaction within the core. [4]

1.3.2 Core melt

LWR composition is very diversified, such that melting phenomena may occur in many different ways depending on materials and chemical structures involved, mainly UO_2 , Zircaloy, stainless steel and Al_2O_3 as burnable poison. Regarding heat up rates of 1K/s, Hoffmann [5] distinguishes three main temperature regimes involving different processes leading to liquid phase formation, summarized in figure 1.3. The first temperature regime ranges between 1473 K and 1673 K, in which structural components may form liquid phases, relocate and obstruct coolant flow, advancing core heat up so further melting takes place. Given its relatively low melting temperature (about 1073 K), Ag-In-Cd alloy is the first compound subjected to melting; its liquid phase could interact with zircaloy causing its dissolution, resulting in local core damage even below zircaloy melting temperature (about 2033 K). [6] Furthermore, contact between zircaloy and INCONEL stainless steel may happen, causing fuel rods early-melt progression starting from 1473 K.

The second temperature regime ranges between 2033 K and 2273 K, regarding extended core damage due to unoxidized zircaloy melting and relocation along fuel rods. In case of cladding oxide layer mechanical failure or dissolution, molten zircaloy may dissolve part of the UO_2 fuel pellet, such that 'candling' process of U, Zr, O may happen, consisting in molten ternary mixture flow from upper core region at high temperature to lower regions at low temperature. Solidification may happen in lower regions, as well as remelting due to decay heat released from the mixture. At last, the third temperature regime ranges between 2873 K and 3123 K, concerning a complete core meltdown and collapse.

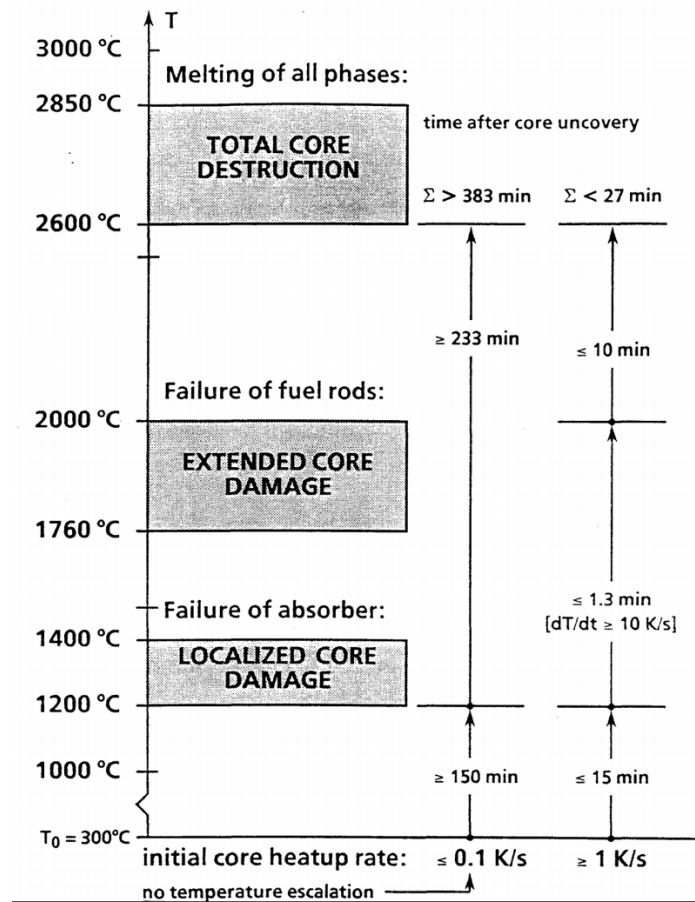


Figure 1.3: Temperature regimes for core meltdown

1.3.3 Debris relocation and jet breakup process

After core melting onset, molten materials start relocating into the lower head and begin cooling. Gravity-driven relocation and molten material cooling and solidification involve several complex thermal hydraulic phenomena regarding debris interaction with the lower head depending on water level inside the lower plenum, heat transfer during fuel-coolant interaction (FCI), steam spikes, steam explosions, debris quenching and molten jet breakup process.

Jet breakup process is a significant phenomenon during debris relocation, being a critical and complex event during FCI, involving two simultaneous events from hydrodynamic and thermal point of view [7]. The former regards interfacial instabilities at corium-water interface, stripping and liquid entrainment, whilst the latter takes into account solidification and remelting possibilities after crust formation. Among many parameters influencing jet breakup, molten mass and falling position are extremely significant ones having a direct influence on the jet breakup length, which refers to the distance between the lower plenum coolant surface and the location in which coherent melt jet no longer exists due to fragmentation. Being jet impingement on vessel inner structure one possible cause of RPV lower head failure, jet breakup length quantity importance is easily retrieved.

Jet fragmentation is a complicated phenomenon still under investigation: many numerical models have been proposed, as well as many experiments performed both on small and big scale regarding molten corium discharge, breakup and quench. A detailed discussion about fragmentation models will be addressed in chapter 2, whilst a brief review of experimental works can be found in section 1.5.

1.4 Simulation codes

Three Mile Island TMI-2 severe accident event induced the scientific community to develop computational codes for accident scenarios simulation, at first in the USA in the 80's and afterwards in Europe and Japan.

Three main codes classes are defined, based on the investigation scope:

- Integral codes, able to simulate the overall NPP using integrated models, both physical and parametric, for accident progression analysis. This category includes MELCOR, MAAP, ASTEC, SAMPSON.
- Mechanistic codes, constituted by best estimates models providing a detailed insight of accident progression, are able to simulate just one part of the plant due to their high computational time: an example is SCDAP/RELAP5, implemented in SAMPSON integrated modular code to provide for RCS and thermal hydraulic calculations.
- Dedicated codes, aiming at single phenomenon simulation.

Following TMI-2 accident, in the integral codes framework, two codes were developed in the USA: MAAP owned by EPRI and MELCOR advanced by the USNRC in the 80's. Later in years, also Europe and Japan followed the same path, proposing ASTEC and SAMPSON. A brief comparison between abovementioned codes will be given below, highlighting differences and common features. A complete description of SAMPSON code can be found in chapter 3.

1.4.1 MELCOR

MELCOR is a fully integrated, relatively fast-running code that models the progression of severe accidents in light water reactor nuclear power plants. [8] Developed by Sandia National Laboratories USA as modular engineering-level computer code, MELCOR is able to simulate a wide range of phenomena during severe accident progression in LWR: at first envisioned as parametric, during the years improvement concerning phenomenological models' implementation have been made to reduce uncertainties and tuning parameters. [9]

MELCOR is constituted by sixteen modules, coupled together in order to simulate overall NPP behavior giving a coherent modular structure, each one aiming at a single phenomenon or physical behavior treatment with a control volume approach. Main modules take into account thermal hydraulics of primary coolant loop, vessel and containment, core uncovering and following occurrences such as fuel rod heat up, cladding oxidation, loss of integrity, core relocation and RPV failure, hydrogen production, release, transport, and combustion, fission products release, behavior of radioactive aerosol in containment building and impact of safety features on thermal hydraulic and radionuclide behavior. [10]

A summary of each module objective is reported in table 1.2

Table 1.2: defence in depth levels

MODULE	OBJECTIVE
Accumulator (ACC)	Sub packages of Engineered Safety Features ESF, regarding liquid injection by an accumulator specified by user.
Burn (BUR)	Combustion of gas in control volumes based on global deflagration models, not considering actual reaction kinetics and flame front propagation.
Cavity (CAV)	Molten material attack on concrete basement, including heat transfer calculations, cavity geometry changes due to ablation and gas generation. Coupled with COR, CVH, FDI.

Condenser (CND)	Sub package of ESF, takes into account Isolation Condenser System (ICS) and Passive Containment Cooling System (PCCS) linked to heat exchangers submerged in water.
Core (COR)	Includes molten core relocation phenomena, computing thermal response of both core and lower head during debris slumping and molten pool growth up to RPV failure. Coupled with CVH and HS for heat transfer and molten mass relocation models calculations.
Control volume hydrodynamics flow path (CVH/FL)	Two models regarding thermal-hydraulic modeling of coolant liquid and gas. CVH concerns control volumes, whilst FL deals with junction and connections. Every change in thermal-hydraulic aspects in other modules is taken as input in CVH/FL, to update plant state.
Control volume thermodynamic flow path (CVT)	Aims at state equations and thermodynamic properties computation for hydrodynamic materials, by means of equilibrium or non-equilibrium thermodynamics.
Decay heat (DCH)	Models decay heat power generated by fission products in RPV and cavity, both for aerosol suspended or deposited, not treating decay chain for each radionuclide which would result in excessive computational burden.

Fan cooler (FCL)	Included in ESF, computes heat and mass transfer due to fan cooler (large heat exchanger used to remove heat from containment building) operation.
Fuel dispersal (FDI)	Describes debris behavior in containment until its deposition in cavity modeled by CAV module. Two main phenomena are considered: low-pressure and high-pressure fuel ejection from reactor vessel. Steam explosions and fission product release from debris are not yet implemented.
Heat structures (HS)	Is dedicated to heat conduction and energy transfer analysis within solid structures and boundary surfaces i.e., pressure vessel inner walls, containment structures and fuel rods.
Material properties (MP)	By means of physical laws, correlations and tables, structural and fuel material properties needed by other modules are elaborated in terms of thermodynamic state and transport properties. Furthermore, it allows new materials recording through user manual input.
Non-condensable gas NCG	Modeling of non-condensable gases as ideal gases by state equations and constitutive relations is provided in this module.
Passive Autocatalytic	Sub package of ESF, working on hydrogen removal rate from hydrogen recombiners, in order to keep its

Hydrogen Recombiner (PAR)	concentration level under control to avoid deflagration or even detonation.
RadioNuclide (RN)	Evaluates fission products, aerosol and vapors behavior derived by fuel and molten debris, their deposition and transport through flow paths and removal from ESF.
Containment Sprays (SPR)	Model capabilities concern heat and mass transfer between spray water droplets and containment atmosphere.

1.4.2 ASTEC

Accident Source Term Evaluation Code ASTEC is an integral code developed since 1996 by French IRSN (Institut de Radioprotection et de Sûreté Nucléaire) and German GRS (Global Research for Safety) in the SARNET European framework, progressively paving its way as European reference code. During the years ASTEC has been under constant improvement, in order to implement models derived by experimental works from all over the world, i.e. PHÉBUS FP experimental program for fission products, giving ASTEC its peculiar feature of high-quality modelling for radioactive products behavior. [2]

On the heels of this, a new version of the ASTEC was released in 2009 including a mechanistic core degradation model concerning 2D molten debris relocation within lower plenum, vessel external cooling model for in-vessel debris retention and

improvement of chemical gas kinetics model for RCS. ASTEC modular structure is defined by 13 modules, each one simulating different part of NPP or severe accident phenomena. An overlook of ASTEC structure is reported in figure 1.4

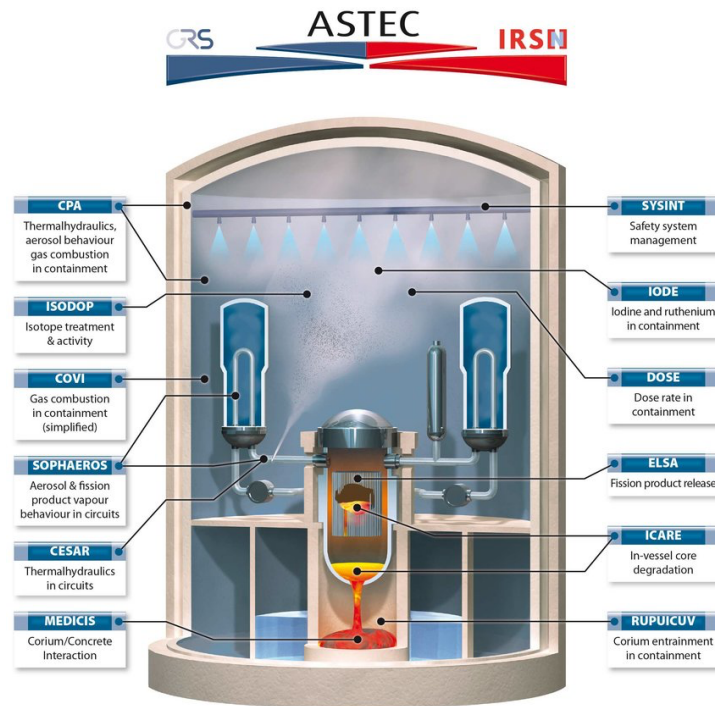


Figure 1.4: ASTEC modular structure

Unlike MELCOR's single module for thermal hydraulic calculations for the overall NPP, ASTEC uses different modules for thermal hydraulic simulations depending on the kind of structure in analysis i.e., CESAR develops analysis for primary and secondary circuits, CPA works in the containment framework and ICARE concerns reactor core region in terms of in vessel degradation and thermal hydraulics progression.

On the other hand, ASTEC's CPA and MELCOR's CVH/FL shares the same control volumes and junction approach, subdividing volume contents in water pool (liquid

subcooled or two-phase saturated) and atmospheric containment gas, using two thermodynamic state options of equilibrium or non-equilibrium. [9] While sharing the same control volumes and junction nodalization reported in figure 1.5, junction transport differs in the two codes: water and gas phase junctions are separated in ASTEC, whilst MELCOR is able to transport both phases at the same time. A concise explanation of ASTEC modules' objective is reported in table 1.3

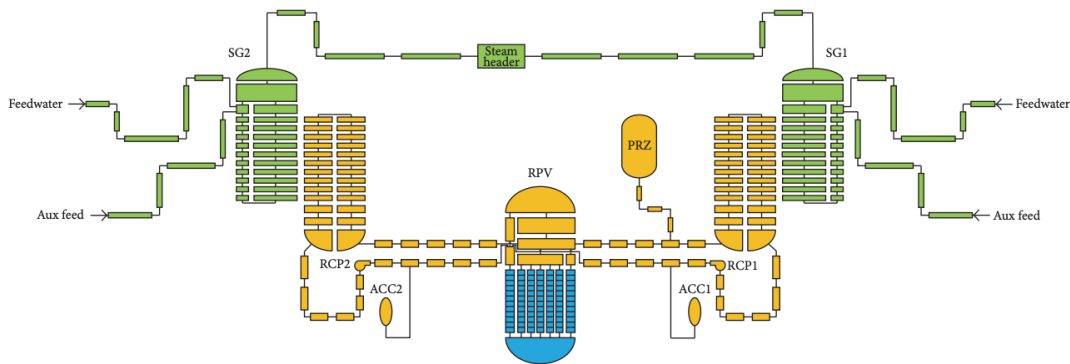


Figure 1.5: ASTEC and MELCOR simplified nodalization for primary and secondary circuits

Table 1.3: ASTEC modules overview

MODULE	OBJECTIVE
CESARS	<p>Thermal hydraulic analysis in primary and secondary circuits and RPV up to core degradation initiation, by means of a two-fluid and five-equations method. [11]</p> <p>Physical laws implemented follows correlations used in CATHARE2, a best estimate French code for thermal hydraulics analysis, pursuing calculation with finite volume method.</p>
ICARE	<p>Simulation of core degradation starting from early stages of rod heat up, ballooning and burst, up to late degradation concerning corium slumping and RPV failure. Includes several models for thermal hydraulics, heat transfer, FP power generation, fuel rod mechanics such as ballooning and creep, Zr chemistry for oxidation, molten material relocation and jet fragmentation in water, lower head failure (both for mechanical and thermodynamical failure) and corium slumping into cavity. [12]</p>
ELSA	<p>Aims at FP release simulation as well as structural material analysis from damaged core by linking with ICARE. Fission products release concerns both fuel rods and debris bed accumulated in the lower head, describing their behavior distinguishing three main categories: volatile, semi-volatile and low volatiles.</p>

SOPHAEROS	Reproduces fission products and aerosol transport in RCS to the containment, differentiating twelve families of compounds and five states regarding suspension, condensation and deposition.
RUPUICUV	Regards ex-vessel phenomena of molten material discharge into cavity after RPV failure, simulating containment heating due to direct contact with corium, subsequent oxidation and droplets entrainment by gas into containment atmosphere.
CORIUM	Strictly related to RUPUICUV, is a parametric model used to simulate corium droplet transport behavior by gasses.
MEDICIS	MCCI (Molten Core Concrete Interaction) simulation using a 0D lumped parameter approach considering debris layers. Furthermore, water injection on debris pool is modeled, taking into account debris coolability.
CPA	Module assigned to containment analysis in terms of thermal hydraulics, FP and aerosol behavior. Control volumes containing the sump (liquid and gaseous phase) and atmosphere are used for the latter calculation, leaving equilibrium or non-equilibrium choice to user. Junctions connects control volume zones, distinguishing between drainage (transporting water including dispersed gases) and atmospheric

	(regarding gaseous state transporting water droplets) junctions.
IODE	As name suggests, this model is devoted to Iodine behavior simulation, focusing on 25 Iodine predominant reactions from a kinetic and chemical transformation point of view.
DOSE	Model not available for previous version of ASTEC, implemented in ASTEC new version V2.0 is able to predict dose rate for gas phase in the containment.
ISODOP	Dedicated to FP and actinides decay in various reactor zones such as core, RCS, containment and environment.
SYSINT	Easy simulation of engineered safety features is allowed for user, i.e., pressurizers, steam generators, containment sprays, H ₂ recombiners.
COVI	Dedicated to maximum built-up pressure value calculation resulting from hydrogen combustion in adiabatic conditions.

1.4.3 MAAP

MAAP modular code was originally developed in early '80s by Fauske and Associates in IDCOR (Industry Degraded Core Rulemaking) program framework advanced by EPRI, actual owner of the code.

MAAP is able to simulate LWR severe accident progression by implementation of many lumped parameters models and hundreds of subroutines falling in four [13] main categories:

- High level routines, including main program, input and output data storage and numerical integration routines.
- System and region routines, defining system status by means of flags in terms of energy and mass conservation in the considered volume.
- Phenomenological routines, regarding state variables change rates among volumes, can be defined as the code core.
- Property and utility routines, generating physical properties and performing mathematical computations.

MAAP's objective is the resolution of lumped parameter, non-linear, first order, coupled ordinary differential equations in time, mostly regarding mass and energy conservations, for sever accident simulation resulting in core degradation.

Many lumped parameter models for physical phenomena are included in the code regarding gas and water flow, as well as evaporation, condensation, boiling and heat transfer analysis, as well as phenomena modeling after core damage onset i.e., cladding oxidation hence hydrogen formation, fission products behavior, core relocation and debris dynamics in lower head and MCCI.

Given the lumped parameter and parametric nature of the code along with momentum

balance equations reduced to algebraic expressions by a quasi-steady analysis, MAAP is the fastest running among severe accident codes in terms of computational time, almost 10-100 times faster than ASTEC and MELCOR. [9] Containment model follows the same pattern as MELCOR and ASTEC implementing heat structures and control volumes nodalization connected by junctions; whilst containment model can be rearranged by user, primary and secondary circuits have a prefixed not-adjustable scheme as shown in figure 1.6

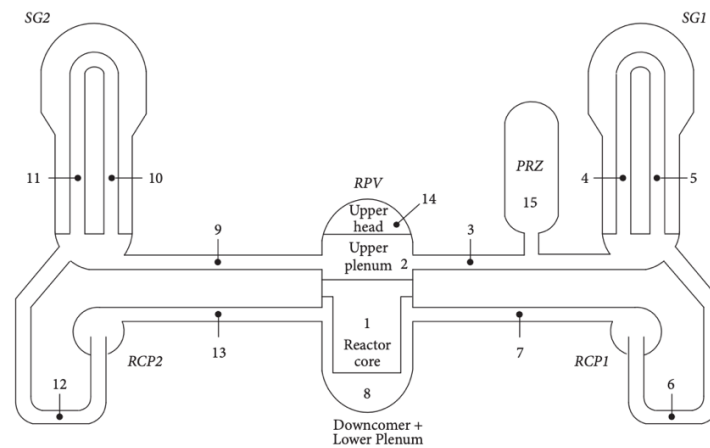


Figure 1.6: MAAP nodalization for primary circuit

1.4.4 SAMPSON

SAMPSON code was developed during the '90s by NUPEC (Nuclear Power Engineering Corporation) in IMPACT (Integrated Modular Plant Analysis and Computing Technology) Japanese project framework.

This integral code aims at modeling each phenomenon occurring during accident scenario as accurately as possible by means of mechanistic models implementation, integrating 11 modules describing accident progression. RELAP5/SCDAPSIM

mechanistic code was merged into SAMPSON for thermal hydraulic analysis, constituting THA (Thermal Hydraulic Analysis) module. SAMPSON, as other severe accident codes, also applies the concept of control volumes and junctions for primary and secondary system nodalization as shown in figure 2.5. On the other hand, in SAMPSON code every model implemented is purely mechanistic and very few parameters can be tuned by user. A complete and detailed description of SAMPSON code will be given in chapter 3.

1.4.5 Integral codes comparison

Integral codes portrayed in the previous section, show differences on many levels, concerning both phenomena modeling and computational time. At first, all severe accident codes shared a fast-running key feature in order to comply with low computational time performances. As computer technology progressed this issue was overcome in terms of computational capability increase, which led to a gradual development and extension of models' implementation in the codes: semi-mechanistic (phenomenological) and mechanistic models gradually replaced lumped parameter approaches, by an extent depending on the code [2].

Nevertheless, codes as MAAP maintained their original peculiar feature of fast-running simulations, whilst ASTEC and MELCOR share the same implementation philosophy of complexity expansion employing several mechanistic and phenomenological models; further complexity, hence less flexibility, is given in SAMPSON employing mechanistic models through the whole code, resulting in extensive computational time. It should be noted that computational efforts rely not only on the complexity of models implemented but also on the nodalization used for the overall simulation i.e., ASTEC employs same discretization meshes for core structure and thermal hydraulic analysis whilst MELCOR uses two different mesh

scale for core and thermal hydraulic discretization, resulting in longer computational times for the latter with respect to the former. In order to give a better comparison of these codes, an idea was to develop crosswalk benchmark studies on a single reference case i.e., Fukushima Daichii NPP: in this framework BASF project (Benchmark Study of the Accident of the Fukushima Daichii nuclear power station) was opened in 2012, gathering many research groups affiliations including ASTEC, MELCOR, MAAP and SAMPSON developers. Preliminary stages of this project reported main differences in simulation capabilities of the codes, especially involving thermal hydraulic treatment and core loss of integrity analysis. The former concerned momentum and energy conservation analysis, resulting in increasing modeling complexity starting from MAAP, solving a quasi-steady momentum balance thus reducing the problem to algebraic equation without differential equation employment, up to ASTEC, MELCOR, and SAMPSON involving a finite discretization for hydrodynamic equations using semi-implicit or implicit resolution methods. Regarding loss of integrity analysis, a key difference can be found in corium generation and slumping into the lower head: MELCOR assumes fuel rods melting and collapse in particulate debris after a given temperature range between 2000 and 2500 K is reached, resulting in a subsequent failure of core plate and slumping of both continuum molten material and particulate into the lower head, whilst on the other hand ASTEC, quite similarly to SAMPSON, does not take into account fuel rods collapse into debris, considering a direct melt of core structure and core plate leading to a molten pool generation. A similar approach is used in MAAP considering jet relocation into lower head forming a molten pool. Nonetheless, SAMPSON differs in the treatment of debris spreading analysis, concerning a debris bed, crust, as well as particulate generation and molten pool treatment by means of a simplified Navier Stokes modeling employing SMAC resolution method [14]. A detailed description of code comparisons can be found in

the crosswalk benchmark studies involved in the BASF project, whilst a brief comparison can be found in table 1.4

Table 1.4: Severe accident codes comparison

	MELCOR	ASTEC	MAAP	SAMPSON
Developer	US NRC	IRSN	EPRI	NUPEC
Objective	Integral	Integral	Integral	Integral
User tuning parameters	few	many	many	none
Simulation time	Several times the real time	Several times the real time	2 hours for 24 hours real time	20 times the real time
Characteristics	Mechanistic and empirical	Mechanistic and empirical	lumped	mechanistic

1.5 Validation of integral codes

Numerical verification and validation are essential steps in code development, in order to ensure a precise and detailed replica of phenomena portrayed in mechanistic models employed for severe accident progression analysis. Even if TMI-2 and Fukushima scenarios were both engaged as benchmark study cases for code validation, data collected were not sufficient for overall plant response simulation: experimental investigations both on small and large scales are crucial stages in order to have a reliable and full-sized data set for goal achievement. Experimental campaigns differ by scope and scale of investigation, whether regarding a single

component failure and behavior or integral research. A summary of experimental inquiries can be found in table 1.5.

Table 1.5: Experimental programs for code validations

Physical process	Program name	Organization
Integral tests	<ul style="list-style-type: none"> ▪ Phébus FP ▪ LOFT-LP-FP2 ▪ TMI-2 accident ▪ Fukushima 	<ul style="list-style-type: none"> ▪ IRSN ▪ INEL
Fission product release	<ul style="list-style-type: none"> ▪ ORNL ▪ VERCORS 	<ul style="list-style-type: none"> ▪ ORNL ▪ CEA
Vessel mechanical failure	<ul style="list-style-type: none"> ▪ OLHF ▪ FOREVER 	<ul style="list-style-type: none"> ▪ SNL ▪ KHT
Core degradation and Fuel-coolant interaction FCI	<ul style="list-style-type: none"> ▪ CORA ▪ FARO ▪ KROTOS ▪ LIVE 	<ul style="list-style-type: none"> ▪ KIT ▪ JRC Ispra ▪ CEA ▪ KIT
Molten corium-concrete interaction MCCI	<ul style="list-style-type: none"> ▪ OECD-CCI ▪ BETA ▪ SWICSS 	<ul style="list-style-type: none"> ▪ ANL ▪ KIT ▪ SNL
	<ul style="list-style-type: none"> ▪ FALCON ▪ LACE 	<ul style="list-style-type: none"> ▪ AEAT ▪ INEL

Aerosol and vapors	▪ DEMONA	▪ Battelle
RCS thermal hydraulics	▪ BETHSY	▪ CEA
Containment thermal hydraulics	▪ NUPEC ▪ MISTRA ▪ VANAM	▪ NUPEC ▪ CEA ▪ Battelle

In this dissertation focus will be given to fuel-coolant interaction (FCI) regarding corium behavior in water, emphasizing molten jet breakup modeling while slumping into RPV lower head.

An in-depth description of FCI experiments will be carried out in chapter 4, focusing on FARO experiments used for IAE model numerical verification and validation attempt using SAMPSON code.

2. Jet Fragmentation models

2.1 Introduction

As addressed in chapter 1 concerning severe accident scenario, events of fuel coolant interaction may arise due to hot core molten material discharge into the lower head. Preliminary phases of mixing and the following sequence of events entail several complex phenomena: FCI was widely investigated by many researchers for many decades, but the scientific community is still unable to agree upon a complete model for molten fuel breakup in liquid phase due to intertwined phenomena and feedback effects leading to a challenging formulation of the problem. Nevertheless, some cornerstones concepts concerning mixing stages, breakup regimes, as well as instabilities responsible for molten fuel breakup governing the FCI global phenomena, are commonly accepted as main drivers by the scientific community and confirmed by extensive experimental campaigns performed by many institutions. In the first paragraph a global description of phenomena involved in the overall process will be discussed, followed by an in-depth analysis of breakup regimes identified based on Weber number and jet breakup length, highlight the influencing factors on the latter. Furthermore, in section 2.4 a description of breakup mechanism based on hydrodynamic instabilities and temperature effects will be shown, complemented by a cursory models overview. A more detailed description of accredited models will be finally given in section 2.5.

2.2 FCI global process

As mentioned in paragraph 2.1, the existence of cornerstones concerning the interaction between molten fuel and coolant pool can provide the basis for a global understanding of the process. In particular, it was found that the fragmentation mechanism of molten jet in the mixing phase can be classified in two main classes: hydrodynamic effects and thermal effects [15] which will be treated accurately in paragraph 2.4. The former relies on two main kinds of hydrodynamic instabilities for breakup process description: Rayleigh - Taylor instabilities (RTI) and Kelvin - Helmholtz instabilities (KHI), both acting in the premix phase, arising due to difference in relative velocity of corium and coolant.

RTI play a key role on the head of the jet during penetration phase, in which the stagnation pressure due to coolant displacement must be overcome, such that instabilities may arise at leading edge resulting in fragmentation of the jet head. On the other hand, KHI may occur on the side of the jet away from leading jet head due to shear forces resulting from different velocity profiles for melt and coolant: rising oscillations on jet body may lead to side layer stripping, translating the problem from continuum jet analysis to single molten droplet investigation. Furthermore, fuel drops may additionally undergo the same KHI process resulting in finer corium.

Concerning thermal interaction, the general accredited mechanism addresses heat transfer mechanism via film boiling and radiative heat transfer, resulting in molten material temperature decrease down to solidification and coolant temperature increase up to vaporization. It may be noted that thermal effects are not only of stabilizing nature but may lead to further fragmentation: as it will be shown in paragraph 2.4.2, depending on the source of energy they can be classified as boiling, internal pressurization and solidification effects. An overview of mechanisms involved in the

global FCI process [16] are presented in figure 2.1 in which μ , σ , κ and H are melt viscosity, surface tension, thermal conductivity and fusion latent heat respectively, while D_j , T_j and U_j indicates jet diameter, temperature and velocity.

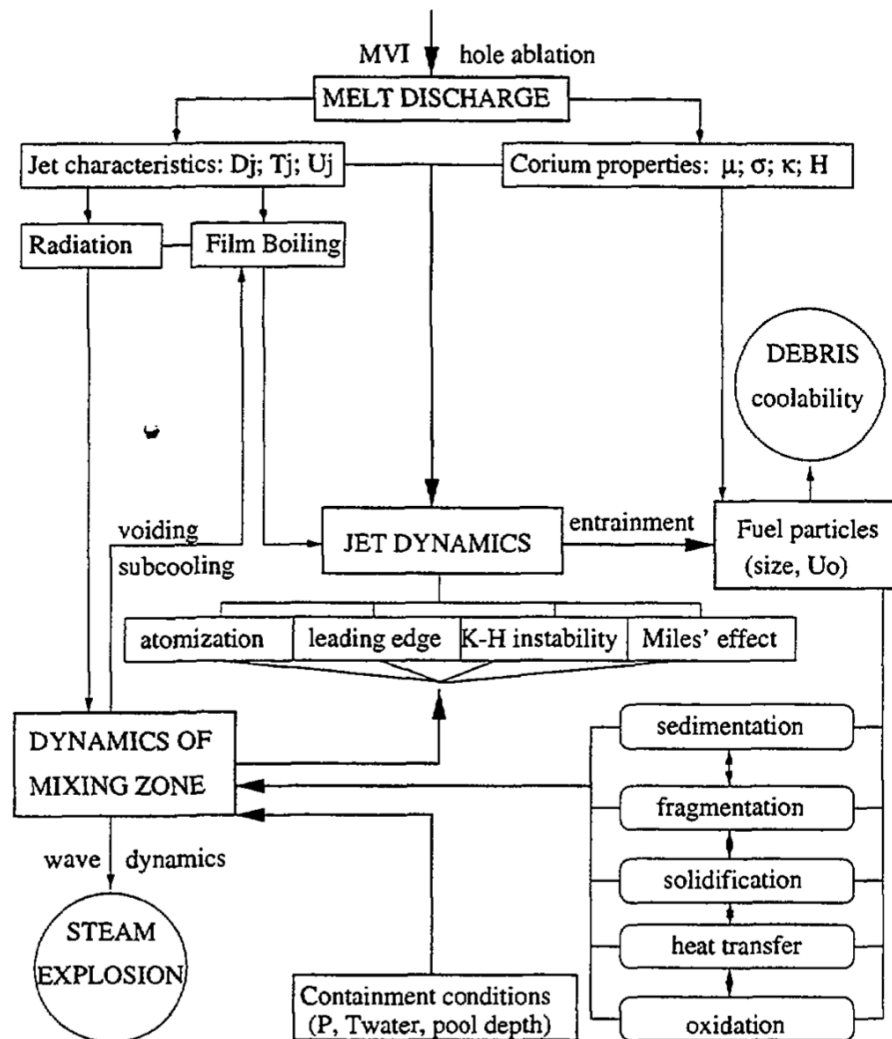


Figure 2.1: Global phenomena occurring during FCI

2.3 Fragmentation regimes

Concerning hydrodynamic fragmentation, it can be clearly pointed out that the driving mechanism for molten corium breakup is strictly related to jet deceleration and difference in velocity between melt and coolant phases. In order to model this complex process, critical and reference parameters must be set for models' development: jet breakup length and weber number can be found as suitable factors governing phenomena evolution. The former, of which and extensive description can be found in section 2.3.1, is able to predict the extent of leading interaction zone, whilst the latter, useful in defining liquid drop breakup, concerns a balance between hydrodynamic deforming forces acting upon the jet or the single droplet and interfacial forces which tend to sustain surface's actual shape. On mathematical terms:

$$We = \frac{\rho v_{rel}^2 d}{\sigma} \quad (1)$$

in which ρ is the melt density, v_{rel} is the relative velocity between molten jet and coolant, σ refers to surface tension and d denotes the characteristic length which may be assumed as the droplets diameter or internal jet diameter based on the model. Weber number is a fundamental parameter in order to assess not only fragmentation regimes but also fragment size by means of Critical Weber Theory (CWT): in case Weber number exceeds a critical value (usually set between 12-18), molten fuel droplet will break into smaller and more stable drops. For liquid drop breakup CWT is used for low Weber number simulations, since experimental results concerning solidified corium mass median diameter were found to be unrelated to high Weber number. Nonetheless, this is not the only parameter involved in particulate size: different melt composition (oxide or metal) resulting in different debris shape, in general cracked brittle fragile the former, round and smooth the latter, as well as prompt boiling

fragmentation and thermal stresses may influence melt breakup and further solidification. As already mentioned, in the framework of Weber number importance an essential role can be found in the definition of breakup regimes. Early studies on jet fragmentation phenomena led to a description of the breakup process in terms of jet breakup length as a function of jet velocity hence the Weber number. A qualitative behavior [17] is reported in figure 2.2

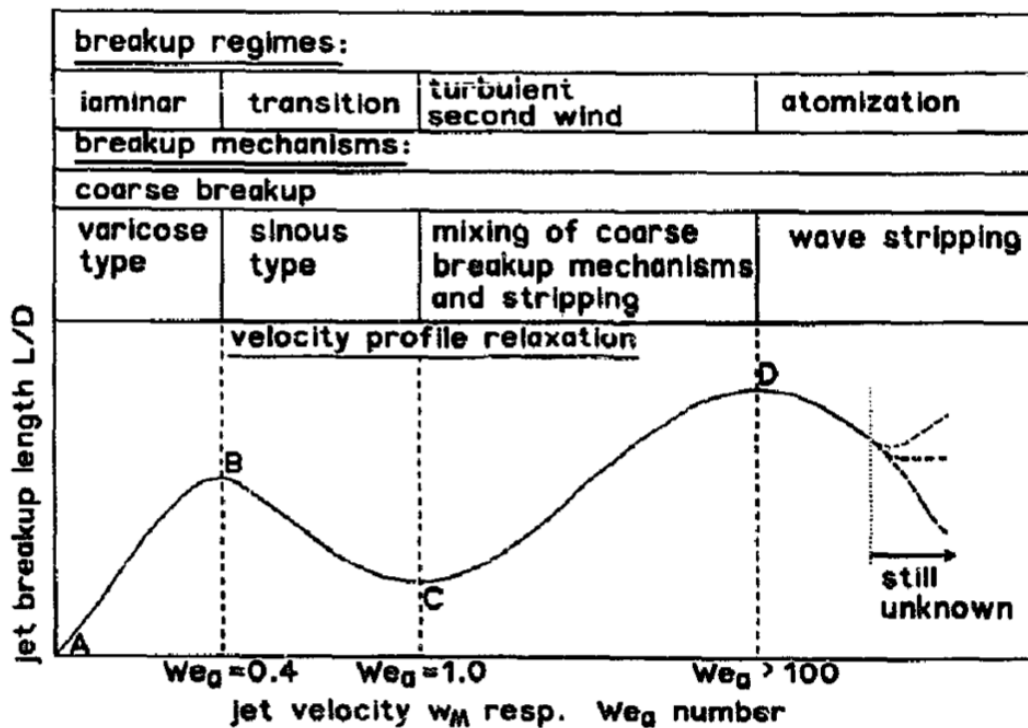


Figure 2.2: Jet breakup mechanism and regimes

Before extensive description of breakup regimes, an overlook of jet breakup behavior in terms of FCI process must be carried out [16], mainly considering four stages. At first, molten material jet injection in lower temperature coolant pool induces a coarse mixing leading to a preliminary fragmentation governed by RTI at leading edge and KHI at jet surface and early vapor phase generation, leading to a lowering of formed

drops cooling rate; as already pointed out in section 2.2, this breakup mechanism is driven by difference in velocity between melt and coolant phase and jet deceleration as it enters the pool. After this initial stage the triggering phase comes into play: onset mechanism for this stage is believed to be vapor film collapse due to some disturbances yet to be completely understood, of which a brief modelling overview will be given in section 2.4.2. The most significant feature of this stage relies on the opportunity for coolant to be in direct contact with molten material, resulting in heat transfer enhancement. In case trigger mechanism is energetic enough, it is possible to enter the third stage known as detonation propagation. This stage is characterized by same breakup mechanism of the first phase, leading to an intensive fragmentation due to propagation of micro-interacting zones between fuel and coolant: this process will lead to an increase of interfacial area hence an increase of heat transfer and shock waves generation. Furthermore, the last expansion phase, following the detonation stage, involves thermal energy conversion in mechanical one, which may act on the surrounding environment as further fragmentation mechanism. This description represents a qualitative behavior for FCI which paved the way to an in-depth analysis of breakup mechanism as reported in figure 2.2.

As already mentioned, fragmentation regimes can be categorized based on coherent jet breakup length as a function of jet velocity hence We number, resulting in 5 main mechanisms. Point A corresponds to 'drop formation zone', developed by low flow rates released from the nozzle in which drops formation slowly takes place at nozzle exit. By increasing jet velocity up to point B, critical flow is achieved: zone A-B is known as laminar or Rayleigh regime, in which drops are formed by means of varicose breakup at the jet leading edge, being surface tension one of the key parameters. This kind of breakup involves small-amplitude, long-wavelength instabilities [16] during FCI. By further increasing jet velocity, it is possible to achieve the first wind induced

regime also known as transition regime, characterized by higher long-wave instabilities inducing a sinuous type of breakup. A rise in velocity will lead to short wavelength development: the second wind induced (turbulent) regime is characterized by coarse mixing and stripping mechanism from jet coherent body side. In case velocity reaches extremely high values, atomization breakup will occur, leading to prompt fragmentation upon jet impact on coolant pool. It should be noted that laminar and transition mechanisms are well understood processes, whilst turbulent and atomization are still under investigation in order to achieve a better physical understanding of the phenomena. Breakup curve analysis may be globally explained by a mixing of breakup mechanisms, mainly coarse fragmentation and stripping under shear flow influence [17], involving additional instabilities related to velocity profile rearrangement caused by turbulence and cavitation, which are able to influence wavelength growth, hence melt-coolant interface instabilities. At last, jet diameter also influences breakup behavior: narrow jets fragmentation is governed by capillarity instabilities due to surface tension resulting in accordance with laminar regime, whilst if larger jets are involved, RTI and KHI are held responsible for breakup, both concerning unstable disturbance wavelength growth.

2.3.1 Jet breakup length

Jet breakup length is able to describe the extension of the primary interaction zone between fuel and coolant [18], referring to the distance between the lower plenum coolant surface and the location in which coherent melt jet no longer exists due to extensive fragmentation.

A first approximate semiempirical correlation was proposed by Taylor [19], considering the dependence of nondimensional jet breakup length from phases density ratio between melt and coolant phases.

$$\frac{L_{brk}}{D_j} = 5.3 \left(\frac{\rho_j}{\rho_c} \right)^{0.5} \quad (2)$$

In which L_{brk} is the actual jet breakup length, D_j refers to jet diameter, subscripts c and j refer to coolant and jet respectively. This correlation was obtained by means of experimental evidence based on investigational studies performed by Sir Taylor himself: he noticed that, even though size and number of droplets formed at high speed jet surface in terms of fragmentation depends on viscosity and surface tension, the total loss rate of material stripped away from a coherent jet does not rely on those parameters i.e., viscosity decrease results in smaller but more numerous droplets, keeping the total rate of material loss constant with respect to the opposite case (increase in viscosity, leading to fewer but larger drops). It should also be noted that this correlation is reliable only for high-speed jets and low viscosity flows, such that fine debris can be produced in order to obtain final drops of lower dimension with respect to the jet diameter.

Saito's investigation of jet breakup governing factors [20], resulted in a nondimensional correlation for jet breakup length which takes into account the balance between buoyancy forces arising from phase density difference and jet inertial forces [7] due to hydrodynamic and thermal interaction:

$$\frac{L_{brk}}{D_j} = 2.1 \left(\frac{\rho_j}{\rho_c} \right)^{0.5} Fr^{0.5} \quad (3)$$

being Fr the Froude number defined as follows:

$$Fr = \frac{v_j^2}{g D_j} \quad (4)$$

At last, Epstein and Fauske [21] proposed a ‘Taylor type’ correlation, introducing the concept of liquid entrainment by melt phase: a tuning parameter E_0 , varying from 0.05 up to 0.1 known as Entrainment Coefficient was included, substituting the constant value independent from velocity used by Sir Taylor.

$$\frac{L_{brk}}{D_j} = \frac{1}{2E_0} \left(\frac{\rho_j}{\rho_c} \right)^{0.5} \quad (5)$$

It should be noted that Saito correlation, unlike Epstein and Fauske correlation [22], shows a dependence from jet initial velocity. Nonetheless, it should be underlined that both equations are effective inside their respective range of validity. Iwasawa and Abe [22] reported experimental results for FCI under several different conditions i.e., water subcooling, pressure, sodium and water coolant, comparing non dimensional jet breakup length as a function of Froude number. Results are shown in figure 2.3, in which filled markers represent sodium coolant, whilst empty markers identify water coolant. As it can be seen, even if breakup length tends to increase as Froude number is increased, most results are compatible with Epstein and Fauske model. Breakup length departure from Epstein and Fauske model was observed in experiments in

which water in saturated condition (or nearly saturated) was employed: for these environments, Saito's equation seems to give a better fitting of the results.

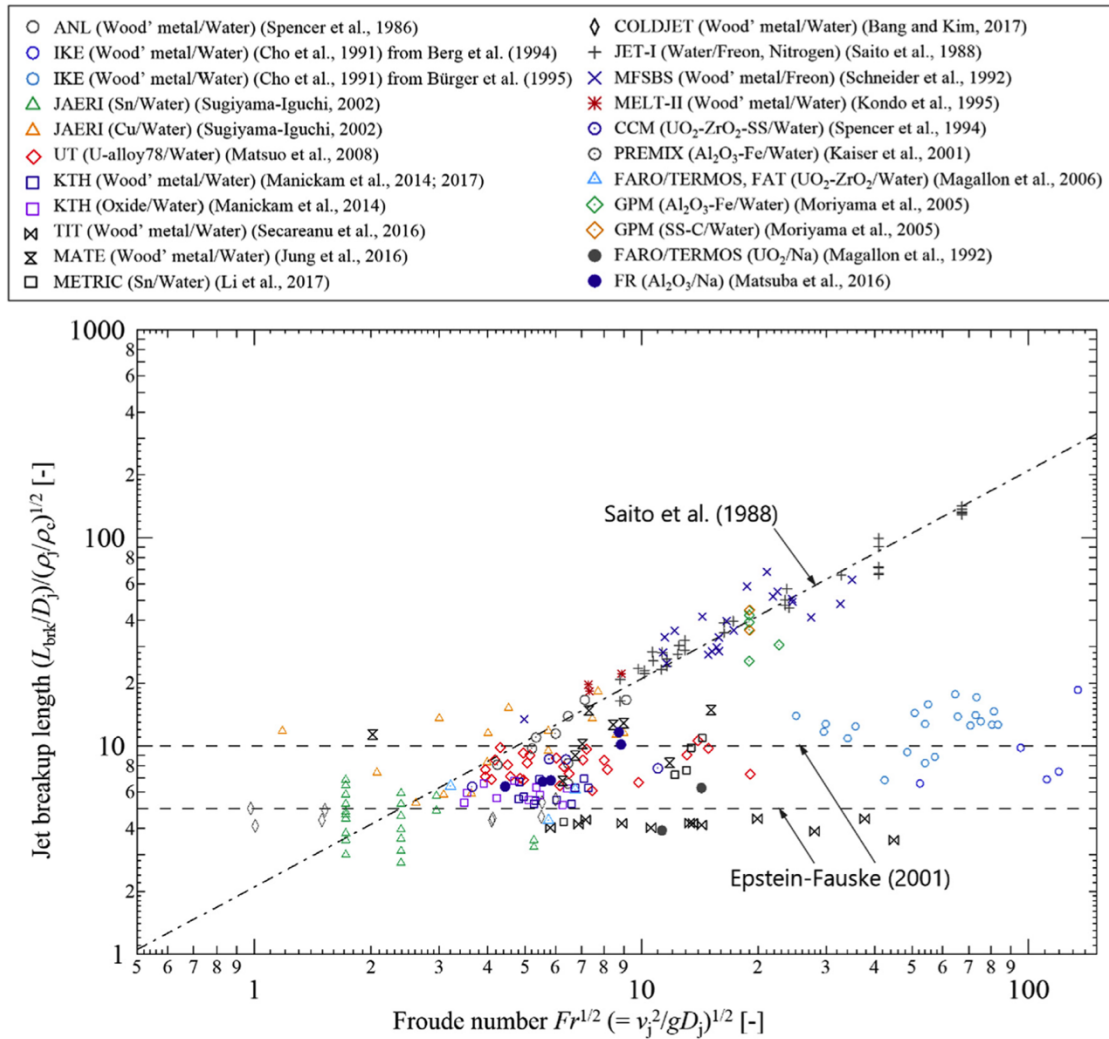


Figure 2.3: experimental jet breakup length compared to Saito and Epstein – Fauske model

At first, based on previous experiments, Moriyama [23] proposed a selection criterion for jet breakup correlations based on Bond number, which takes into account gravitational forces compared to forces due to surface tension.

$$Bo = \frac{\Delta\rho g L}{\sigma} \quad (6)$$

For small Bond numbers (less than 50), Saito's correlation is appropriate, whilst for higher values jet breakup length could be considered closer to Epstein and Fauske model. Unluckily, this criterion didn't show much accordance with Iwasawa and Abe works, which instead showed a good agreement of experimental results with Epstein and Fauske model even at low Bond numbers. Jung [24] performed an experimental campaign in order to focus on jet breakup length analysis: the outcomes suggested that highly subcooled coolant and superheated melt may result in shorter breakup lengths which were well represented by Fauske correlation, whilst for saturated or nearly saturated water, Saito correlation seemed to be a better fit to the results.

As shown by Jung experiments, coolant subcooling is one of the main parameters affecting jet breakup length, which can be displayed as a decreasing fragmentation length as result of coolant subcooling increase. This behavior could be explained by means of vapor film generation at melt leading edge which inhibit direct contact between coolant and melt, resulting in a further penetration of molten material in the pool mainly due to fragmentation suppression. Since vapor film inhibit intensive fragmentation in saturated or nearly saturated cases, a strong vapor generation may occur, resulting in longer jet breakup lengths caused by delayed fragmentation as predicted by Saito's correlation. On the other hand, at high subcooling vapor may condense quite easily such that a stable gaseous film generation may be difficult: this translates into higher jet breakup length due to extensive fragmentation following Epstein and Fauske model. Further development on the description of this mechanism should be carried out, also focusing on other effects affecting breakup length such as melt oxidation and solidification.

2.4 Fragmentation mechanisms and models

Fragmentation mechanism can be categorized based on the effects acting as leading force for molten material breakup. Two main classes can be identified: hydrodynamics effects and thermal effects. The former includes RTI and KHI and boundary layer stripping whilst the latter can be further subdivided in three main categories: boiling effects, internal pressurization effects and solidification effects. A brief overview of all these effects will be shown hereafter, highlighting peculiarities and limitations for the proposed models, following a chronological order as a summary of the state of art reported in [15].

2.4.1 Hydrodynamic effects

Hydrodynamic fragmentation breakup mechanism relies on the analysis of external forces acting on the molten material compared to cohesive forces i.e., surface tension. In order to be an effective process, the former must exceed the latter, resulting in two main causes of fragmentation [15]:

- Acceleration or deceleration of melt jet in liquid phase up to fluids velocity equilibrium, corresponding to a difference in relative velocity induced breakup due to surface forces deforming melt jet droplets up to rupture.
- Fragmentation upon impact, resulting from strong inertial forces which are able to overcome surface tension forces.

As mentioned, Weber number can be found extremely useful for hydrodynamic breakup definition, being able to express fragmentation eventuality by means of ratio among inertial and cohesive forces: this behavior is expressed in the CWT. Among

many hydrodynamic effects, the focus was devoted to RTI, KHI and boundary layer stripping.

2.4.1.1 Rayleigh – Taylor instabilities

Rayleigh – Taylor instabilities evolve at the melt leading edge, involving two different fluids acceleration in direction perpendicular to boundary surface, pointing from lighter liquid to the heavier one [15]. These kinds of irregularities were first investigated by Rayleigh [25] concerning capillarity phenomena in liquid jets. It was assumed that denser discharged fluid under the action of capillarity forces, retains its form as enclosed by a layer of constant surface tension in steady vibrational motion around its original cylindrical shape. On the premises of isochronous vibrations, it is possible to evaluate the wavelength corresponding to two points of a recurring figure which is proportional to jet impingement velocity. When wavelength is comparable with jet diameter, vibration can be assumed as developing in two dimension such that it is possible to estimate the wavelength quite easily by means of harmonic functions, even if for the most general case the use of a Bessel function is required. Instability phenomena at different density fluids interface was later investigated by Taylor [26] obtaining an exponential growth rate of the wavelength describing the instability. At a certain time after the heavier fluid elapses from the orifice, wavelength will continue increasing nonlinearly, such that linear instability analysis is not adequate to describe the problem in analysis, leading to non-linear stability analysis requirement, involving three dimensional effects strongly affected by density ratio expressed in terms of Atwood number A [27]. Being A closer to 1, light fluid penetrates the heavier fluid as a form a round-headed mushroom shape bubble: lighter fluid bubble results unstable, breaking into three-dimensional bubble, leading to spike-like deformation in the

heavier fluid. Furthermore, interactions between bubbles and heavier fluid surrounding them may occur up to heavier fluid spikes break due to various mechanism.

2.4.1.2 Kelvin – Helmholtz instabilities

Kelvin – Helmholtz instabilities, which could be defined as the dominant factor for jet and drops breakup, arise due to difference in velocity at the interface between molten material and coolant. Haraldsson [16] gives a simple treatment of KHI, considering a travelling wave as initial perturbation of the kind:

$$\eta = \eta_0 e^{i(kx - \omega t)} \quad (7)$$

in order to obtain a dispersion relation as function of wave number and frequency. By this evaluation it is possible to obtain perturbation growth rate relating melt velocity v , wavelength λ , wave number k and Weber number as follows:

$$\omega^2 = \left(\frac{2\pi}{\lambda}\right)^2 v^2 \left(1 - \frac{4\pi k}{We}\right) \quad (8)$$

From this dispersion relation, is possible to evaluate the maximum growth rate, corresponding to $k = \frac{We}{4\pi}$: above this threshold value, surface tension tends to suppress KHI. Given this evaluation, is possible to define three main regions for instability evolution; letting We_c be the critical weber number, equal 4π from (8) it can be obtained:

- $We < We_c$: no instability growth is observed, due to an alternate suppression related to surface tension force effects and induction behavior caused by inertial forces on the wave like motion.

This mechanism is known as oscillatory regime.

- $We > We_c$: perturbation growth will increase in time, resulting in interfacial deformation leading to 'finger-like' shape: KHI enters the fingering regime.
- $We \gg We_c$: interface between melt and coolant assumes a roll-up shape up to different interfaces collisions of the coolant: roll up regime.

A schematic idea of KHI regimes is given in figure 2.4, based on Haraldsson calculation.

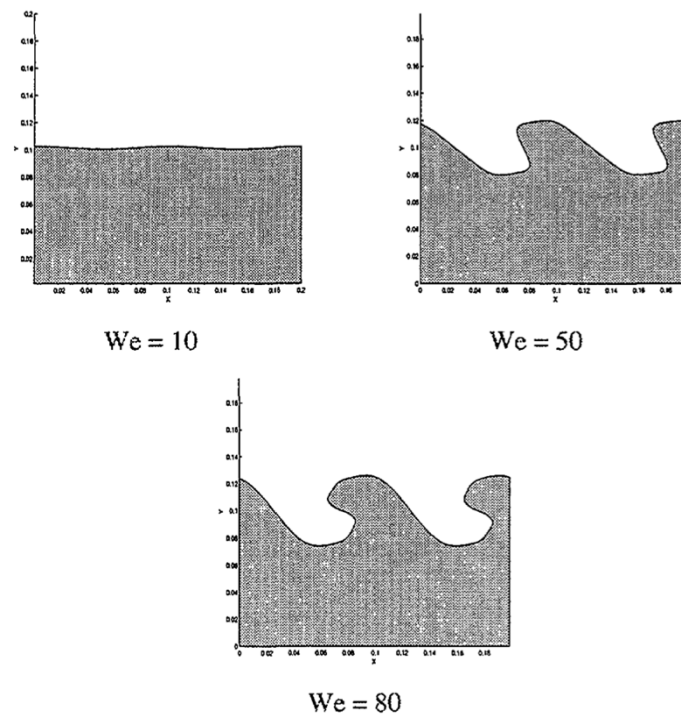


Figure 2.4: KHI evolution regimes

It should be noted that viscous force tends to have the same effect of surface tension on KHI, even if the former acts globally in terms of continuum energy dissipation whilst the latter acts locally at the fluids interface. The effect of viscosity, having as

primary consequence reduction of interface deformation rate, can be expressed by means of Ohnesorge (Oh) number.

A more detailed treatment of KHI is given by Iwasawa and Abe [22], still considering a traveling wave for disturbance description, developing interface growth rate evolution both for spatial and temporal behavior of the instability:

$$\gamma_t = Re \left(\frac{1}{\eta} \frac{d\eta}{dt} \right) \quad (9)$$

$$\gamma_y = Re \left(\frac{1}{\eta} \frac{d\eta}{dy} \right) \quad (10)$$

A complete description of the model is given in [22]. As for the approximated treatment, it is possible to achieve a dispersion relation in terms of angular frequency and wave number and subsequently obtain temporal growth rate of KHI as function of wavelength. Under the hypothesis of direct contact between melt and coolant phase, a trend as shown in figure 2.5 can be obtained. For these calculations a difference in velocity of 1 m/s and a bending stiffness equal to zero was taken into account, resulting in no crust formation between the two phases which are assumed in contact. As it can be seen from figure 2.5, wavelength λ and temporal growth rate γ_t are related: critical value λ_c of wavelength is referred to neutral stable wavelength identifying the switch from stable to unstable interface. If wavelength exceed the neutral stable value, growth rate will increase up to a maximum, in which interface is in the most unstable conditions: for this reason, the wavelength value corresponding to the curve peak is referred to most unstable wavelength λ_m .

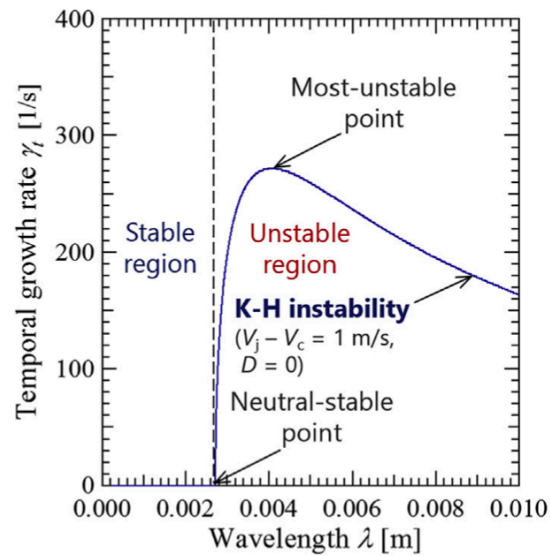


Figure 2.5: KHI stability plot

This model is not only able to evaluate fluctuations in KHI but can also include the solidification effects by tuning the stiffness parameter: as shown in figure 2.6, solidification effects, of which an extensive description will be given in section (2.4.2.3) tends to shift interfacial stability. It should be noted that vapor film considerations are not included and may be the focus for further developments.

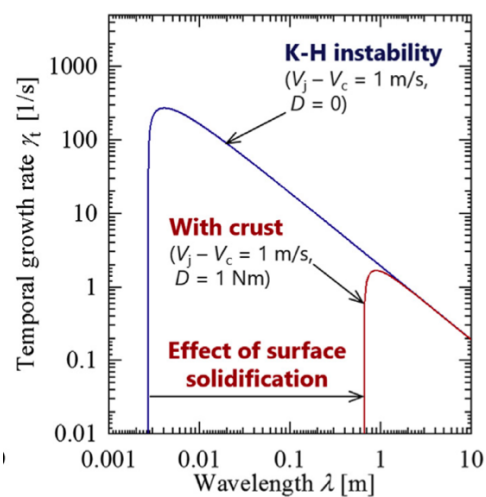


Figure 2.6: KHI stability plot including solidification effects

2.4.1.3 Boundary layer stripping

Boundary layer stripping (BLS) phenomena may arise after KHI full development on the sides of the molten jet. The main cause of this fragmentation behavior can be found in the flow tangential components at the drop surface: shear forces come into play, leading to an extensive fragmentation due to layer detachment. This kind of mechanism is still under investigation, even if some models taking it into account have been proposed, i.e., Sharon and Bankoff [28] suggested that boundary layer stripping could be representative of shock waves propagation. Nevertheless, it was pointed out that BLS alone cannot be held responsible for fragmentation phenomena but should be coupled with other instabilities such as RTI and KHI instead. This logic can be extended to the overall hydrodynamic effects: even becoming dominant for large scale scenarios, they are unable to predict the overall process of extensive fragmentation such that coupling with thermal effects becomes a necessity for global phenomena estimation.

2.4.2 Thermal effects

Thermal effects arising during fuel-coolant interaction are considered to be a cause not only of solidification but also fragmentation. Based on the driving force responsible for breakup, they are subdivided into boiling effects, internal pressurization effects and solidification effects.

2.4.2.1 Boiling effects

Quenching process, which develops as soon as molten material enters the coolant pool, can be explained by means of the boiling curve as shown in figure 2.7.

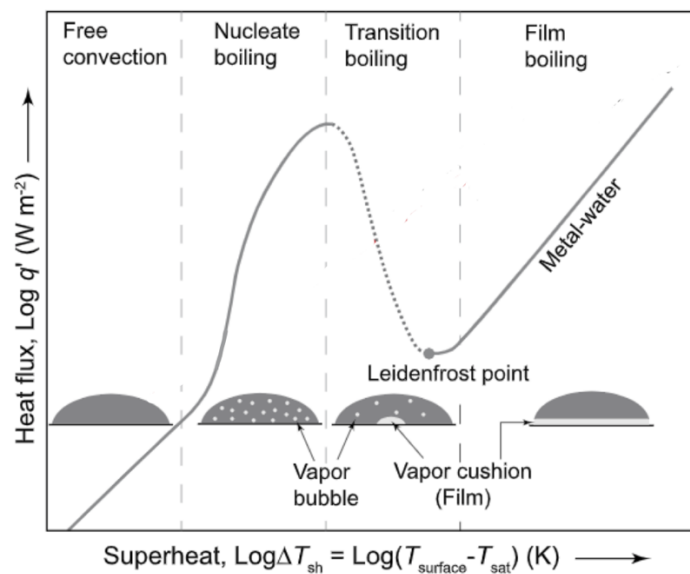


Figure 2.7: boiling curve for melt quenching process

As soon as molten jet surface is free in contact with cold coolant, a vapor film generates at the interface: film boiling regime develops, inhibiting stronger heat transfer mechanism. It is believed film boiling to be 'hydrodynamically quiet' [15] concerning low turbulence phenomena. As quenching process progresses resulting in fuel temperature decrease, switch from film boiling to transition boiling occurs: vapor film collapse occurs at Leidenfrost point and is further reestablished in case molten material temperature exceeds coolant boiling point. This mechanism is affected by strong turbulence due to continuous process of vapor layer collapse and regeneration, leading to a periodic contact of the liquids involved allowing coolant entrainment in molten phase: as addressed later on in this dissertation, instability arising from turbulent

mixing phenomena constitutes one of the driving mechanisms for jet breakup. Transition regimes develops down to nucleate boiling mechanism onset: in this region bubble nucleation occurs near the interface surface at specific nucleation sites, leading to growth and collapse process involving other surrounding bubbles. It is clear that also nucleate boiling can be considered as a turbulent phase, even though the strength of instabilities is much lower than in transition boiling. As molten temperature is lowered heat transfer mechanism does not imply any further phase change, achieving a free natural or forced convection regime. Whilst a detailed treatment of proposed models can be found in Corradini works, for sake of simplicity a cursory comparison and description as a summary of state of art reported in [15] can be found below.

2.4.2.1.1 Proposed models

- Swift and Baker (1965) [29]

Following Swift and Baker approach, molten breakup cause is to be attributed to vapor bubble growth and collapse in turbulent regime, which are distinctive features of transition and nucleate boiling. Unluckily, only breakup mechanism due to boiling effects was proposed without providing a proper mathematical treatment for the overall process including hydrodynamic instabilities effects.

- Witte (1973) [30]

After a thorough analysis of Swift and Baker work, Witte was found to believe that violent boiling hypothesis could not exactly represent the main cause of breakup, due to time scale of involved events. A series of experiments were performed in

order to investigate time evolution of boiling effects. As a result, the overall interaction resulted in a time lapse greater than oscillation period needed for vapor film growth and collapse mechanism to occur: transition boiling could not be considered as main boiling effect for breakup due to low time for instability development. Based on these considerations, Witte proposed a new way of fragmentation due to interfacial tension force lowering caused by pressure upon film collapse.

- Anderson and Armstrong (1974) [31]

This model is based on Swift and Baker assumption, considering a sequence of events describing initial liquids mixing behavior. A stable vapor film formation is assumed, also considering coolant entrapment into melt phase. As a further stage, film collapse is taken into account, leading to heat transfer enhancement and almost instantaneous cold liquid vaporization. Evolution dynamics after film collapse depends on cold liquid fraction vaporized in the previous stage: single liquid – liquid contact results to be enough for single explosion in case of large vaporization, whilst for low vaporization fraction multiple stages of liquid- liquid interaction will produce vapor generation resulting in shockwave propagation. It should be noted that this model relies on the strong assumption of considerable heat transfer between molten material and coolant in a very short time.

- Caldarola and Kasenberg (1974) [32]

Based on a similar mechanism proposed by Anderson and Armstrong, this mathematical model portrays bubble growth dynamics following Rayleigh

equation: growth is possible up to asymmetric collapse due to lack of external inertial forces. During the collapse phase, coolant microjets instabilities may form at the interface between the liquids, impinging on fuel surface leading to fragmentation: upon rupture, elastic wave propagation will occur causing further melt jet breakup. Even though this seems a reasonable mechanism, energy dissipation through the process is not enough to explain intensive fragmentation phenomena.

Bubble growth and collapse mechanism is indeed believed to be one of fragmentation dynamics paths, being able to include spatial distribution analysis of local interactions leading to global interactions due to pressure increase and adjacent bubbles induced collapse. Even though this mechanism is believed to play a role in the fragmentation process, it is not able to account for the overall shattering process, indicating that other breakup means should be taken into account. Most accredited models for fragmentation dynamics including boiling effects are Buchanan's model developed in 1973 as well as Henry and Fauske interpretation. Concerning internal pressurization effects, Kim and Corradini model for single droplet interaction is widely accepted given its unique feature of complete mathematical description. A brief overlook on this model will be given in section 2.4.3.

2.4.2.2 Internal pressurization effects

Both for boiling and hydrodynamic effects, triggering mechanism is induced by external forces acting on fuel surface. As it was shown, this kind of externally driven regimes are not enough to give an extensive comprehension of the fragmentation phenomena. Molten material internal pressure generation should also be taken into

account, resulting in further breakup. Main events triggering an internal pressure generation are represented by coolant entrapment and eventual encapsulation inside the molten phase, cavitation and dissolved gas impurities release. A brief overview of developed models will be given below. Being Kim and Corradini work a broadly recognized model for internal pressurization effect, a specific treatment will be presented in section 2.4.3

2.4.2.2.1 Proposed models

- Long (1957) [33]

Entrapment of coolant in molten phase was incorporated in Long model based on experimental observations on large pours. A possible fragmentation mechanism based on coolant evaporation inside the molten fuel phase was developed and later confirmed by Hess and Brondike in 1969, pointing out three possible explosions outcome, starting from moderated up to violent and eventually catastrophic.

- Witte (1971) [34]

Witte studies confirmed the entrapment theory proposed by Long, developing an alternative triggering mechanism. It was assumed a bonding-like triggering phase, concerning interaction between molten material and bottom plate of the test vessel: once the jet contacts the vessel surface, a sort of bond may arise trapping cold fluid between metal-corium interface. Subsequent vaporization of coolant,

unable to escape from this layer, will induce internal pressures resulting in fragmentation.

- Brauer (1968) [35]

Brauer model was based on experimental observation of molten material bubble growth and rupture during quenching process. These studies predicted a new way of liquid entrapment, known as encapsulation. The proposed model involved a rapid solidification of molten drop, leading to a solid shell generation. Cold liquid could be encapsulated by molten material by means of porosity in the external shell. This would turn into internal pressure generation and eventually fragmentation.

- Shins (1973) [36]

In this model a sequence of events coupling boiling and internal pressurization effects is proposed in order to explain liquid encapsulation and entrainment behavior: as soon as jet enters the pool, a temperature increase is observed in the coolant layer resulting in vapor film and bubble generation. In the transition boiling region, asymmetric collapse of the bubble coupled with resulting cavitation forces will lead to coolant entrainment in the molten material. Once again, an internal pressure will be induced followed by fragmentation. This mechanistic model was proposed without any experimental campaign support: an investigation will be needed in order to evaluate whether this mechanism is sufficiently energetic to reproduce extensive breakup.

- Kazimi (1973) [37]

Kazimi proposed an induced cavitation model for fragmentation, resulting from positive and negative pressure fluctuations at fuel surface caused by vapor film growth and collapse behavior. Pressure changing in very short time may result in pressure waves travelling across the melt drop: as these waves travels towards particle center, a magnification process occurs such that cavitation at drop center may be observed in case high negative values of pressure are achieved. Pressure calculation was carried out using Bernath 1951 equation, resulting in unlikely high value improbable to be observed during FCI. Nonetheless, cavitation could in fact be achieved at lower pressure values comparable to FCI process in case of impurity dispersed in molten phase.

As highlighted by liquid encapsulation theory, cooling and solidification may be a cause of pressure constraint, resulting in internal pressure generation leading to fine fragmentation. Unfortunately, many models lack detailed mechanistic breakup processes, which may be further investigated in the future.

2.4.2.3 Solidification effects

In the dissertation carried out up to this point, a strong hypothesis related to melt state phase was implied, which relies in not considering eventual solidification effects during fragmentation process. It should be pointed out that solidification not only affects final stages of FCI phenomena, but may be also a cause of breakup due to thermal stresses rising in the solidified droplets exceeding yield stress values. Thermal

stresses may be due to a sudden change in the crystalline structure as described by Zyskowski in 1973, or stresses distribution which may lead to rupture.

2.4.2.3.1 Proposed models

- Zyskowski (1973) [38]

This model was based on experimental observations related to solidified debris form, resulting in empty shell or horn-type structure generated by molten material expulsion during the solidification stage. This kind of structure is believed to be caused by internal pressurization leading to thermal stress formation, hence rupture, due to a rapid change in crystalline structure. The mechanism proposed involves six stages, in which the triggering process is attributed to molten jets ejection owing to stresses arising due to shrinkage, leading to direct liquid-liquid contact hence vaporization and eventually explosion. A full analysis of crystallization kinetics was performed by Cronenberg and Fauske in 1974 to check whether discharged fuel will freeze during FCI process, or it may remain in a molten state for a significant time. It was found that solidification occurs as soon as liquid-liquid contact is achieved, underlying that the main mechanism involved in the solidification phase is heat transfer controlled rather than crystallization growth controlled.

- Hsiao (1972) [39]

This model relies on the hypothesis that time required to crystallization ordering should be lower than characteristic time evolution of heat transfer. Based on this,

a solidification rupture criterion was carried out: in case total tangential stress results higher than radial stress, rupture of the solidified drop may occur.

- Knapp and Todreas (1975) [40]

This study investigated the influence of cracks or flaws on thermal stresses development. A failure criterion was assessed, involving local stress intensity factor compared to fracture toughness of the material: in case the former exceeds the latter, fracture will occur. This model has been further developed by Corradini and Todreas in 1979, aiming at minimum particle size evaluation which could survive to thermal stresses rupture. Findings of this studies were in accordance with experimental data on debris size: this model could be considered as a complete first-order approximation for the FCI under thermal stress failure.

It should be noted that, even if thermal stresses breakup mechanisms cannot be neglected, they are unable to predict extensive fragmentation hence a complete model considering film boiling and hydrodynamics effects is required.

2.4.3 Accredited models

- Drop capture model – Henry and Fauske 1976 [41] [42]

A preliminary jet breakup phenomena investigation was delivered by Epstein and Fauske in 1975, just considering film boiling effects in order to estimate jet breakup length by means of two fundamental hypotheses: thin vapor film may be neglected, unlike thick film which must be considered, giving the definition of thin and thick film by a comparison of instability wavelength and film thickness. Other

assumptions made involved steady state FCI, neglecting leading edge effects such as RTI so that the main breakup mechanism to be analyzed is jet atomization. Total neglect of RTI at jet penetration time in the pool will lead to an obvious underestimation of the process. Considering atomization regime, KHI are employed in order to estimate layer stripping and molten mass particle size. Further development of this model aims at including triggering mechanism for a better understanding of the boiling effects on FCI: limit of superheat theory for spontaneous nucleation was adopted. This theory takes into account the possibility of spontaneous nucleation in case no nucleation sites are available: in this case during liquids contact, coolant temperature may rise above standard boiling point. This temperature, known as spontaneous nucleation temperature, is the onset for a prompt vaporization, leading to a consistent rate of nucleation and shockwaves generation which may lead to fuel fragmentation. This mechanism seems incomplete, due to the lack of resemblance with extensive fragmentation experimental results.

Henry and Fauske in 1976 developed the Drop Capture Model, based on their previous studies, in which a modification of spontaneous nucleation mechanism was implemented: mechanism leading to explosive boiling was defined as a stability criterion for cold liquid drop. A complete analysis can be found in [42]. It should be noted that this model is accredited as triggering mechanism due to lack of micro dynamics treatment of the fragmentation phenomena.

- Buchanan's model 1973 [43]

This model, considered to be a good reproduction of the actual phenomena involving a cyclic process for fragmentation behavior, is able to reproduce the overall process. Model strength relies on the prediction capability of surface area increase, hence heat transfer increase, and the use of feedback mechanism for bubble dynamics. FCI is subdivided in five stages of which steps two to five are cyclic:

- Stage 1

This stage provides an initial perturbation caused by a non-specified mechanism, which leads to the first bubble formation at fuel surface proximity.

- Stage 2

An adiabatic expansion of the bubble is assumed, up to its maximum radius: when the threshold value is reached, vapor suddenly breakdown due to subcooled liquid at the boundaries. A cavity is now formed, and its following asymmetric collapse occurs: this leads to an impinging coolant jet generation towards fuel surface.

- Stage 3

As molten jet gradually penetrates into the pool, further disintegration will occur. It was demonstrated that jet length increases exponentially with a time constant proportional to the ratio between velocity and diameter of coolant impinging jet multiplied by of a given constant, which will show a dependence

from fluids density ratio: this leads to an exponential increase of interfacial area related to time constant.

- Stage 4

As FCI proceeds, heat transfer occurs between fuel and coolant jets under the strong hypothesis of constant jet temperature and no film vapor generation at the interface. A sketch of the problem is given in figure 2.8. It should be noted that heat transfer is computed as 1D approximation along element of fuel – coolant - fuel

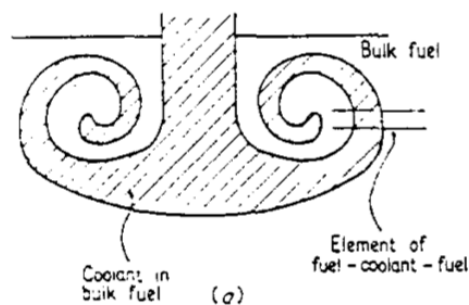


Figure 2.8: Sketch of coolant jet impingement in fuel

- Stage 5

As coolant jet is heated up to saturation temperature, vaporization occurs forming heterogenous nucleation sites. In case sites are not available, coolant temperature must be increased up to homogenous nucleation temperature before evaporation occurs. By instantaneous phase change hypothesis, it is possible to obtain pressure and radius conditions as in input for the subsequent cycle.

This model is able to reproduce many typical features of FCI process, i.e., increase of surface explanation justifying and increase in heat transfer, reproduction of pressure peak at a given distance from the bubble for iterative cycles and self-limiting description based on pressure analysis. On the other hand, many hypotheses were assumed throughout the modelling, leaving some uncertainties upon nonexistence of vapor film in order to justify liquid-liquid contact, instantaneous vaporization and other parameters influence FCI. Furthermore, it should be noted that this mechanism is only applicable in case of boiling regime since it relies upon bubble growth and collapse dynamics.

- [Kim's model \(1985\) \[44\]](#)

Kim's model is a unique study since a complete mathematical description is given instead of only theoretical concepts. Kim study focused on single drop behavior modeling during FCI, subdividing the process in four stages of which the last three are repeated cyclically. Steps involved are sketched in figure 2.9. A brief explanation of phenomena involved in each stage is given below [45].

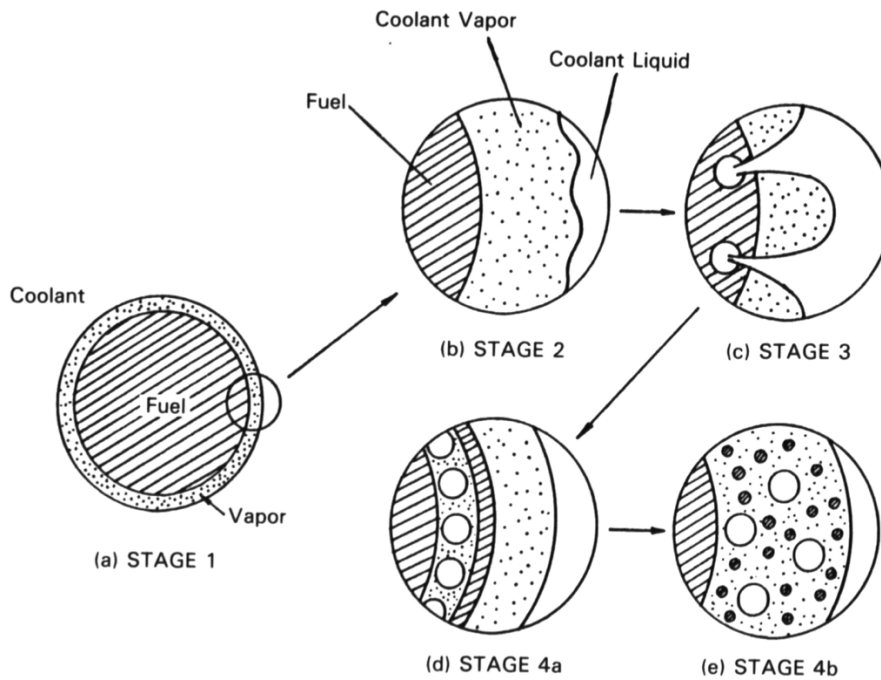


Figure 2.9: single droplet analysis stages

- Stage 1

Film boiling occurs at molten material drop surface submerged in liquid coolant. Aims of this stage is to provide bubble formation and growth by means of transient film boiling model development, considering momentum balance equations for vapor phase and energy balance for melt, vapor and liquid coolant states. Giving appropriate boundary and initial conditions a dynamic model for film boiling was carried out. Triggering mechanism is believed to be induced by vapor interfacial instabilities as entering in the second stage.

- Stage 2

This stage is able to reproduce film collapse due to an external pressure input: as collapsing event proceeds, a magnification of interfacial instabilities amplitude is recorded, modelled as spherical harmonics functions with a first order linear approximation for growth rate evolution.

- Stage 3

This stage is devoted to coolant jet penetration into molten phase analysis, leading to liquid-liquid direct contact condition. As it can be seen, this situation resembles the exact opposite of stage 1, hence a heat transfer mechanism can be easily understood by adapting previous equation to the new case considering different boundary and initial conditions. Furthermore, evolution equations for coolant volume rate of change, drop shape, and penetration velocity and depth are sorted out in order to have a global understanding of the phenomena. Even if it is not clear whether film phase develops immediately or after some time has elapsed from coolant encapsulation, it was found out that vaporization is inhibited up to supercritical temperature achievement: due to lack of nucleation sites, coolant temperature must be raised to homogenous nucleation temperature as already discussed.

- Stage 4

Vapor film growth is taken into account, coalescence of single entrained drops may lead to a layering of molten fuel drops into outer molten shell and internal layer. Due to this schematization, nonlinear growth of molten shell instabilities and motion equations are carried out, resulting essential for molten drop

breakup description: external shell will break in case amplitude of surface instability results larger than shell thickness. This kind of burst breakup results into liquid drops, molten drop and vapor mixture release around the original drop. As this macroscopic bubble vaporizes and expands up to maximum diameter, collapse will occur: fuel will leave the vapor phase, as well as liquid drops, and quench. This process can be repeated from stage 2.

This model showed a good accordance with experimental trends for qualitative bubble growth-collapse behavior as well as debris diameter, particle number and quenching process. Some inconsistencies were found about maximum bubble diameter and ambient pressure increase, perhaps related to instability wave analysis.

2.5 Concluding remarks

Many intertwined factors affecting FCI result into a complex phenomenon description: main global effects related to hydrodynamic instabilities are quite well understood, although proven insufficient for an extensive description of the process, whilst for thermal effects more effort is needed to identify triggering and evolution mechanism for fuel fragmentation. Following a chronological order of events during FCI, even though RTI are essential for the initial step description of molten material impingement on water surface, their role become less crucial as the FCI phenomena evolves. In fact, as molten fuel jet penetrates into the coolant pool, KHI becomes increasingly dominant with respect to RTI up to leading edge contact with bottom plate, in which case the latter cannot longer be a fragmentation driving mechanism, since jet head is no longer existent. This is a strong index of the side role of RTI,

involving just a little breakup transient time, with respect to KHI which are instead an active mechanism for the overall discharge transient time. This consideration is also reflected in the first simple model of Epstein and Fauske, in which RTI were neglected as a first approximation. Concerning thermal effects instead, boiling outcomes can be considered as the main driving mechanism for fragmentation: given the extreme temperature difference between molten jet and coolant pool, bubble generation and growth as vapor film collapse must be accounted for an extensive breakup explanation. On the other hand, also internal pressurization effects, strictly related to the boiling ones, must be taken into account, involving cold liquid entrapment into the molten phase during vapor film collapse. Even though these effects also surely lead to an extensive fragmentation, their relevance can be considered more aleatory with respect to the boiling ones: whilst the latter are always strongly involved, the former depend on the eventuality and frequency of coolant encapsulation inside the molten phase. Nevertheless, cold liquid entrapment will surely occur due to vapor film and bubbles collapse, leading to the necessity of internal pressurization effects complete evaluation in order to account for the extensive fragmentation occurring during the FCI. At last, solidification effects should also be evaluated for the final stages of breakup process in order to have an insightful view of the phenomena, even though their relevance is secondary with respect to the abovementioned effects, since extensive fragmentation of the jet already occurred when their onset time is achieved. Due to the intricate nature of this issue, an exhaustive model including all these effects is not yet developed and scientific community is still unable to predict a well-defined and detailed process for FCI. Anyhow, existing models can be employed based on the scope of investigation, depending on the best fit for the effect that has to be modeled.

3. SAMPSON CODE

3.1 Introduction

In the present chapter an overview of SAMPSON code and its developing framework is reported, together with a brief description of each module and the physical models implemented in order to reproduce severe accident events as accurately as possible. At the end of the chapter, a cursory comparison with other codes will be presented.

3.2 SAMPSON code

Sampson (Severe Accident analysis code with Mechanistic, Parallelized Simulations Oriented towards Nuclear field) was developed by NUPEC Japan (Nuclear Power Engineering Corporation) under Japanese Ministry of Economy, Trade and Industry sponsorship, in the framework of IMPACT (Integrated Modular Plant Analysis and Computing Technology) project. It is a best estimate mechanistic code developed on physical principles implementing theoretical equations, which aims at analyzing a wide range of severe accident phenomena as accurately as possible: loss of coolant, heat-up of fuel rods, their melting and collapse, falling down of molten core considering its relocation into the lower plenum and thermal interaction with retained coolant, debris spreading, cooling, and interaction with concrete, fission product

production, release and distribution in and ex-vessel are some examples. SAMPSON code has a modular and hierarchic structure in which each module can run independently and communicate with others by analysis control module namely ACM. [46]

SAMPSON objective is to evaluate physical and chemical processes as accurately as possible, resulting in a complete overview of a wide range of scenarios in NPP.

In order to achieve this goal, the code is structured in 10 modules, each one concerning a specific NPP part or behavior as shown in fig 3.1.

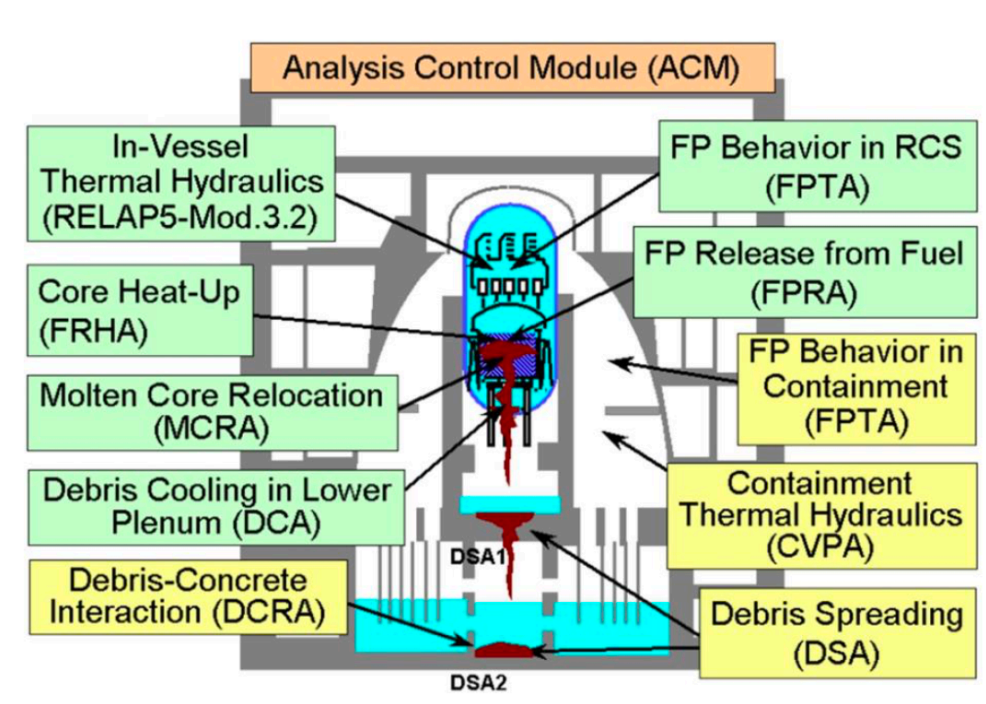


Figure 3.1: Overview of SAMPSON modules

3.3 SAMPSON modules

- ACM: Analysis Control Module
- THA: Thermal Hydraulics in RCS (reactor cooling system) Analysis module
- FRHA: Fuel Rod Heat up Analysis module
- FPRA: Fission Products Release from fuel Analysis
- FPTA: Fission Products Transport Analysis
- MACRES-FPTA: Fission Products Transport behavior analysis module
- MCRA: Molten Core Relocation Analysis module
- DCA: Debris Coolability in lower plenum Analysis module
- DSA: Debris Spreading Analysis module
- DCRA: Debris-Concrete Reaction Analysis module
- CVPA: Thermal Hydraulics in PVC (primary containment vessel) Analysis module

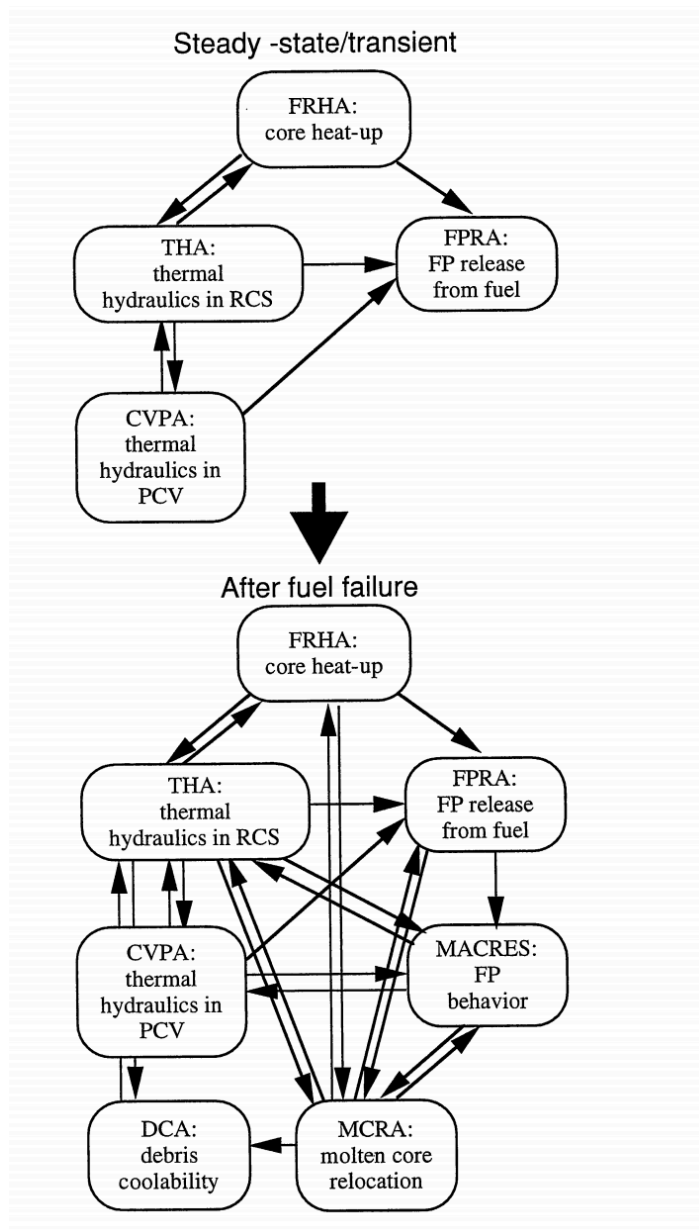


Figure 3.2: SAMPSON modules linking and data transfer

These modules are controlled by ACM, linking them together as shown in figure 3.2 considering each arrow as data transfer.

A brief description of each module will be presented, in order to overview SAMPSON structure and computing capability.

3.3.1 FPTA

FPTA is the fission product transfer behavior analysis, which is strictly connected to FPRA (fission product release analysis), as shown in fig. 3.3

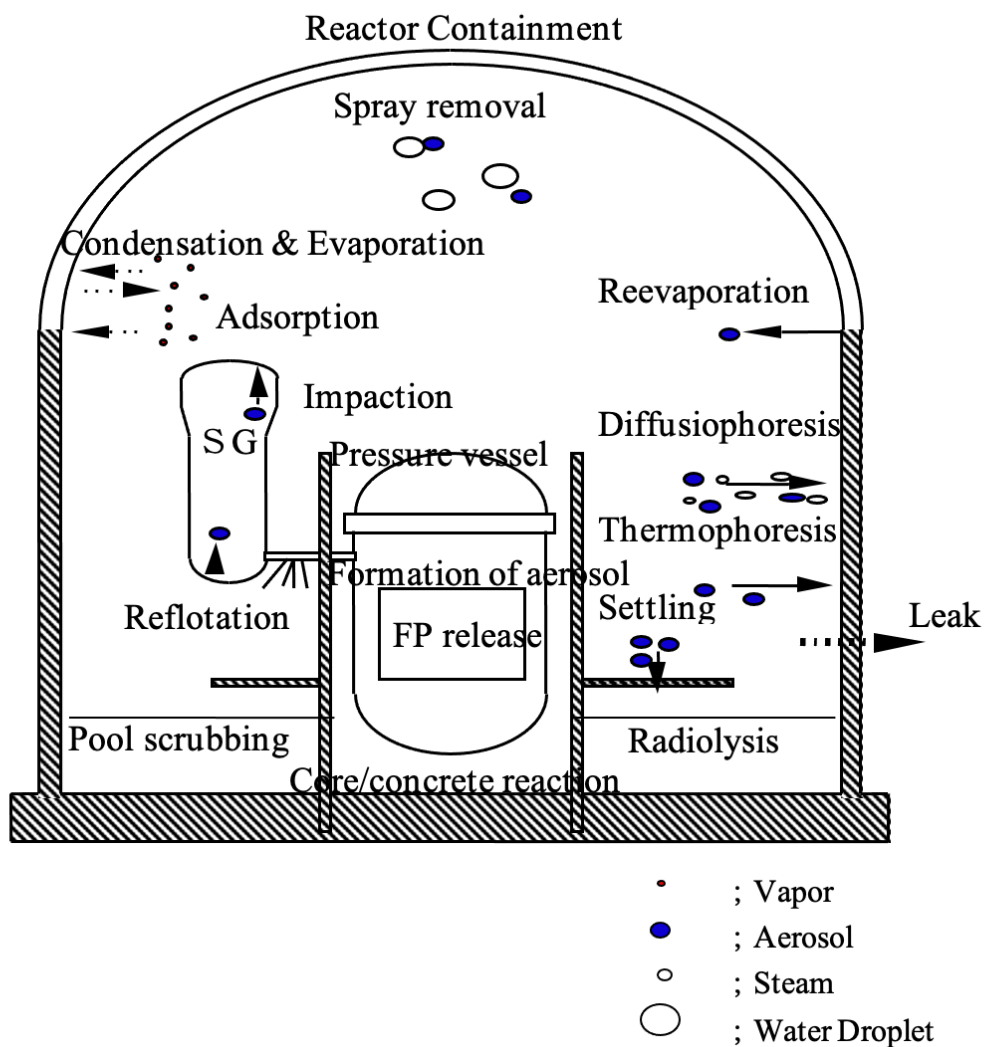


Figure 3.3: Outline of fission product behavior

FPRA computes the fission products FP released by the fuel, whilst FPTA analyses its distribution in the reactor containment, primary system and the quantity discharged in the environment. [47] As in fig. 2.3, FP are formed in the fuel as a by-product of the nuclear fission chain reaction and accumulate in the fuel/cladding gap. After the cladding failing, FP are released in the primary system taking a chemically and physically stable form, according to the external atmosphere. Furthermore, as fuel temperature increases, a fuel melting could occur such that FP are discharged directly from the debris bed and, moreover, from the molten pool decay heat.

In general FP behave as gas and aerosol which can be trapped in coolant and structural material; as they accumulate, a wide range of deposition mechanism can occur such as gravity settling, thermophoresis, diffusion, diffusionphoresis and inertia collisions, but a fraction of accumulated FP could evaporate and be discharged in the containment: in this accidental scenario case, they are removed by scrubbing or spray. FPTA, dividing facilities in nodes, solves differential equations (mass and energy balance, including chemical reactions of main FP) [48] related to transport and deposition mechanisms listed above for each node.

3.3.2 FPRA

As mentioned in the previous paragraph, FPRA is the module analyzing FP release from crust and molten pool, release after fuel failure, and transport within the fuel pellet [49], basing the latter calculation on the model developed by B. J. Lewis, according to which FP reaching the boundary pellet inner surface are completely released. An improvement of the model was later proposed and implemented, considering semi-volatile FP release.

3.3.3 FRHA

Fuel Rod Heat up Analysis module analyzes phenomena until failure of fuel rods in severe accidents [47]: by using different models it takes into account a wide range of events such as fuel pellets heat up, failure of cladding and its eventual brittle fracture and various kind of reactions, for instance zirconium-water reaction and zirconium-uranium dioxide eutectic reaction. [50] FRHA models are based on two-dimensional geometry (r-z coordinates), such that a 2D basic equation for heat transfer is used, considering fixed temperature, heat flux, heat transfer and radiative heat transfer as boundary conditions. Treating heat transfer between fuel pellets and inner cladding surface as a gap conductance [51] based on a simplification of the FRAP-T6 model [52], two cases can be distinguished whether fuel pellets are in contact with cladding or not: the former is proportional to contact pressure, whilst the latter considering gap conductance due to gaseous FP, is inversely proportional to the gap length. Cladding plastic strain is obtained by Prandtl-Reuss equation solving the elastic problem based on strain-increment theory for stress analysis, considering Von Mises condition for yield stress. Cladding rupture occurs when actual stress in tangential direction reaches burst stress, whilst brittle fracture conditions by heat impact depend on two key parameters such as oxygen concentration in zirconium dioxide beta phase and its temperature.

At last, exothermic zirconium and water reaction $\text{Zr} + 2\text{H}_2\text{O} \rightarrow \text{ZrO}_2 + 2\text{H}_2$ is taken into account: Zr-H₂O reaction rate is expressed by mass increment based on parabolic law [53] above 1373 K.

3.3.4 MCRA

MCRA (Molten Core Relocation Analysis) adopts a multi-phase, multi-component and multi-velocity field approach simulating the relocation behavior of molten core into the lower plenum in case of severe accident, being a dominant factor in in-vessel retention [54]. As shown in figure 3.4, physical mechanistic models included in MCRA can be summarized in:

- Flow regime and interfacial area model
- Momentum exchange model
- Heat transfer coefficient model
- Metal-water reaction model
- Phase change model
- Volumetric heat source model

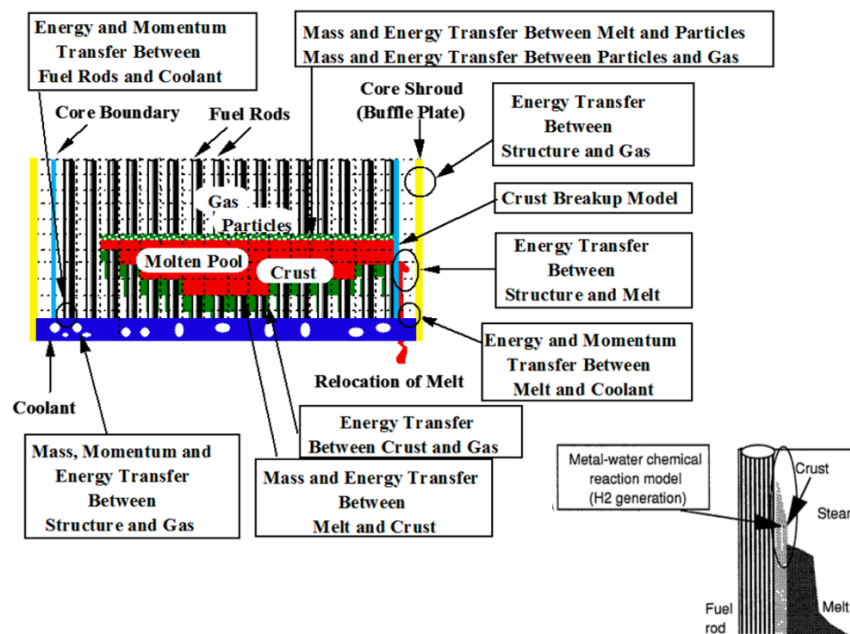


Figure 3.4: Basic MCRA physical models

The models mentioned above are able to conceive main key parameters in case of severe accidents scenario such as: loss of coolant, melting and collapse of fuel rods after heating up, extension of molten pool, falling down of molten core, its relocation into the lower plenum and thermal interaction with retained coolant, injection of coolant by emergency core cooling system and debris cooling in case of in vessel retention. [47]

MCRA consists of two types of HIS (heat interactive structures) namely 'annulus' HIS (surrounding the rod elements) and 'slab' HIS (on any of the six surfaces defining the computational cell). [55] MCRA is globally able to treat nine liquid components and four structure components, solving fifteen mass conservation and ten energy conservation equations for liquid and mixed gas phase components and three momentum conservation equations. [56]

3.3.5 THA

THA module, which concerns thermal hydraulic analysis of reactor cooling system (RCS), is subdivided in two sub-modules namely THA1 and THA2. The former analyses thermal hydraulic parameters during the period starting from normal operation up to fuel cladding failure when reactor core is uncovered by water, whilst the latter takes over after fuel failure analyzing RCS thermal hydraulic except from core region, being MCRA task after 1200K (average fuel burst temperature) [56]. Hereinafter, THA1 and THA2 will be referred collectively as THA unless otherwise specified.

THA, based on RELAP5/MOD3 code, applies a heterogeneous non-equilibrium two fluid model computing RPV and primary system thermal hydraulics parameters by means of node-junctions method, such that THA physical models and numerical

solution are equivalent to the one described in RELAP5/MOD3 code manual. [57] An example of nodalization is shown in figure 3.5, considering the current Fukushima NPP study case.

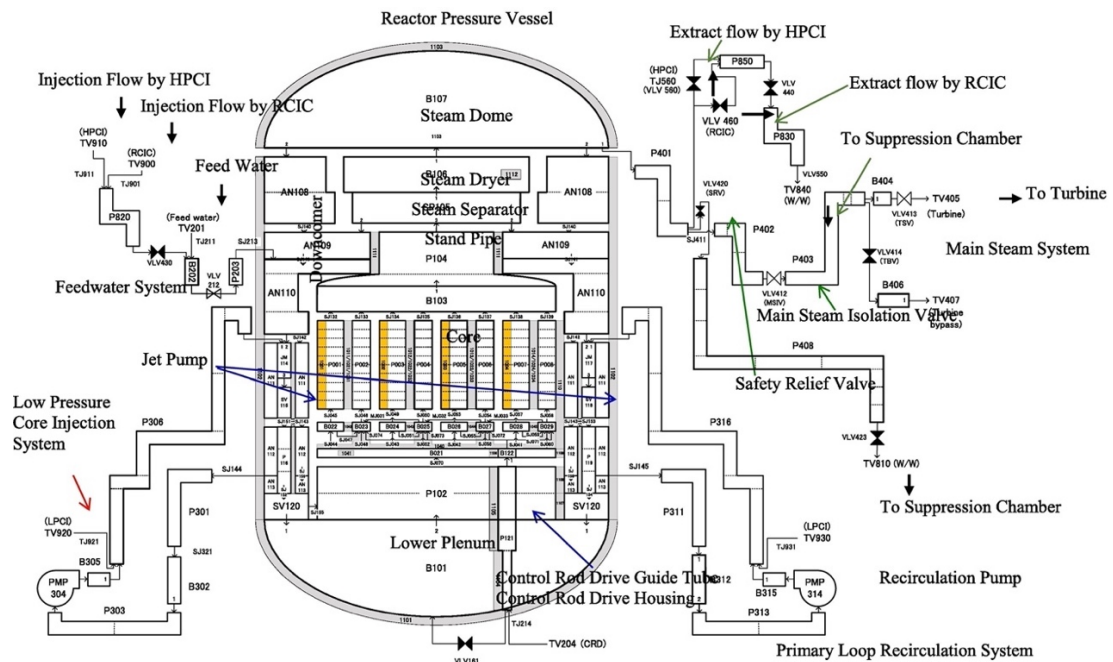


Figure 3.5: Fukushima THA nodalization based on RELAP5/MOD3 code

As shown in figure 3.6, THA simulates reactor thermal-hydraulic evolution during both normal operation and accident scenario, interacting directly with all other SAMPSON modules.

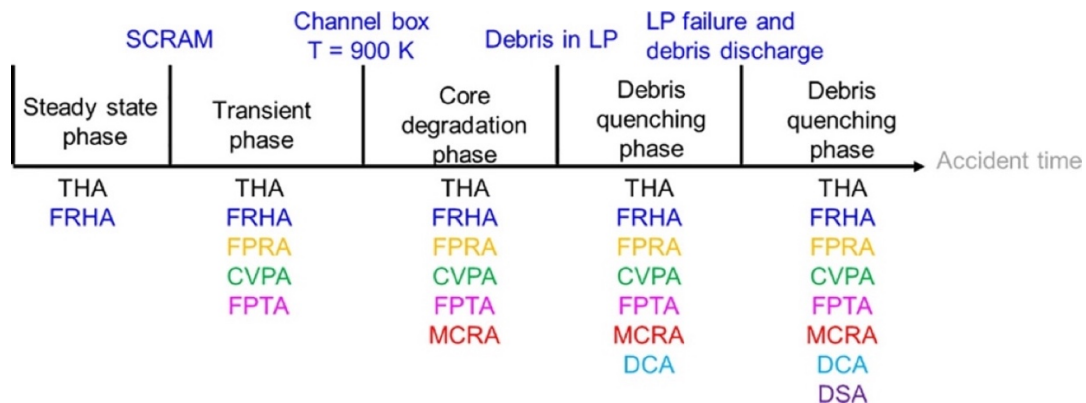


Figure 3.6: Onset of SAMPSON modules in function of accident evolution time

This feature of THA is essential for the present dissertation, in which coupling between THA and DCA is necessary in order to evaluate debris fragmentation and heat exchange.

3.3.6 DCA

Debris Coolability Analysis module takes into account phenomena related to debris relocation into the lower head such as cooling and spreading of continuous phase debris, cooling of accumulated melted particle (debris bed) and consequent heat damage to the pressure vessel and penetration pipes, water gap cooling between debris and vessel and its external cooling.

DCA is composed by a spreading model, a detailed coolability model and a simplified one, having as final thermal hydraulic objective 3D natural convection resolution for debris pool cooling, including solidification. [58]

DCA module overview is given in figure 3.7, whilst for a detailed treatment of this module can be found in chapter 5.2.1

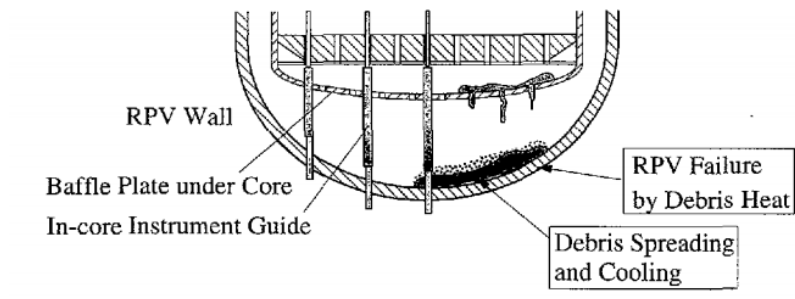


Figure 3.7: Debris falling and spreading phenomena in the lower head

3.3.7 DSA – DCRA

DSA module investigates ex vessel phenomena, focusing on continuum phase debris spreading on containment concrete floor after RPV failure, cooling of debris bed (molten core particles accumulating in time) and heat damage of the concrete base.

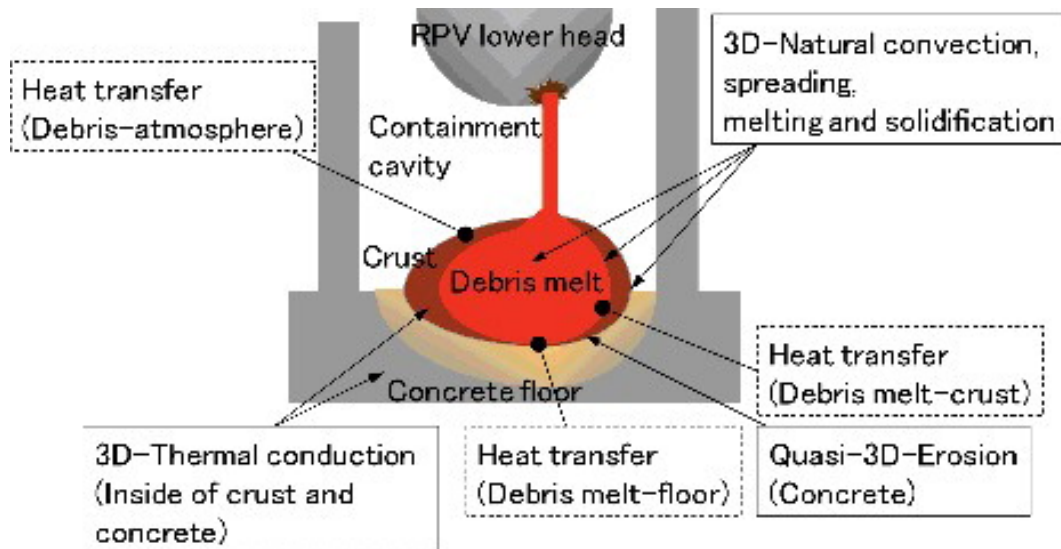


Figure 3.8: Phenomena modeling in DSA module

DSA was originally developed for short term molten core concrete interaction (MCCI) up to debris spreading stop [59], triggering DCRA module (Debris-Concrete Reaction Analysis) for long term MCCI calculation; however, an improvement of DSA module in terms of concrete erosion was implemented [60] starting from a quasi-3d model advancing to a fully 3D model, following needs of sufficient spatial resolution for a first estimate of containment vessel failure and debris removal planning.

DSA, acting as a rough CFD model with moving boundaries, solves Navier Stokes equations for a Newtonian fluid using SMAC (Simplified Marker And Cell) method [14] and incomplete Cholesky conjugate gradient matrix method for pressure analysis [61], employing four types of cells namely: debris, crust, free surface or structure as shown in figure 3.9.

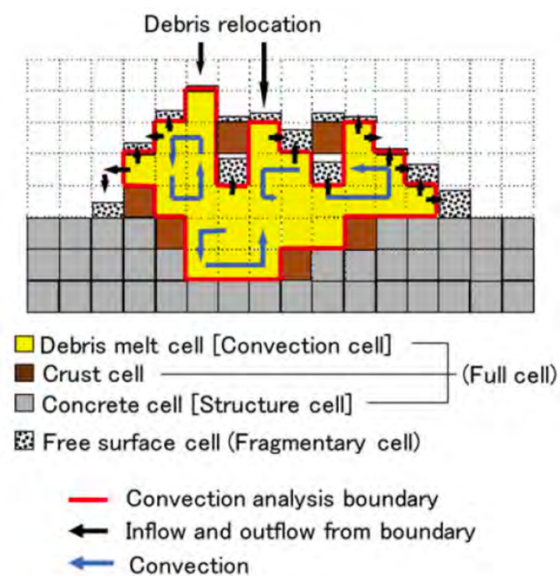


Figure 3.9: DSA computational cells and moving boundaries for debris spreading

Solving such complex phenomena, DSA works under two main strong but necessary assumptions:

- Fallen debris is treated as a continuum body, restricted to the containment floor by gravity such that gas entrainment and debris backscatter is not possible
- Crust transport can be applied only in vertical direction

3.3.8 CVPA

Containment Vessel Phenomena module involves pressure and temperature analysis regarding ex vessel events during light water reactor severe accident including a wide range of physical models for thermal hydraulics, structures and material properties, safety systems, combustion and containment failure.

Module structure and nodalization constitutes of several cells as control volumes in which containment vessel is divided (wall, floor and ceiling), connected by flow paths. An example of CVPA cells and models for thermal hydraulic analysis is given in figure 3.10. Thermal hydraulics model solves mass and momentum conservation equations in and between cells for path flow rates and mass calculation, energy conservation and state equation for ideal for temperature and pressure analysis, being steam treated as an ideal gas. Moreover, using leakage, combustion, containment safety features and failure models it is possible to obtain a containment vessel status overview.

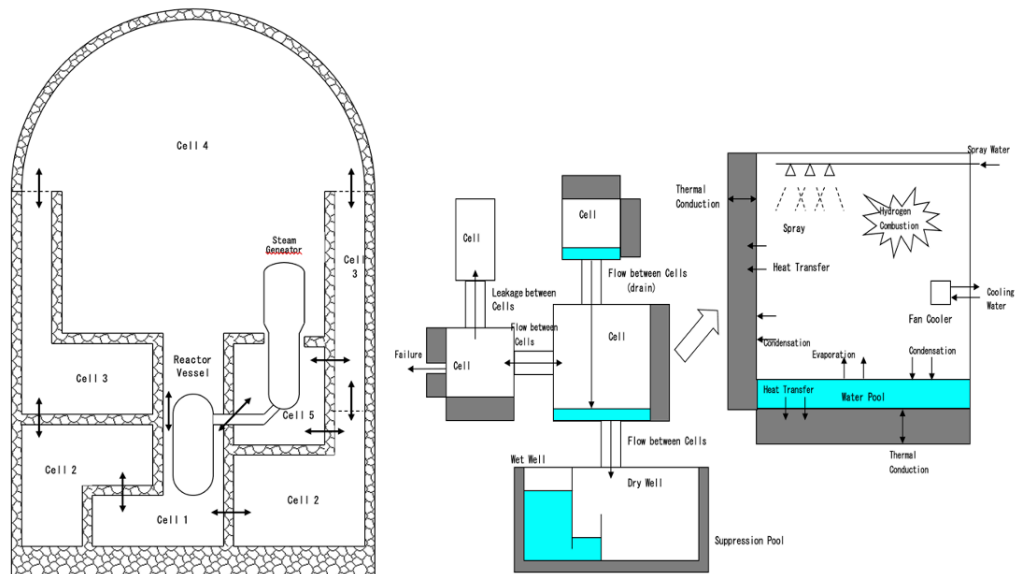


Figure 3.10: examples of PWR containment cells and thermal hydraulics models

3.4 Concluding remarks

The third chapter of the present work summarizes SAMPSON code from an operational point of view, presenting its peculiar features.

Being a mechanistic code, SAMPSON is able to overcome very important issues compared to lumped severe accidents codes such as MELCOR and MAAPE: for instance, 3D Navier Stokes resolution, detailed modeling for each and every phenomenon regarding severe accident, and a few tuning parameters and correlations which translates into simulations coherency for every user.

4. FARO L-14 EXPERIMENT

4.1 Introduction

Regarding numerical code validation in melt jet fragmentation framework, many experiments were performed by several institutions for phenomena assessment. In the first part of this chapter, an overlook of these studies will be presented, underlining differences and boundary conditions influence, followed by an in-depth presentation of FARO L-14 experiment used for IAE molten jet fragmentation numerical verification and first attempt validation in SAMPSON code.

4.2 Jet fragmentation experiments

Fuel-coolant interaction is a critical event regarding severe accident scenario in terms of event progression and risk assessment. FCI, involving contact between molten core material and coolant, was widely investigated by many institutions all over the world i.e., KIT, JRC Ispra, and CEA in Cadarache regarding different scopes of analyses i.e., single melt droplet, large scale involving several kilograms of debris, jet breakup, quenching behavior and solidification effects.

Key tuning parameters for FCI investigation concern the different combinations of coolant and molten materials in analysis and their quantity as well as relative ratios,

pressure and temperature. In the framework of fuel-coolant combination, four main systems can be identified: oxide/sodium, metal/sodium, oxide/water and metal/water [22]. Regarding sodium coolant interaction with molten material, different standard metal [62] and oxide [63] melt composition were deeply investigated in the BETULLA facility at JRC, whilst M-series experiments performed by Argonne National Laboratories involved just oxide fuel [64]. In the same framework, Sandia National Laboratories (SNL) conducted FLAG experiments focusing on steam explosions event occurring during FCI [65], as well as the tests performed at JRC Ispra FARO test facility in which 100 kg of uranium oxide was poured into sodium [66]. Reports of experiments regarding sodium coolant – melt interaction can be found in Table 4.1 concerning oxide mixture and Table 4.2 for metal composition: typical oxide mixture consists of UO_2/Al_2O_3 , while reference metals are stainless steel, copper, silver, iron and aluminum.

Table 4.1: Experimental works for oxide/sodium interaction

Institution	Facility and experiment	Melt composition
JRC	BETULLA	UO_2, Al_2O_3
ANL	M - series	UO_2-Mo, UO_2-ZrO_2-SS
JRC	FARO/THERMOS	UO_2
SNL	FLAG	Fe- Fe- Al_2O_3 , UO_2-ZrO_2-SS

Table 4.2: Experimental works for metal/sodium interaction

Institution	Facility and experiment	Melt composition
JRC	BETULLA	SS-Cu
ANL	CAMEL	U, U-Zr, U-Fe
JAEA	MELT	Al
CRIEPI	-	Ag, Cu

Focusing on water as coolant, interaction with metal has been investigated by many institutions targeting singular processes during FCI i.e., Berkeley Technology Center (BNL) studied various possible melt discharge geometries whether single or multiple nozzles involvement, Japan Atomic Energy Research Institute (JAERI), Argonne National Laboratory (ANL), Japan Atomic Energy Agency (JAEA) and Kungliga Tekniska Hogskolan (KTH) focused on solidification effects such as fragments size and shape, whilst Power Reactor and Nuclear Fuel Development Corporation (PNC) examined steam generation around melt droplets and jet. Main experimental works are listed in table 4.3

Table 4.3: Experimental works for metal/water interaction

Institution	Facility and experiment	Melt composition
ANL	COREXIT	Wood's metal, Al, Al-U
PNC	MELT-II	Wood's metal
POSTECH	MATE	Wood's metal
SJTU	METRIC	Sn

At last, regarding oxide corium discharge in water several phenomena related to FCI were highlighted by experimental works, i.e., SNL by means of FITS series [67], ANL with MIXA studies [68], United Kingdom Atomic Energy Authority by MIXA experiments (UKAEA) [69], JAERI in the framework of ALPHA program [70], as well as ECO experiment [71] at Forschungszentrum Karlsruhe (FZK) investigated corium discharge by means of thermite mixture reaction. ANL also used oxide mixture to investigate hydrogen production upon Zr injection. On the other hand, experimental facilities such as KROTOS in JRC, FARO/TERMOS and FARO/FAT at Ispra concerned uranium dioxide injection in water as scope of investigation, the former focusing on steam explosions investigation (as well as the TROI facility at CEA in the framework of the OECD/SERENA project), whilst the latter on pressure response, particulate size distribution and bottom cake sampling, providing data sets for many numerical studies and computer codes verification and validation. Most relevant studies are presented in table 4.4

Table 4.4: Experimental works for oxide/water interaction

Institution	Facility and experiment	Melt composition
SNL	FITS	Al ₂ O ₃ - Fe
UKAEA	MIXA	UO ₂ - Mo
JRC	KROTOS	Al ₂ O ₃ , UO ₂ - ZrO ₂
JRC	FARO/TERMOS, FAT	UO ₂ - ZrO ₂
KAERI	TROI	UO ₂ -ZrO ₂ , Al ₂ O ₃ , ZrO ₂
FZK	PREMIX	Al ₂ O ₃ - Fe
KTH	MIRA	CaO-B ₂ O ₃ , MnO ₂ -TiO ₂ , WO ₃ -CaO

For the purpose of this dissertation, FARO L-14 from L series was selected among many tests performed in this facility for FCI. A comparison between L-series experiments and a complete description of L-14 setup and results can be found in section 4.3

4.3 FARO tests

Furnace And Release Oven (FARO) facility has been developed by JRC Ispra in the framework of severe accident progression studies related to molten core material injection into the lower head, after core failure stage. Its aim is to provide an in-depth knowledge and dataset for assessment of many phenomena occurring during FCI such

as jet breakup, quenching, pressure behavior and eventually steam explosions. FARO test facility was established in 1987, operating at first for liquid metal fast breeder reactors concerning molten fuel – sodium interaction. It was only three years later, that the main focus addressed LWR safety issues concerning FCI, involving prototypical molten mass mixture i.e., UO_2/ZrO_2 , $\text{UO}_2/\text{ZrO}_2/\text{Zr}$ and several accident scenario boundary conditions such as different initial pressure, water subcooling and pool depth, etc., for a total of 12 FCI tests. An external view of FARO facility is reported in figure 4.1

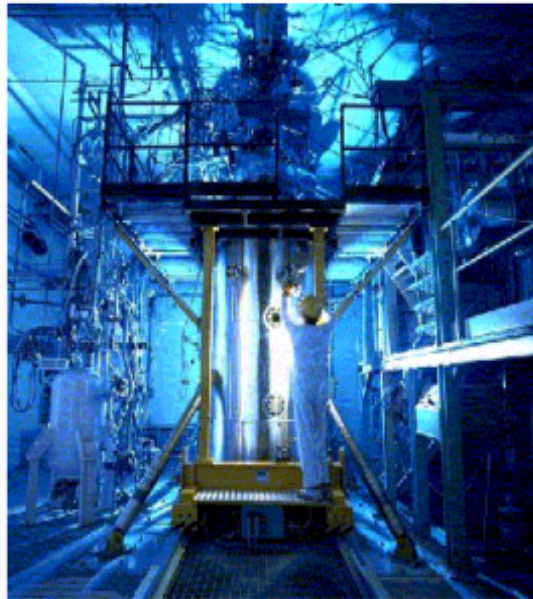


Figure 4.1: FARO test facility external view

4.3.1 FARO test facility

The initial configuration of FARO test facility, reported in figure 4.2 involved 5 main elements: a furnace, an intersection valve, the release vessel, interaction test section and venting system. The melting furnace is connected to the test vessel by a release channel and isolated from it during interaction by the main isolation valve SO₂. If pressure reaches the threshold value (set to 9.3 MPa) during corium quenching, venting to the condenser occurs. The corium melted in the furnace is at first released to an intermediate vessel and then into water by gravity; at the bottom of the test vessel, a debris catcher completely submerged in water collects the corium after the interaction. Starting from FARO L-14 up to L-24, TERMOS interaction vessel was used, whilst from L-27 it was changed into FAT interaction vessel reported in figure 4.3. TERMOS test section, cylindrical shape with 0.71 m diameter and 1.5 m³ volume, is a pressure vessel designed for 10 MPa pressure and 573 K temperature with the addition of a debris catcher at the bottom plate. FAT test vessel instead, keeps same TERMOS temperature feature design but lower pressure (8 MPa) and larger dimensions (1.5 m diameter and 2 m height). FARO tests' main goal was to investigate the influence of melt quantity, composition, water depth and initial pressure on quenching and melt/water mixing behavior: many experiments were carried out tuning these parameters in order to have a complete understanding of FCI phenomena. Some examples of tests are reported in table 4.5 highlighting differences on modulated parameters involved and how they impact on the final results in terms of debris grain size, bottom cake and particulate debris quantity generated.

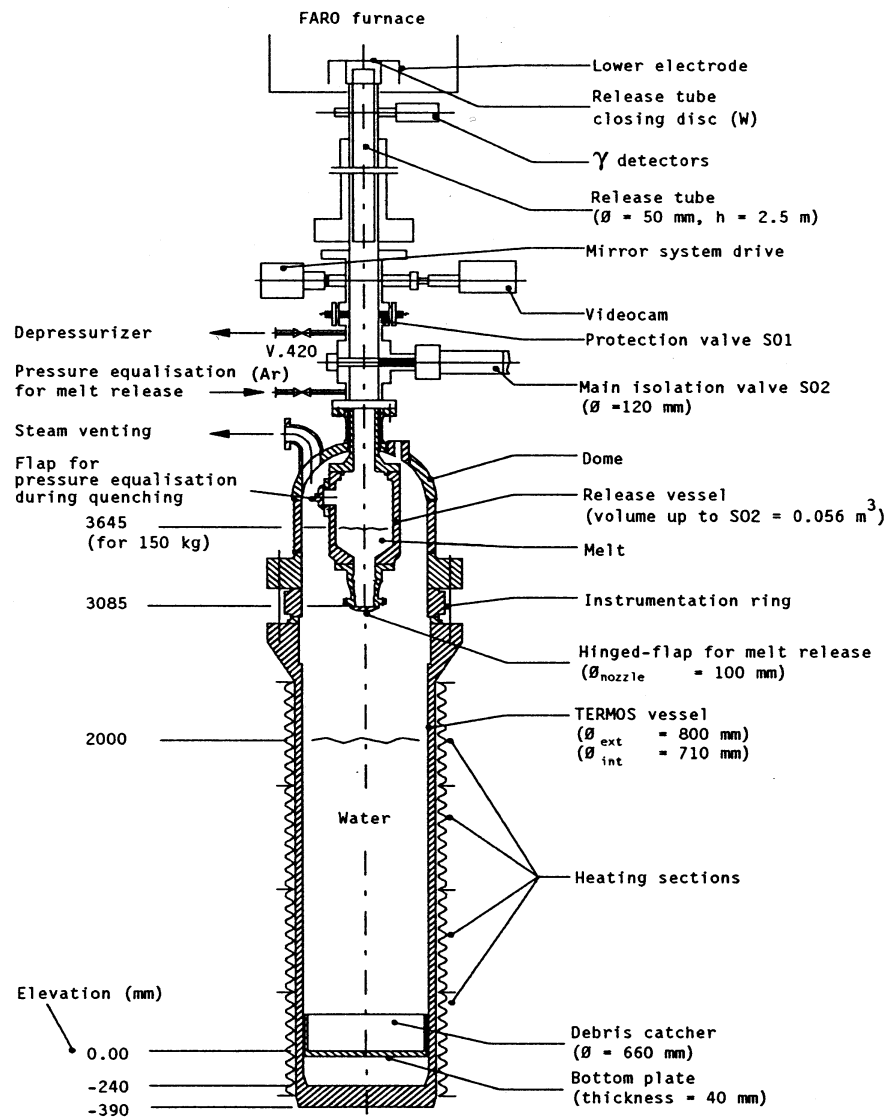


Figure 4.2: FARO facility with TERMOS vessel

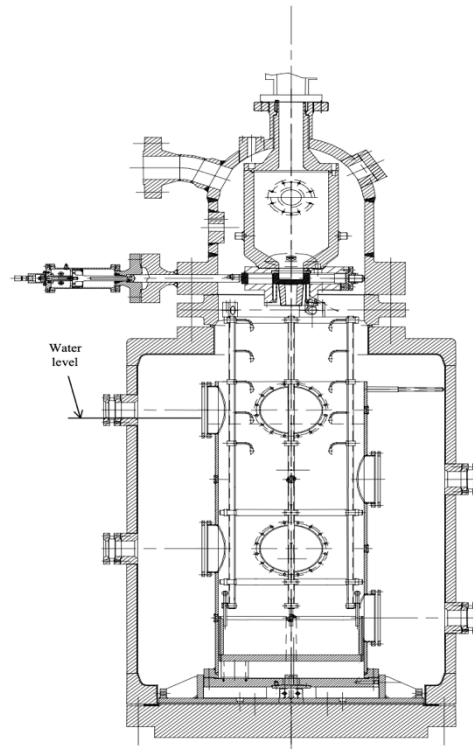


Figure 4.3: FARO facility with FAT vessel

Table 4.5: Comparison of L-series test

Test no.	19	20
Initial pressure (MPa)	5	2
Melt mass (kg)	157	96
Melt temperature (K)	3073	3173
Melt free fall in gas (m)	1,19	1,12
Water depth (m)	1,10	1,97
Free-board volume (m ³)	1,635	1,291

Melt leading edge travel time in gas (s)	0,57	0,47
Melt leading edge velocity in water (m s^{-1})	4,2	3,3
Cake on bottom (kg)	80	21
Particulate debris (kg)	77	75
Mean particle size (mm)	3,7	4,4

Water depth highly influences melt breakup-ratio and cake formation at the bottom: comparing data between L-19 and L-14 (reported in table 4.6), molten mass initial condition and flow rate are similar as well as starting pressure. However, different free fall length in gas leads at first to different jet velocity at the pool surface, followed by different pressurization: higher fall length results in higher jet velocity reflected in higher pressurization and larger debris fraction formed by jet breakup and erosion. This is coherent with particulate debris analysis at SEM: leading edge erosion confirms to be the main contributor for L-14 test FCI leading to larger fragment size, whilst in L-19 column-jet erosion is the predominant factor [72]. A comparison between cake in these tests are reported in figure 4.4 and 4.5

Dynamics of pressure role on jet breakup can be exhibited by a comparison between L-14 (5 MPa) and L-20 (2 MPa) tests: in both cases, molten jet leading-edge reaches water contact surface at the same time, indicating low influence of steam density on jet dynamic. Furthermore, pressure increase during gas phase drifting is almost the same in both tests, stressing the fact that no significant difference in gas heating took place. On the other hand, pressurization was higher in L-20 rather than in L-14 during penetration phase in water, but this could be explained by different melted mass

involved: by thermodynamic calculations it can be seen that pressurization in L-20 corresponds to similar energy release from melt to water in L-14. This leads to proof of low impact of initial pressure on jet fragmentation dynamics.

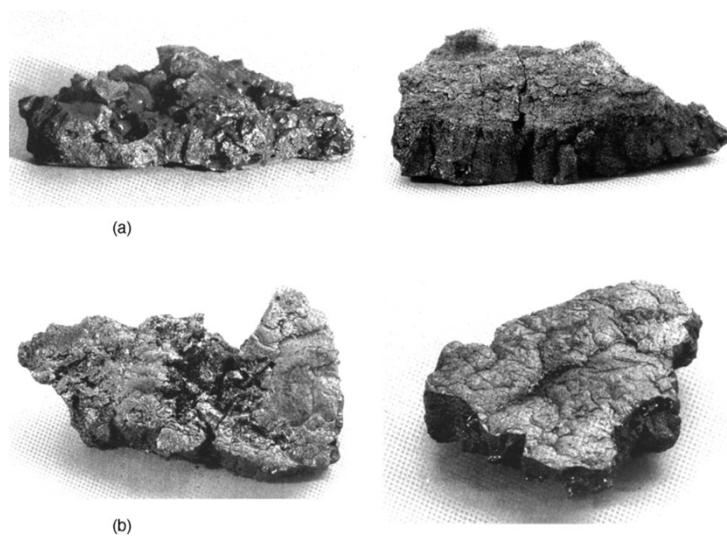


Figure 4.4: Cake formed in L-19 test (a) seen from the top (b) seen from below at contact with bottom plate



Figure 4.5: Cake formed in L-14 test

Molten mass quantity also plays a fundamental role on jet breakup understanding. Comparing data from experiments performed at same pressure boundary conditions i.e., L-14, L-08 and L-06 but different discharged quantities, it can be seen that low mass quantities up to 44 Kg do not influence breakup, pressurization and quenching behavior. In fact, higher amount of molten mass can be translated in higher pressurization due to continuous jet heating up of the gas phase while the leading edge already impinged on water and bottom plate, leading to overlapping of pressure increase both from quenching in water and gas phase. In all tests, pressurization rates reach maximum around melt-bottom contact time, indicating that melt jet breakup of leading edge is no more a contributor to steam generation, thus only erosion of the continuous molten column is the provider for pressure increase after this instant. This is an essential information for large quantity corium mass studies, leading to the necessity of evaluate erosion due to Kelvin-Helmholtz instabilities and stripping phenomena other than Rayleigh-Taylor instabilities describing just leading front breakup process.

4.3.2 FARO L.14

Faro L-14 tests involves 125 kg molten mass injection into interaction vessel, analyzing a mixture of 80% in weight of UO_2 and 20% of ZrO_2 . Test initial reference conditions are set to 5 MPa for pressure and 3073 K for corium temperature. In this test, neither debris rejection nor steam explosion were observed. Water pool depth was set to 2.05 m leading to a free fall height in gas (mixture of steam and argon) of 1.04 m. A summary of working conditions and results are reported in table 4.6

Table 4.6: FARO L-14 experimental conditions and results

MELT		
Composition (UO ₂ -ZrO ₂)	wt%	80 – 20
Zr	wt%	0
Temperature	K	3073±50
Discharged mass	kg	125
Hydrostatic head in release vessel	m	0.57
Δp delivery		Gravity
Initial discharge diameter	m	0.1
Free fall in gas	m	1.04
Delivery time	s	1
Mean mass flow rate	kg/s	125
Final discharge diameter	m	0.092
Conglomerated on bottom plate	kg	20
Mean size of fragment	mm	4.8
Melt/debris rejection		no
WATER		
Mass	kg	623
Height (water pool depth)	m	2.05
Diameter of water container	m	0.710
Initial mean temperature	K	537
Fuel/coolant mass ratio		0.21

FREE-BOARD		
Gas composition (steam – argon)	wt%	77 – 23
Volume	m ³	1.28
Initial pressure	MPa	5
Initial mean temperature	K	536
BOTTOM PLATE		
Maximum temperature increase	K	330
State	-	intact
PRESSURE INCREASE		
Before melt/water contact	MPa	0.1
Melt fall stage maximum	MPa	2.8 (t=2.4s)
Long term maximum	MPa	3.4 (t=30s)
Maximum rate		2.4
Steam explosion		No
TEMPERATURE INCREASE		
Gas phase (uppermost region of test vessel)	K	77
Water	K	28
LEVEL SWELL		
Maximum indicated by level-meters	m	1.100 (t=2.1s)
MELT DOWNWARD PROGRESSION		
Mean velocity in gas phase	m/s	2.9
Velocity at melt/water contact (estimated)	m/s	5.6

Mean velocity in water	m/s	4.8
Dimensionless breakup length L/D (a)		>20.5
ENERGY RELEASE AND QUENCHING RATE		
Energy of the melt E_{melt}	MJ	188
Energy released at first pressure maximum E_{fall}	MJ	83
Ratio E_{fall}/E_{melt}	-	0.44
E_{fall}/kg of broken up melt	MJ/kg	0.79
E_{fall}/kg of melt	MJ/kg	0.66
Maximum quenching rate P_{max}	MW	57
P_{max}/kg of broken up melt	MW/kg	0.54
P_{max}/kg of melt	MW/kg	0.46

(a) In which L is the breakup length and D being the initial discharge nozzle diameter.

Main results from this test were carried out focusing on pressure increase, water level swelling and temperature increase of test facility bottom plate. These data are listed respectively in figures 4.6 up to 4.10

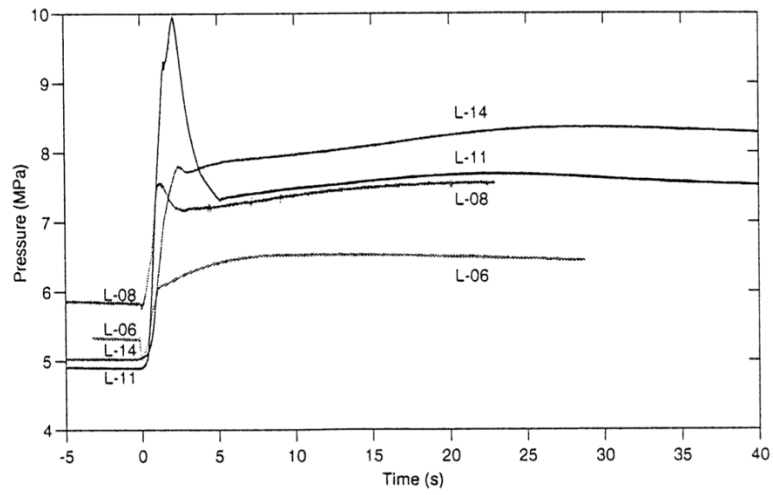


Figure 4.6: Pressure increase in FARO L-14 experiment from -5s up to 40 s

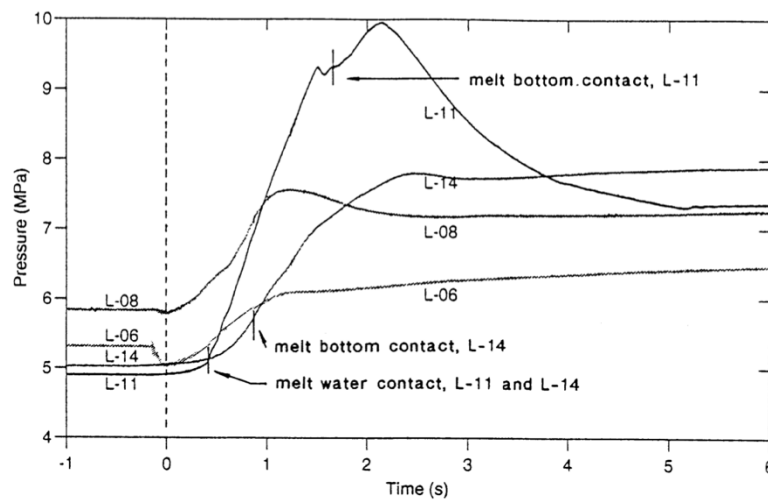


Figure 4.7: Pressure increase highlighting melt contact with water and bottom plate

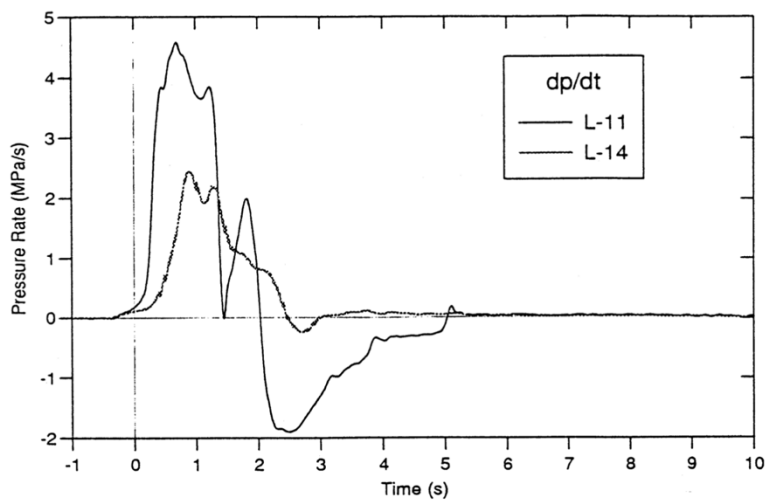


Figure 4.8: Pressure increase rate in FARO L-14 experiment

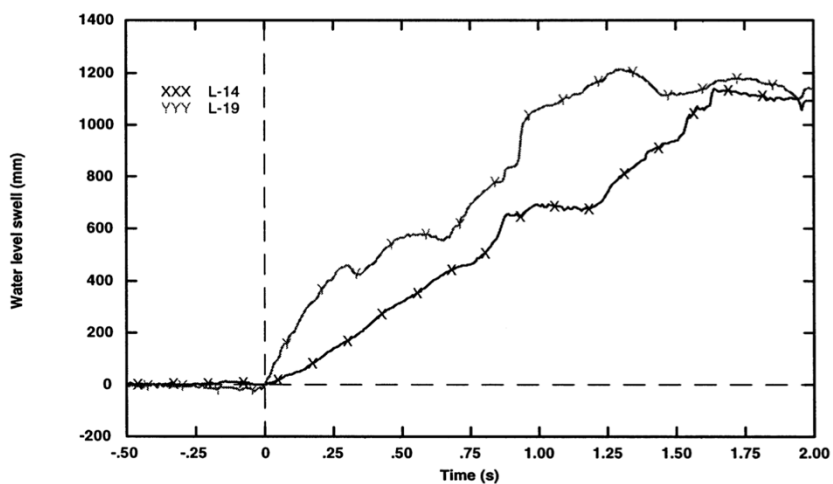


Figure 4.9: Water level swell in FARO L-14 experiment

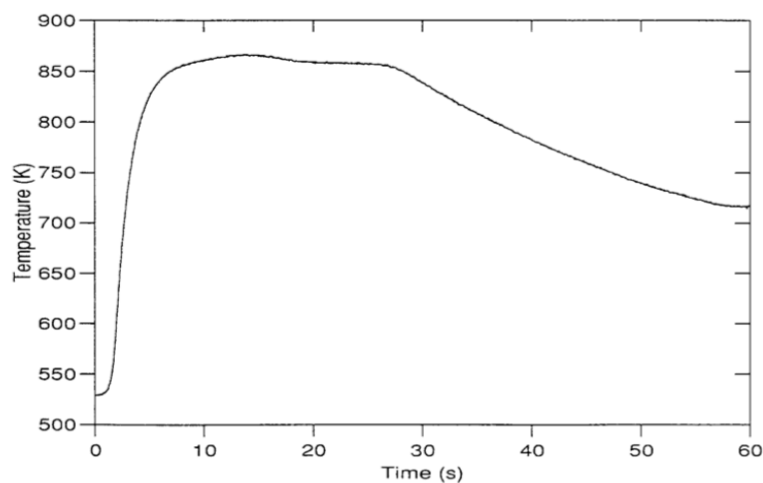


Figure 4.10: Temperature increase at bottom plate

4.4 Concluding remarks

Due to evidence of melt jet erosion and breakup investigation importance in the framework of progression of accident analysis, many experimental studies tried to catch peculiar features of FCI phenomena. This chapter presented an overview of FCI studies focusing on FARO tests, useful for the purpose of numerical verification and validation of IAE jet breakup model in SAMPSON, underlining the influence of many parameters on the process. Among many tests performed, FARO L-14 was chosen being the most suitable due to lack of natural and external triggered steam explosions and hydrogen production and large dataset available.

5. IAE jet fragmentation model numerical investigation

5.1 Introduction

As already mentioned in the previous chapters, jet breakup mechanism in the framework of FCI is an essential phenomenon for severe accident progression after core melt. The aim of this chapter is to give a preliminary numerical investigation of the jet fragmentation model implemented in SAMPSON code against FARO L-14 experiment. As stated in chapter 4, SAMPSON is a hierarchal modular code composed by 11 modules which, coupled together, are able to reproduce overall plant evolution both for normal operation and accident scenario. For the purpose of this investigation, two main modules are considered: DCA and THA. The former concerns lower plenum phenomenology regarding debris behavior and coolability analysis, whilst the latter involves thermal hydraulic calculations for the overall plant based on RELAP code analysis. Coupling between these modules is an essential task: DCA involves debris related phenomena in the lower plenum such as discharge, breakup and spreading but does not consider thermal hydraulics evolution of these stages. THA is able to overcome this lack providing an accurate analysis: if coupling is properly performed, the overall behavior in the lower head can be simulated. It should be noted that SAMPSON is still under development: many open issues are still to be addressed, not

only related to simulation capabilities but also considering many implemented mechanistic models still in need of verification and subsequent validation. Among these models, jet fragmentation will be addressed: at first, implementation of FARO test vessel geometry will be carried out, followed by DCA and THA stand-alone simulations for the present case, leading to coupling. Furthermore, in order to justify the need of fragmentation model for pressure peaks reproduction, a sensitivity analysis on THA and DCA heat exchange and pressure procedures will be carried out: this step will be crucial, ensuring jet fragmentation model importance and requirement. An analysis on this model will be finally carried out, showing that the model was not yet verified and further efforts in terms of implementation were needed for the reproducibility of the fragmentation process. A new implementation strategy will be proposed, and final results will be discussed in section 5.5.3, followed by a brief comparison of SAMPSON code with VESUVIUS steam explosion dedicated code.

5.2 DCA stand-alone analysis

5.2.1 DCA model overview

Although a brief description of this module was already given in chapter 3.3.6, an in-depth knowledge of module computational performances and aims are essential in order to achieve a complete understanding of the considered problem. DCA evaluates phenomena occurring in the lower head after core failure, concerning debris cooling after relocation for both particulate and bed, RPV heat damage and its external cooling, as well as lower head penetrations, piping damage and water influx in the gap. A debris spreading model is also provided, together with debris coolability analysis models. The former involves mass, momentum and energy conservation equations for

debris thickness and density, following an explicit resolution method for a quasi-three-dimensional scheme: as conservation equations are solved, crust generation in each mesh is taken into account based on solidification fraction as a function of specific enthalpies at solidification point and latent heat. Furthermore, Volume Of Fluid (VOF) is applied for debris spearhead analysis. On the other hand, the latter provides for a debris coolability analysis, following two different approaches based on the purpose of the simulation: detailed debris coolability model and simplified coolability model. On one hand, the detailed analysis involves Navier Stokes equations for natural convection, engaging Incomplete Cholesky Conjugate Gradient (ICCG) method for pressure analysis and SMAC method for molten leading edge transport equations: as soon as energy balance is computed, solidification is decided in case solidification fraction exceeds the critical point at which liquid properties are lost, leading to heat conductivity analysis for solid phase and natural convection for liquid phase [58]. Coordinates and mesh structure for detailed coolability model are shown in figure 5.1

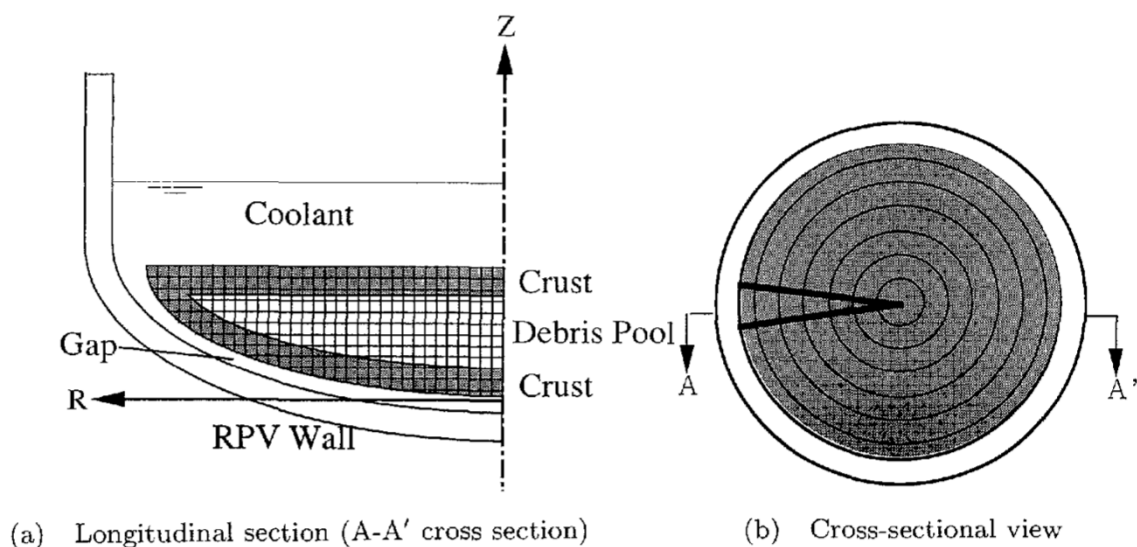


Figure 5.1: Detailed debris coolability model meshes and coordinates

On the other hand, simplified coolability analysis provides a lumped calculation, involving meshed computations only for lower crust treatment whilst molten material and upper crust are treated as a lumped hemisphere and disc respectively, as shown in figure 5.2. Energy and mass balance are solved for debris phase based on two main assumptions: molten pool is at thermodynamic equilibrium and debris thickness in lower plenum is at constant level [58].

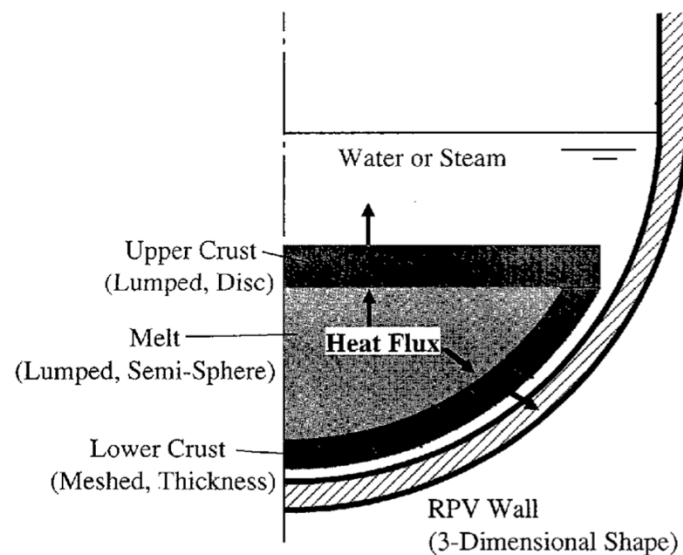


Figure 5.2: Simplified coolability model coordinates

5.2.2 FARO L-14 geometry and boundary conditions implementation

Since SAMPSON code is devoted to Fukushima accident analysis, TEPCO's NPP geometry and accidental boundary conditions were implemented: a switch to FARO geometry and L-14 experiment boundary conditions represent the first step in order

to evaluate experimental discharge transient. It should be noted that, as already stated, DCA module alone is just able to reproduce debris slumping and spreading in the lower head: what it is expected from stand-alone results is debris cooling due to heat transfer with lower head until RPV melt failure due to the lack of heat exchange with lower plenum water, treated in THA module. Among FARO L-14 experimental conditions reported in table 4.6, fundamental parameters for DCA input implementation lie in the total discharged mass (125 kg), mass flow rate (125 kg/s leading to the total discharge in one second), UO_2 and ZrO_2 weight fractions (80% and 20% respectively), initial corium temperature (3073 K), volume and specific volume of molten material components. Concerning the geometry implementation, DCA employs two sets of meshes for lower head visualization: 'RPV' for vessel analysis and 'NCD' related to debris relocation and spreading, as shown in figure 5.3 and 5.4 respectively [56].

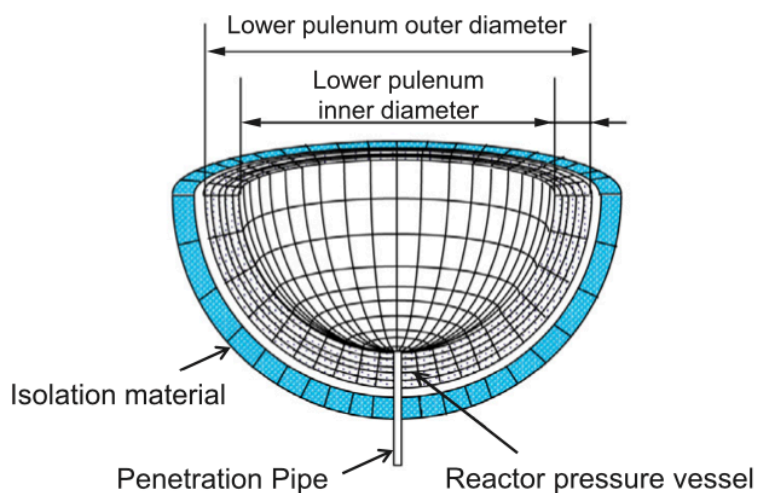


Figure 5.3: RPV mesh discretization in DCA module

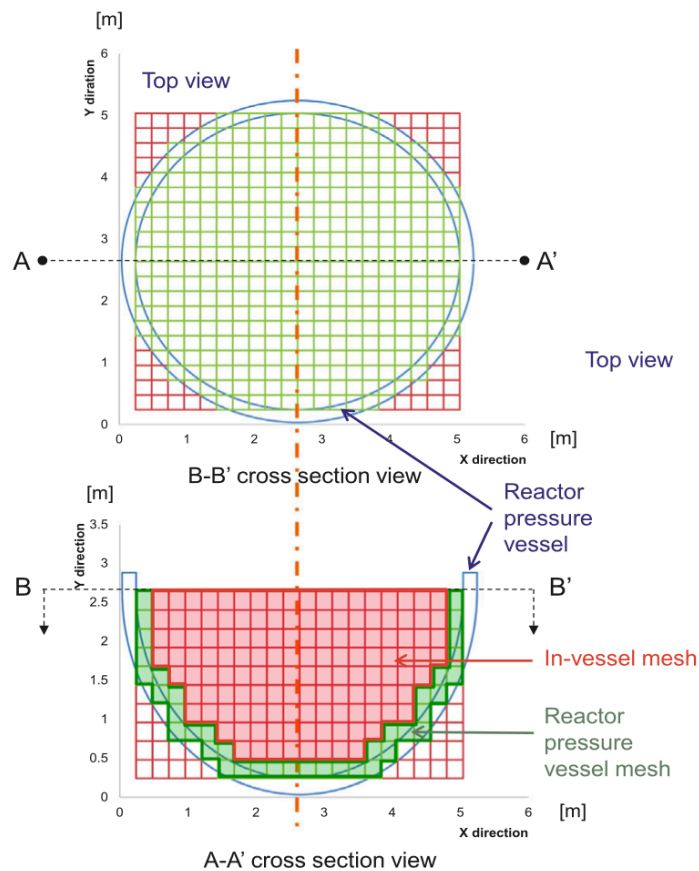


Figure 5.4: Debris mesh discretization in DCA module

As it can be seen, vessel meshes are expressed as spherical coordinates, whilst a cartesian reference system is employed for debris relocation: the interface and connections between these meshes can be visualized as a cube, expressing corium spreading, containing a hemisphere for RPV computational analysis. At first, definition of mesh number both for debris and vessel is necessary, thus changing the input files switching from Fukushima geometry (concerning a 2.4 m internal radius) to FARO test vessel (of 35.5 cm radius). Mesh number for debris relocation was kept as the original case, involving 22 meshes for x (NXNCD) and y (NYNCD) directions and 12 for z direction (NZNCD); for all three directions, 2 meshes are dummies leading to a (20, 20, 10) mesh configuration for (x, y, z) coordinate system. On the other hand,

for RPV mesh definitions a first attempt was made using the same input as Fukushima: 11 meshes in radial direction (NXRPV), 72 meshes for θ direction (NYRPV) concerning sectorization of lower head, and 5 for φ direction involving RPV thickness subdivision in concentric hemispheres. Following this path, stand-alone analysis could not be carried out successfully: due to the huge difference in Fukushima and FARO vessel dimensions, high sectorization of lower head for small scale test vessel resulted in too fine mesh for the considered geometry, leading to excessive hotspot in debris temperature (exceeding starting temperature range of over 400 K) due to code numerical instabilities which stopped the simulation because of RPV melt. For this reason, a coarser mesh definition was implemented following (11, 36, 5) path for (r, θ , φ) reference system. The final mesh definition for both debris relocation and vessel can be found in table 5.1.

Table 5.1: Mesh implementation for DCA stand-alone

Input	Fukushima	FARO
NXNCD	22	22
NYNCD	22	22
NZNCD	12	12
NXRPV	11	11
NYRPV	72	36
NZRPV	5	5
Inner radius (m)	2.4	0.355

5.2.3 DCA stand-alone results and discussion

It should be noted that, for each SAMPSON module, the possibility of subdividing the simulation in two separate transients is available. This philosophy was adopted in DCA stand-alone analysis, considering a first transient of discharge and a second evolution transient of debris spreading and cooling due to heat transfer with internal RPV wall. Simulation results are reported in figure 5.5 for RPV lower head temperature, in 5.6 for debris temperature field and spreading before restart and in 5.7 for debris temperature evolution after restart at time of RPV melt (7.502 seconds after molten material injection).

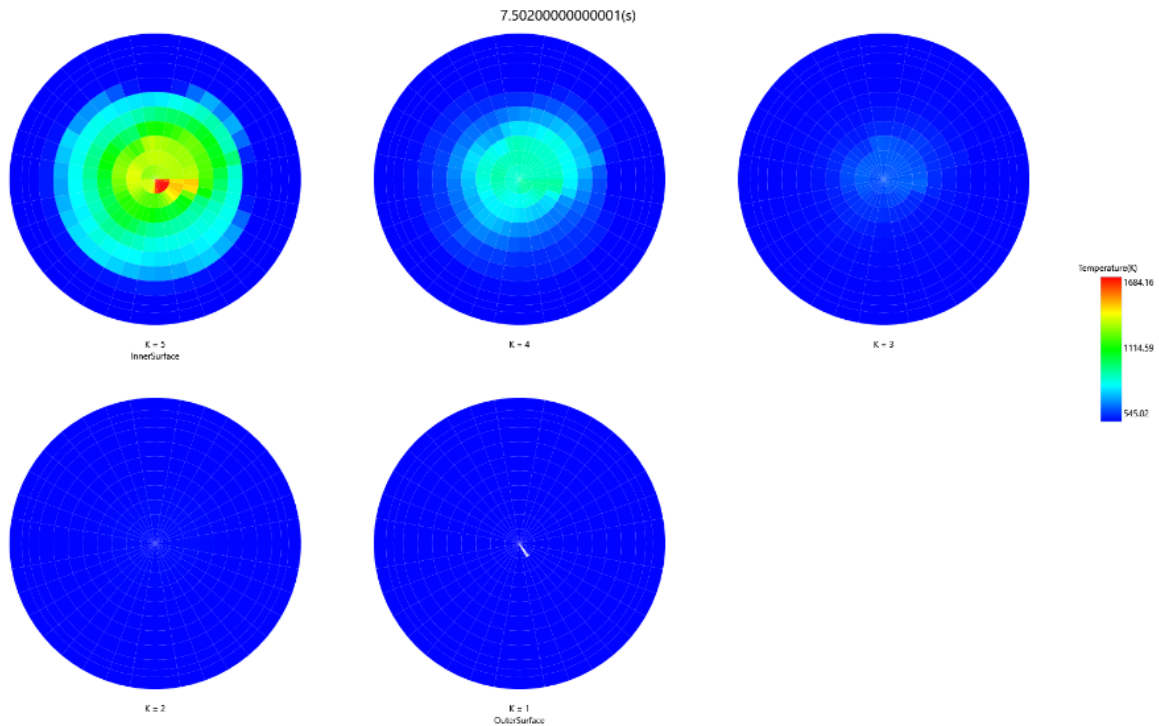


Figure 5.5: RPV lower head temperature distribution for DCA stand-alone

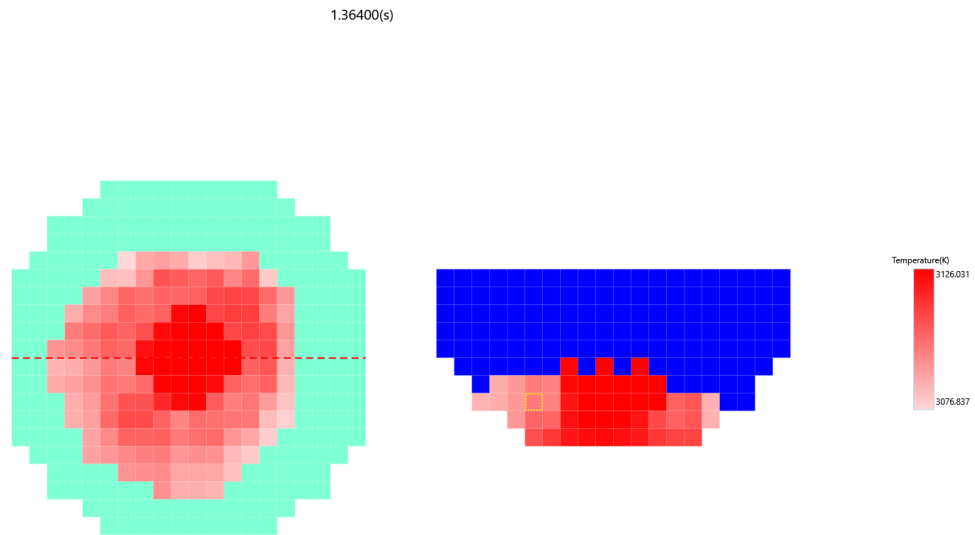


Figure 5.6: Debris spreading and temperature evolution before restart

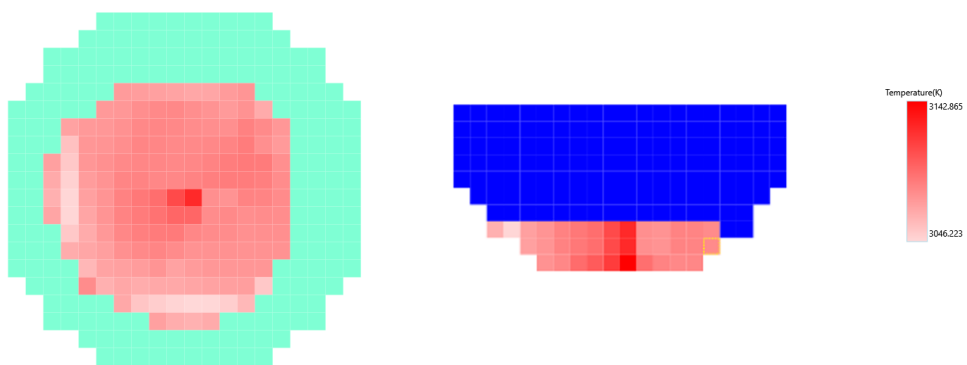


Figure 5.7: Debris spreading and temperature evolution at RPV melt time

As it can be seen from figure 5.5, RPV failure due to melt occurs at 7.502 seconds after corium slumping in the lower head. This result is consistent with the fact that in DCA stand-alone analysis no water in lower plenum is provided, leading to a direct heat exchange between molten material and RPV inner walls: shell 5, experiencing the highest temperature increase transient, represent the inner shell of the vessel, whilst shell 1, indicating the outer shell, undergoes only slight temperature changes. Concerning debris relocation and temperature evolution, some considerations should be set out. SAMPSON code was not able to simulate a discharge of 125 kg mass of corium in 1 second, but the maximum achievable was a 90 kg/s mass flow rate. The reason for this code incapability is still under investigation, perhaps due to a limiter on discharge mass as a result of smaller geometry implementation with respect to full size reactor for which the code was developed. This thesis is supported by the fact that, using Fukushima geometry, the code was able to simulate 125 kg/s mass flow rate, whilst for FARO geometry, upper limit was found to be at 90 kg/s.

Furthermore, as shown both in figure 5.6 and 5.7, debris highest temperature is 3142 K as result of some hotspots formed during simulation. Molten mass temperature was set based on a subroutine in MCRA module which, given melt composition, was able to reproduce debris enthalpy related to a specific temperature, which was set equal to 3073 K, as experimental data reported. Computed enthalpy value has then been checked with literature [73] giving a consistent result. Given a coherent enthalpy calculation, hence a correct input temperature, reasons for arising hotspots are believed to lie in the smaller geometry newly implemented with respect to the original Fukushima case: as already mentioned, a first trial discharge transient of a 125 kg/s mass flow rate was computed under experimental conditions but using original

Fukushima geometry input, leading to a sensible result for upper boundary debris temperature, as shown in figure 5.8. This enforces the idea that hotspots instabilities arising in code output are due to numerical instabilities for fine mesh: hotspots of 2300 K were observed also using FARO geometry with Fukushima mesh grid for RPV (11,72,5), furthermore supporting the theory of fine mesh related issue.

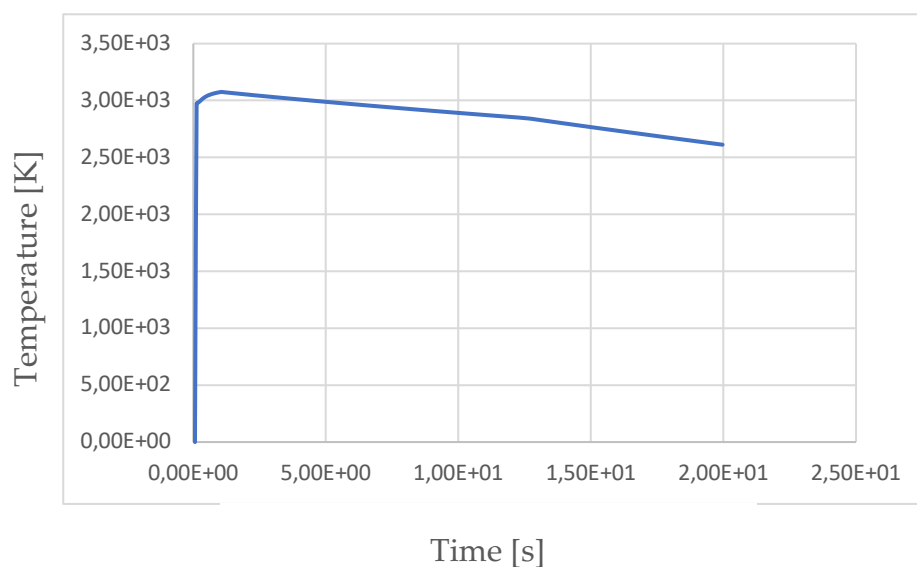


Figure 5.8: Debris temperature for FARO data input and Fukushima vessel geometry

However, a coarser mesh definition was not implemented in order not to lose computational sensitivity: this choice was supported by average debris temperature evaluation which, as reported in figure 5.9, was able to match the requirement for 3073 K. Figure 5.9, other than debris average, summarizes DCA stand-alone results, including RPV inner shell temperature behavior up to melt.

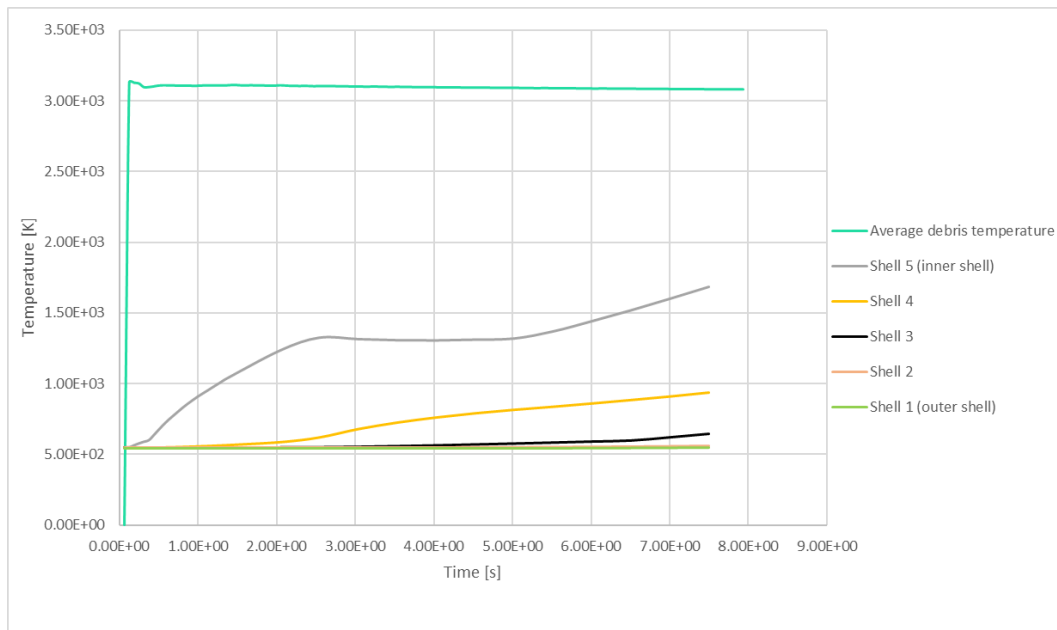


Figure 5.9: DCA stand-alone results

5.3 THA stand-alone analysis

5.3.1 THA module overview

THA module is responsible for Thermal Hydraulics Analysis for both normal operation and accidental transient: the former computational section is referred as THA1 involving transients before core melt, whilst the latter concerning accidental transient is denoted as THA2. This module implements dedicated code RELAP/MOD3 for thermal hydraulics computation based on the programming concept of control volumes, nodes and junctions: all functions of RELAP/MOD3 code including physical models and numerical solutions are inherited by THA [47]. Since THA is devoted to the analysis of the overall plant, coupling with each of SAMPSON's other modules is

necessary in order to provide for inputs and feedbacks for global NPP transient simulation. Fukushima nodalization system is reported in figure 5.10: for the sake of this dissertation concerning FCI after core meltdown, focus will be given on volume B101 concerning the lower plenum of the RPV.

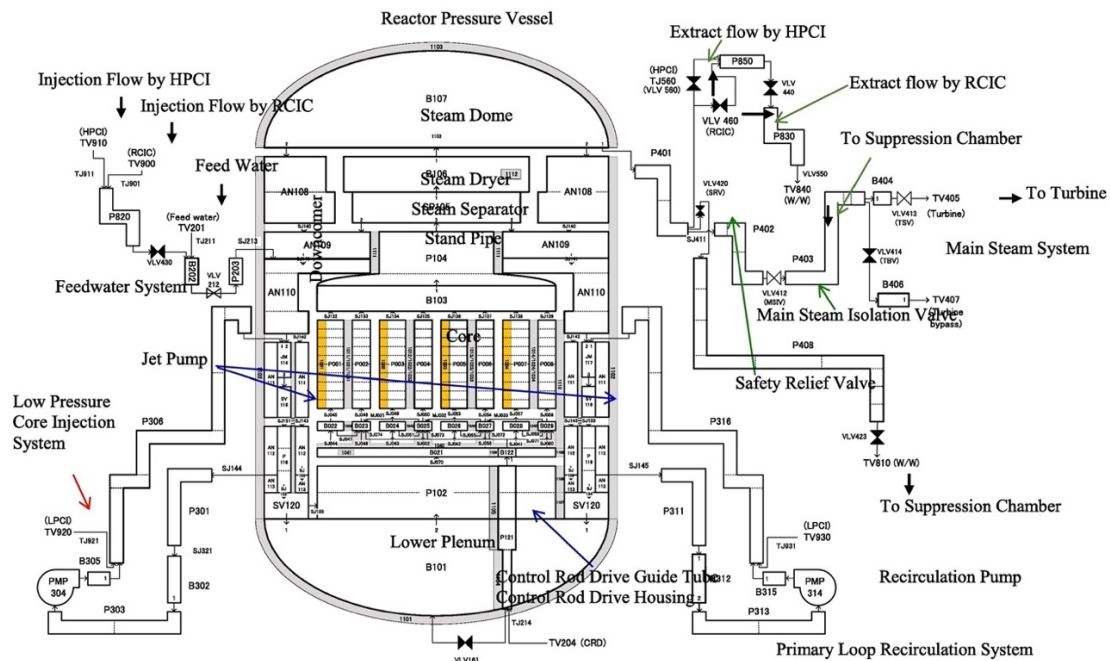


Figure 5.10: Fukushima nodalization in RELAP/MOD3

5.3.2 FARO L-14 geometry and boundary conditions implementation

As already mentioned in the previous paragraph, THA involves a control volumes approach for thermal hydraulics analysis: since DCA involves phenomena occurring in the lower plenum, identified as volume B101 in Fukushima nodalization, the first essential step in order to provide for THA stand-alone analysis is the implementation

of FARO L-14 geometry using RELAP substituting volume B101 for the current investigation scope. FARO test vessel geometry is reported in figure 5.11 as well as essential geometry and boundary conditions parameters in table 5.2

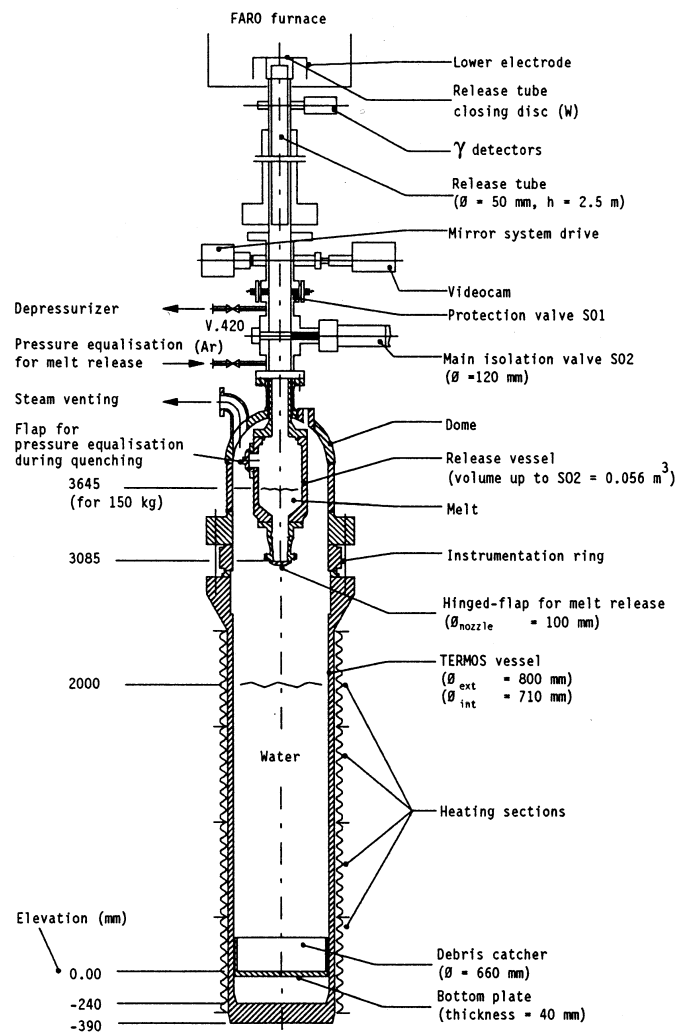


Figure 5.11: FARO test vessel geometry

Table 5.2: FARO L-14 geometry and boundary conditions

Geometry	Data	Unit of measure
Internal diameter	0.71	m
Water level	2.05	m
Gas composition	Steam 77%	-
	Argon 23%	-
Gas temperature	536	K
Water temperature	537	K
Pressure	5	MPa
Total vessel height	3.085	m

At first, FARO test vessel nodalization was carried out by means of 8 volumes for a cylindrical shape of 3.085 m in height: 5 volumes for water of 0.41 m height each and 3 volumes for gas phase mixture in the upper part of 0.354 m each. A sketch of this configuration is reported in figure 5.12. This configuration was able to reproduce good results in terms of stand-alone analysis, leading to DCA and THA coupling. Unfortunately, following this implementation, several problems related to enthalpy, pressure, and water level nonphysical computational values arose. The reason for these issues may be due to the drastic change in geometry from Fukushima to FARO test vessel: the former not only involves the lower plenum but also engages control rods driving mechanism and heat structures which are not implemented in FARO geometry. For this reason, it was believed that SAMPSON code does not consider new

geometry input files as lower plenum geometry only, but as a mixture of the above-mentioned structures.

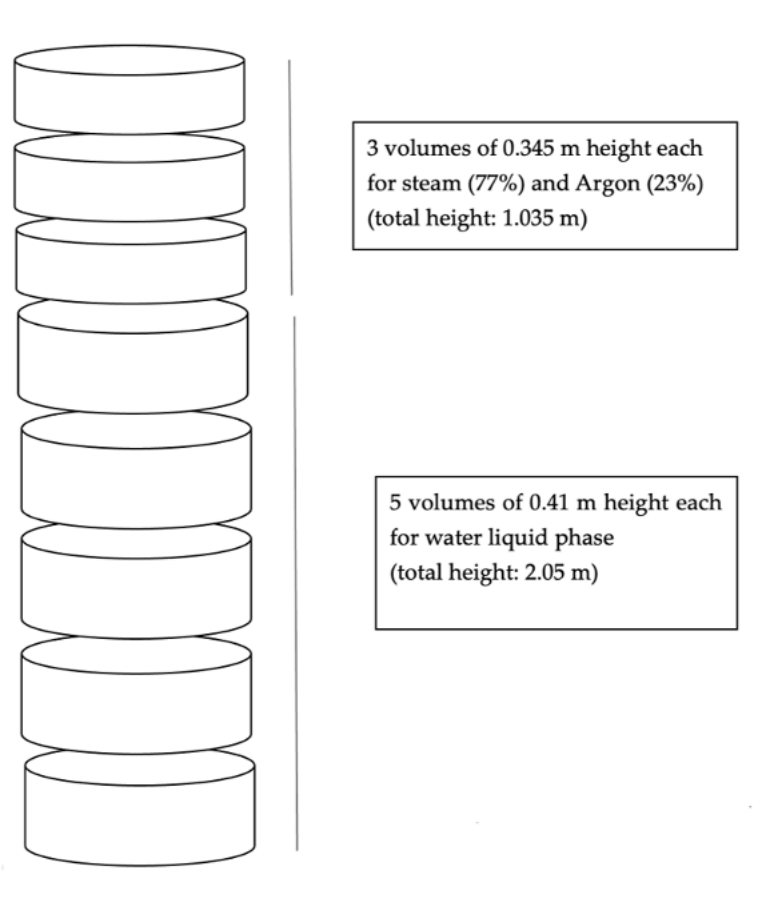


Figure 5.12: RELAP 8-volumes input for FARO vessel geometry

In order to provide for physical results in the coupling phase, a trivial input geometry for THA stand-alone was implemented, following a 2-volumes structure philosophy: one volume for liquid water phase of 2.05 m height and one for gas phase steam-argon mixture of 1.035 m height. A sketch of the final RELAP input is shown in figure 5.13.

This configuration was able to provide for consistent results both for stand-alone and coupling: results for the former will be discussed in the next section.

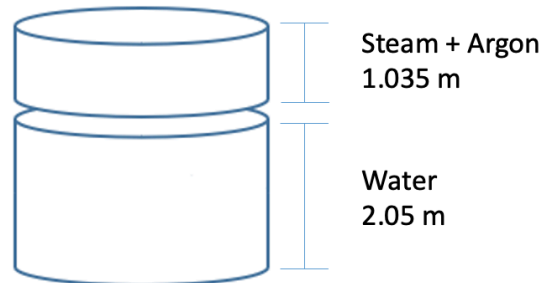


Figure 5.13: RELAP 2-volumes input for FARO vessel geometry

5.3.3 THA stand-alone results and discussion

Given the experimental data from table 5.2 and RELAP input following 2-volumes approach, THA stand-alone analysis was carried out: results are shown in figure 5.14 and 5.15 for temperature and pressure behaviors respectively, in which volume 301 refers to water whilst volume 302 to steam-argon gas phase mixture.

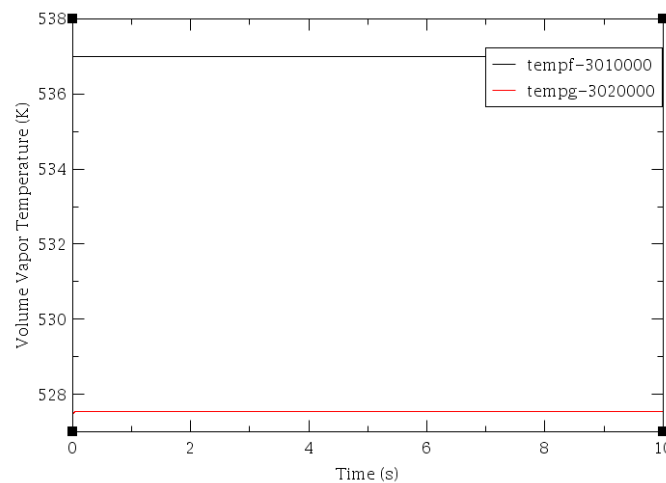


Figure 5.14: Temperature analysis in THA stand-alone

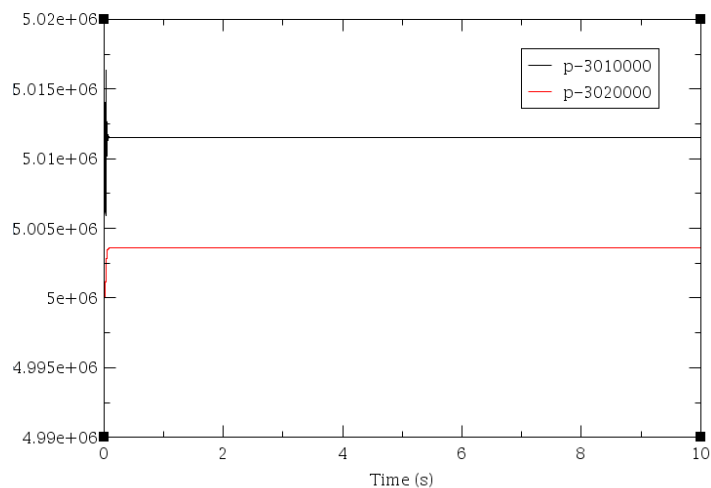


Figure 5.15: Pressure analysis in THA stand-alone

As it can be seen from figure 5.14, temperatures in the two volumes are different even if the system is at saturation conditions, due to the presence of Argon in gas phase mixture. Furthermore, temperature in gas volume was set at a lower value with respect to the saturation one provided for FARO L-14 experiment in order to match saturation pressure for steam-argon mixture at 5 MPa given the Argon partial pressure. In figure 5.15, it can be noted that pressure in liquid volume is a bit higher than 5 MPa, due to the presence of gas column represented in volume 302. As expected, this simulation is able to reproduce pressure and liquid and gas phase constant value, since no transient is involved.

5.4 DCA-THA coupling without fragmentation model

After THA and DCA stand-alone successful analysis, coupling between these modules is essential in order to achieve jet fragmentation model numerical investigation, which will be treated in section 5.5: coupling not including fragmentation model is crucial in order to justify the necessity of the model. In this paragraph, coupling results will be discussed, showing a tendency in system pressure underestimation with respect to experimental results: simulation results are not enough to support the thesis of breakup model need, unless a sensitivity analysis on pressure and energy computation is carried out in order to check the validity of SAMPSON code implemented models. As will be shown in section 5.4.1, coupling pressure analysis gives a coherent result with respect to analytical evaluation, whilst some modifications were needed in energy evaluation analysis related to heat flux computational issues. Nevertheless, even by fixing these bugs, pressure increase is not able to match experimental trend as shown in figure 5.16, leading to the necessity of the fragmentation model in order to justify high pressure increase in both experimental setup and Fukushima case.

5.4.1 DCA – THA coupling results and discussion

Once both THA and DCA stand-alone analysis were correctly carried out, by turning on both modules in SAMPSON it was possible to achieve coupling. Results are shown in figure 5.16, comparing SAMPSON computational pressure with the experimental one. It should be noted that these are the actual and final results of the simulation after some issues related to heat flux computation were fixed, as discussed in section 5.4.1.1.

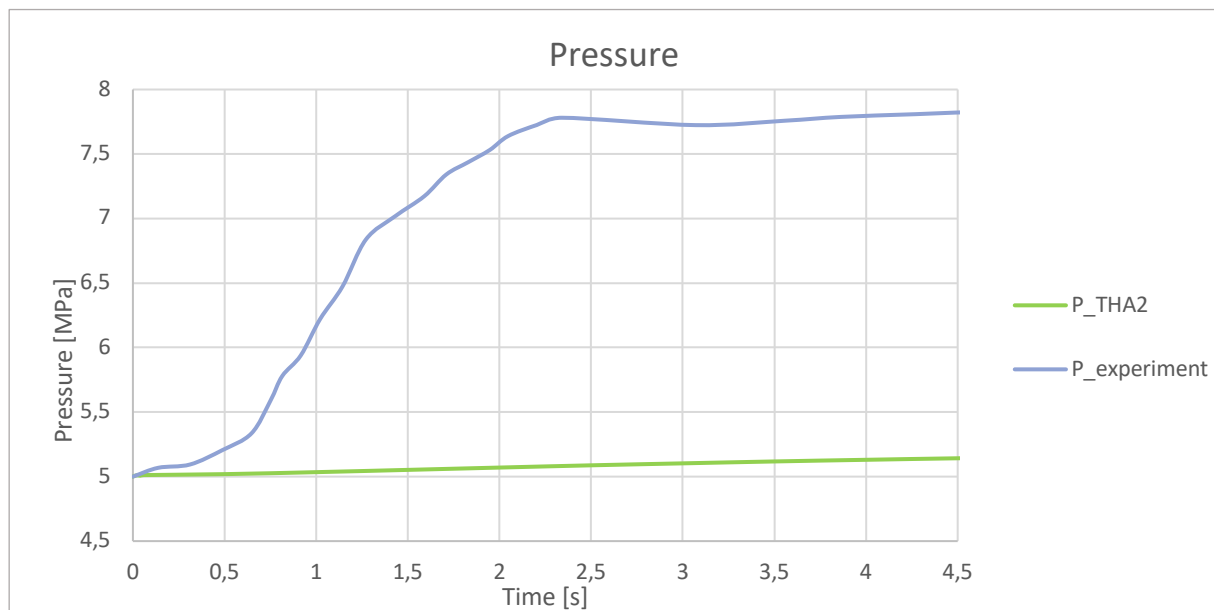


Figure 5.16: Coupling pressure result (green) compared to experimental one (blue)

As it can be seen, pressure increase provided by coupling is not able to match FARO L-14 experimental one. Since SAMPSON code is still under development, a sensitivity analysis on heat exchange between debris and water as well as on pressure calculation is essential in order to assess the necessity of the fragmentation model.

5.4.1.1 Heat exchange analysis

In this section, heat transfer process between debris and water will be analyzed by means of pool boiling heat transfer comparison between DCA computation and analytical evaluation, in order to check whether the code is able to reproduce Nukiyama boiling curve (figure 5.1 [74]) at different pressure conditions or not, considering atmospheric and 5 MPa pressures as reference cases.

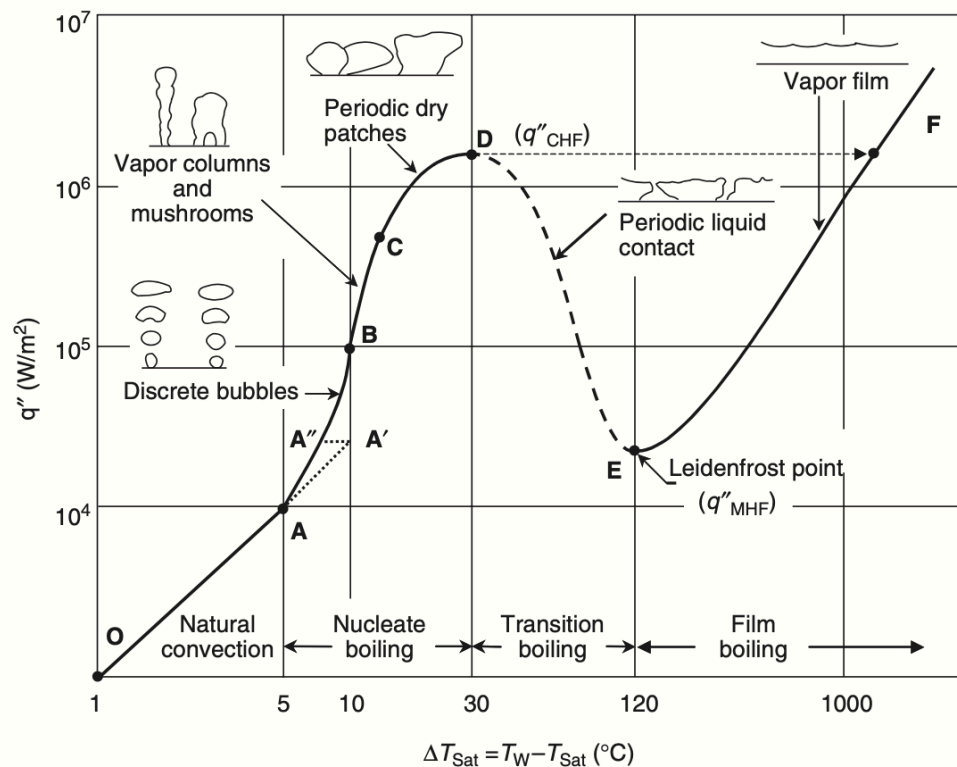


Figure 5.17: Nukiyama boiling curve

In region O-A no boiling occurs, being natural convection is the main heat transfer mechanism. At point A', corresponding to a fixed overheating, onset of nucleate boiling occurs involving bubble nucleation origination. For an imposed heat flux, superheat temperature drops to A'', leading to an hysteretic effect represented by segments A-A'-A'' which disappears for repeated boiling cycles [74]: this temperature overshoot is due to considerable increase in heat transfer due to bubble generation, leading to a decrease in temperature down top point A'' [75]. Region A''- B is known as underdeveloped nucleate boiling, in which activation nucleation sites start increasing up to fully developed nucleate boiling (region B-C) denoted by a high rate of bubble generation and growth and characterized by elevated heat exchange. At higher heat fluxes, bubble generation is so strong that at some points bubbles may

cover the whole surface such that intensive evaporation may lead to a surface drying and rewetting cycles, involving large surface area coverage by a vapor film, hence leading to a decrease of heat exchange up to the critical heat flux (CHF) denoted by point D. CHF is the maximum heat flux which can be sustained under nucleate boiling condition [74] and beyond this value two paths become available: 'heat controlled' or 'temperature controlled' systems. In case of 'heat controlled' system, a small increase in heat flux will result in burnout phenomenon, leading to a sudden switch from point D to F involving a drastic increase of wall temperature. Starting from point F by decreasing heat flux values, is possible to reach the minimum heat flux known as Leidenfrost point (E) by means of film boiling regime; by a further reduction in heat flux, nucleate boiling is reached again resulting in a hysteretic cycle [75]. On the other hand, in case of 'temperature controlled' regime, region D-E, known as transition boiling, is achievable only by means of stable temperature boundary conditions on heated surface, concerning very rapid transients of surface drying and rewetting: at Leidenfrost point, a stable vapor film is formed switching to a complete blanketing for higher temperature increase.

SAMPSON code neglects the transition boiling regime, involving calculations just for natural convection, underdeveloped and fully developed nucleate boiling and film boiling, the latter starting from a local minimum heat flux just after CHF is achieved. Results of debris-water heat exchange by means of pool boiling are reported in figure 5.18. Natural convection phase (BLNACO subroutine) computes heat flux and differential heat flux, by means of typical relations for free convection based on Rayleigh, Grashof and Prandtl numbers, up to the onset of nucleate boiling. When this value is reached, BLNUCL1 subroutine takes over aiming at underdeveloped nucleate boiling regime estimation up to the inflection point by means of a Rohsenow-type

correlation [76] including a scaling factor to take into account actual system pressure, with $m = \frac{1}{3}$ and $n = 1$:

$$q'' = \left(\frac{P_{system}}{P_{atm}}\right)^{0.7} \frac{1+3\left(\frac{P_{system}}{P_{crit}}\right)^3}{1+3\left(\frac{P_{atm}}{P_{crit}}\right)^3} \Delta h_{lg} \mu \sqrt{\frac{g(\rho_l - \rho_g)}{\sigma}} \left(\frac{c_p \Delta T}{C_{sf} \Delta h_{lg} Pr^n}\right)^{1/m} \quad (11)$$

After the inflection point is reached, fully developed nucleate boiling is taken into account in subroutine BLNUCL2, up to the critical heat flux. CHF correlation implemented in SAMPSON code is Zuber [74] [77] equation defined as follows:

$$q''_{CHF} = 0.131 \Delta h_{lg} \rho_g^{1/2} [\sigma g(\rho_l - \rho_g)]^{1/4} \quad (12)$$

As already mentioned, transition boiling is not taken into account in SAMPSON code. This aspect may be due to the fact that in nuclear power reactors main mechanism involves an 'heat flux controlled' system, leading to burnout right after CHF is reached. Perhaps, a first implementation philosophy gave relevance to the 'heat flux controlled' mechanism involving natural convection, nucleate boiling and film boiling rather than 'temperature controlled' system, hence transition boiling, also possibly due to rather difficult implementation as a result of numerical instabilities which may arise during calculations. Nonetheless, the present case involves a quenching process such that transition boiling may occur in real accident events: thus, further implementation improvement in this sense may be necessary in the future. Given this, film boiling occurs right after CHF in SAMPSON code: film boiling heat exchange contribution i.e., radiative heat transfer is taken into account in BLFILM subroutine, the former achieved by Berenson film boiling correlation for heat transfer:

$$h = 0.425 \left\{ \left[\frac{K^3 g \rho_g (\rho_l - \rho_g) h'_{lg}}{\mu_g (T_w - T_{sat})} \right] \left[\frac{g (\rho_l - \rho_g)}{\sigma} \right]^{1/2} \right\}^{1/4} \quad (13)$$

$$\text{with } h'_{lg} = \Delta h_{lg} \left(1 + 0.5 \frac{c_{p,g}(T_w - T_{sat})}{\Delta h_{lg}} \right) \tag{14}$$

As reported in figure 5.18, SAMPSON code calculation at atmospheric pressure is able to reproduce pool boiling curve, even though transition boiling is not considered. Furthermore, fully developed nucleate boiling is not taken into account, involving Rohsenow relation for heat flux up to the CHF. Even though the reason for this behavior is still under investigation, SAMPSON code is able to reproduce quite well the Nukiyama curve for pool boiling.

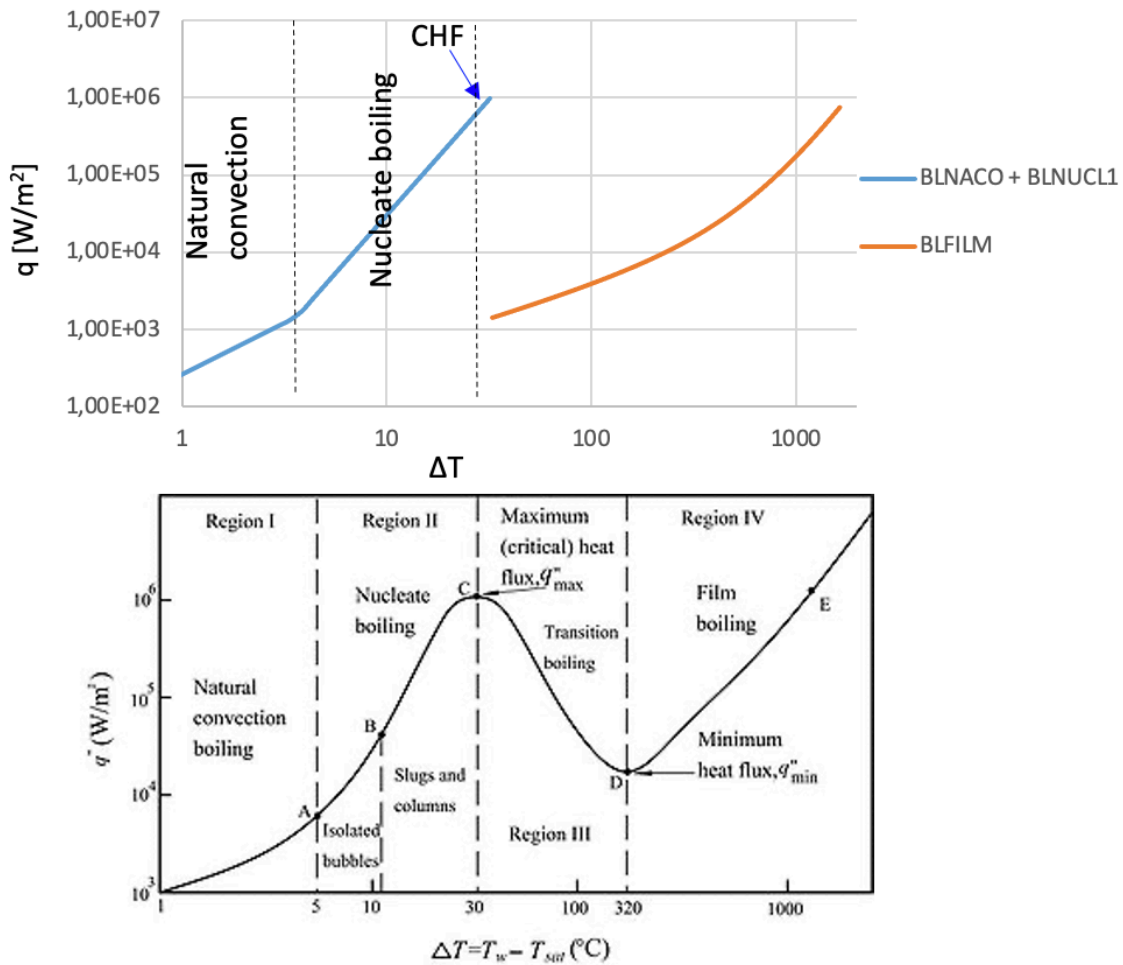


Figure 5.18: Comparison between SAMPSON calculation for pool boiling and literature at atmospheric pressure

On the other hand, many issues arose concerning calculation at higher pressure: when reproducing experimental case at 5 MPa, both underdeveloped nucleate boiling and fully developed boiling were taken into account leading to an overestimation of heat flux as shown in figure 5.19.

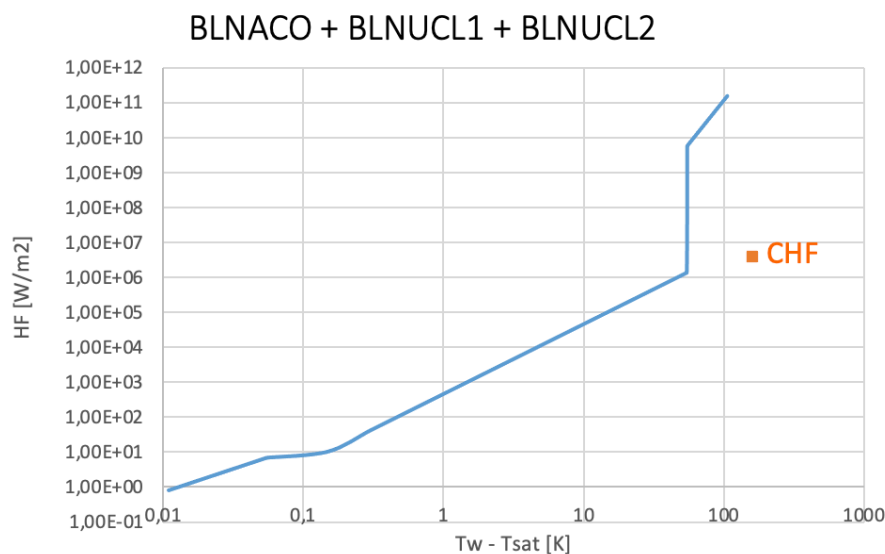


Figure 5.19: Pool boiling calculations at 5 MPa pressure

As it can be seen from figure 5.19, problems arise in the fully developed nucleate boiling transient, involving wrong heat flux calculations well above CHF threshold value such that switch to film boiling does not occur, leading to an overestimation of the heat flux. In the subroutine devoted to fully developed nucleate boiling analysis, an 'if-condition' was implemented in order to make switch to film boiling analysis possible, involving two different conditions which had to be contemporarily satisfied: a trivial one regarding heat flux value greater or equal to CHF and a specific variable NBOILCHA, a selection parameter for heat transfer choice [78] between two values (10 for boiling heat transfer and 20 for critical heat flux). In order to switch from nucleate boiling to film boiling once CHF is achieved, this variable had to be equal to 10: being

this condition always false, nucleate boiling computations continued well above CHF value leading to inconsistent results. The reason of incapability of variable update is still under investigation by IAE THA module experts, aiming at providing for accurate calculations. In order to proceed to fragmentation model investigation, a limiter on the heat flux was imposed, setting manually heat transfer choice parameter equal to 10 once CHF was achieved, leading to a correct evaluation of the overall process. It should be noted that even though this was a temporary solution, it was able to improve not only the simulation for our scope, but every ongoing simulation at IAE related to Fukushima's analysis required by TEPCO. Being a temporary solution, further investigation in the pool boiling analysis is required.

5.4.1.2 Pressure analysis

In this section a comparison between THA pressure results and analytical computation will be carried out: considering released energy in the system computed by SAMPSON as starting point, by means of an iterative procedure involving water mass evaporated and the sensible heat required to bring remaining water pool up to saturation temperature at each time step, analytical pressure will be computed and compared to simulation results. Outcomes of this process are reported in figure 5.20, proving that pressure output given by THA is adequately fitted by analytical pressure analysis. Both energy and pressure analytical analysis were carried out in order to confirm pressurization arising by molten material discharge into the lower head, without considering the fragmentation model. As shown, SAMPSON provided a coherent pressure computation, resulting in a much lower trend with respect to the experimental behavior as shown in figure 5.21. This is indeed a proof of fragmentation

model need in order to reproduce large pressurization in short transient time as in FARO L-14 experiment and Fukushima accident analysis.

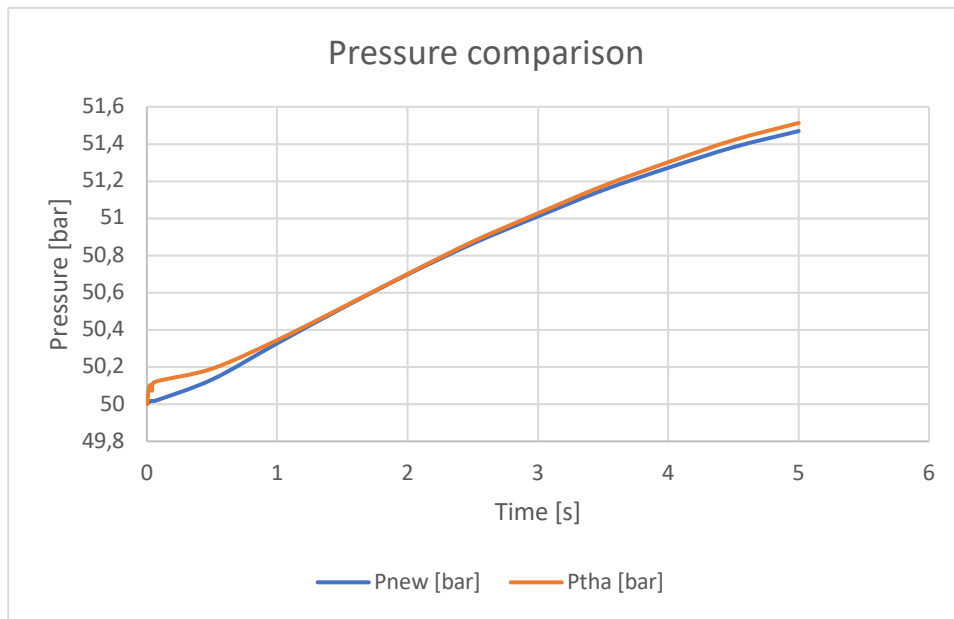


Figure 5.20: Pressure comparison between THA and analytical evaluation

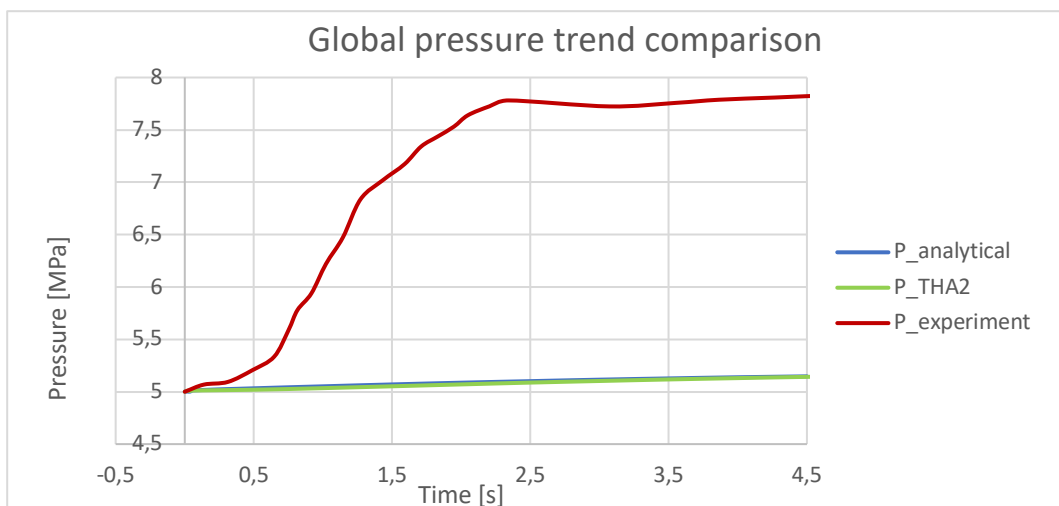


Figure 5.21: Final result of DCA-THA coupling without fragmentation model comparing experimental, analytical and computational pressure

5.5 DCA – THA coupling with fragmentation model

In this section an overview of IAE fragmentation model will be presented as well as heat exchange mechanism devoted to each step of relocation phenomena. A preliminary evaluation will lead to a code overestimation of pressure with respect to the experimental output: an in-depth analysis of the code behavior will show a discrepancy between developer's manual model and implemented model, due to lack of phenomena transient time integration implementation in the code. A trivial implementation will be carried out leading to an underestimation of pressure, whilst a well-structured implementation will be proposed for further studies and eventual validation.

5.5.1 IAE jet fragmentation model

After core failure, in case fragmentation model is turned on, four main areas of interest are taken into account from the computational point of view: molten jet and falling through gas phase, falling melt reaching water phase leading to breakup, as well as direct particulate molten material discharge from core plate falling through gas and finally quenching in water. For the sake of this dissertation, given FARO L-14 boundary conditions involving the discharge of a coherent jet through gas and liquid phases, only the former two cases are taken into account. From SAMPSON manual [47] these two situations are treated as follows:

- [Molten jet falling through gas phase](#)

This model is based on several assumptions listed below:

- Molten material jet does not break up during its falling through gas area

- Diameter of molten material jet is constant and can be regarded as having cylindrical shape.
- Temperature of molten material jet is constant during its falling through gas area
- Molten material jet falls freely due to gravity

Given the above assumptions, heat transfer rate from molten jet to gas phase is computes as:

$$Q_{jg} = \pi d_j H q_{jg} \quad (15)$$

In which d_j is the diameter of molten material jet [m], H is the active length of gas phase, whilst q_{jg} is the heat flux from molten material jet to gas [W/m^2] computed as sum of convection heat transfer and radiative heat transfer:

$$q_{jg} = q_{j,conv} + q_{j,rad} \quad (16)$$

$$q_{j,conv} = h(T_j - T_g) \quad (17)$$

By this definition, convective heat transfer coefficient must be computed, as well as average Reynolds number for the jet, free fall velocity and fall-in velocity of jet respectively.

$$h = \frac{K_g}{H} (0.037 Re_H^{4/5} - 871) Pr^{1/3} \quad (18)$$

$$Re_H = \frac{1}{H} \int_0^H \frac{\rho_g v_g(z)}{\mu_g} dz \quad (19)$$

$$= \frac{\rho_g}{15\mu_g g^2 H} \left\{ v_{j,in}^5 - (v_{j,in}^2 - 3gH)(v_{j,in}^2 + 2gH)^{3/2} \right\}$$

$$v_g(z) = v_j(z) = \sqrt{v_{j,in}^2 + 2gz} \quad (20)$$

$$v_{j,in} = \frac{4M_j}{\rho_f \pi d_j^2} \quad (21)$$

The last term involved in the heat flux calculation is radiative heat transfer defined as:

$$q_{j,rad} = F \varepsilon \sigma_{SB} (T_j^4 - T_g^4) \quad (22)$$

- Molten material jet falling through water: actual fragmentation model

This model is based on several assumptions listed below:

- Generation rate of molten material particles by molten material break-up is constant along jet surface.
- Diameter of molten material jet is constant and can be regarded as having cylindrical form.
- Almost all the heat transfer from molten material jet to water is radiative heat transfer, while convection and conduction heat transfer can be neglected.
- As falling velocity of molten material jet through water is high and as its surface area is small, temperature change of molten material jet in water can be neglected.
- Diameter of molten material particles broken up from molten material jet is constant.
- Molten material particles broken up from molten material jet fall down through water with constant velocity.
- No coagulation of molten materials nor influence of latent heat is considered.

- Heat transfer from molten materials deposited in the bottom plate to water is neglected, since it is regarded in another model (flux from particulate bed).

Given these hypothesis, heat transfer rate from molten material jet and particles broken up from it to water Q_{jl} [W] is calculated as follows:

$$Q_{jl} = \pi d_{jl} L_j q_{jl} + \pi d_B^2 N_B \int_0^{t_{B,stay}} q_{Bl} dt \quad (23)$$

In which:

d_{jl} : Diameter of molten material jet [m]

L_j : Length of molten material jet [m]

q_{jl} : Heat flux from molten material jet to water [W/m²]

q_{Bl} : Heat flux from particles generated by break-up to water [W/m²]

d_B : Diameter of broken-up particles [m]

N_B : Number of broken-up particles generated [#]

$t_{B,stay}$: Residence time of broken-up particles in water (Time until precipitation) [s]

Equation (23) is the fundamental one on which dissertation will focus in the next section.

Heat flux from molten coherent jet is computed as radiative heat transfer:

$$q_{jl} = F \varepsilon \sigma_{SB} (T_j^4 - T_l^4) \quad (24)$$

In which T_j is the average temperature of molten material jet considering the same value as in gas area.

Essential parameters for jet fragmentation model such as jet diameter and length in water, non dimensional jet breakup length by Saito's equation [20], as well as particulate diameter, number and residence time, are modelled as follows:

$$d_{jl} = d_j \sqrt{\frac{v_{j,in}}{v_{j(H)}}} \quad : \text{diameter of molten material jet in water [m]} \quad (25)$$

$$L_j = \min(H_l, L) \quad : \text{length of molten material jet in water [m]} \quad (26)$$

In which:

d_j : Flow-in diameter of jet in gas area [m]

$v_{j,in}$: Velocity of jet flowing into gas area [m/s]

$v_{j(H)}$: Velocity of jet when reaching water surface [m/s]

H_l : Water level [m]

L : Break-up length of molten material jet (from Saito's Equation) [m]

$\frac{L}{d_{jl}}$: nondimensional break-up length defined as

$$\frac{L}{d_{jl}} = 2.1 \frac{\rho_f^{1/2}}{\rho_l} Fr^{1/2} \quad (27)$$

Fr : Froude Number (using jet water approaching velocity as jet velocity)

The present case involves particle generated from a coherent jet which should be treated differently with respect to the simpler the case in which particulate is flowing directly into water, since broken particle generation position may be distributed on various height level. Hence, assuming that broken-up particles are generated from jet with the same rate throughout their path and that the falling velocity is constant, average falling distance H_B is equal to that of all particles falling from height of half-length of jet, implying that calculation is made assuming that all the broken-up particles fall down distance of H_B at constant velocity:

$$H_B = H_l - \frac{L_j}{2} \quad (28)$$

On the heels of this, diameter and number of broken-up particles, and residence time are calculated respectively as follows:

$$d_B = \frac{We\sigma}{\rho_l v_f^2} \quad (29)$$

$$N_B = \frac{6M_j R}{\rho_f \pi d_B^3} \quad (30)$$

$$t_{B,stay} = H_B / v_f \quad (31)$$

In which M refers to jet flow rate, whilst R represent the breakup rate of particles from molten jet defined as:

$$R = \min\left(1, \frac{H_l}{L}\right) \quad (32)$$

It should be noted that, in case break-up length is shorter than water depth, all the jet shatters, leading to a unitary break-up rate whilst, in the opposite case, water depth H_l divided by break-up length L is regarded as break-up rate, while obviously molten particles generation follows this rate.

Moreover, heat flux model for detached particles from the jet is the same of simpler case involving particle directly flowing in the lower plenum: this treatment involves the second term on the right-hand side of equation (23) of which a brief description is reported below for which the subscript 'f' refers to particulate whilst 'l' refers to water in lower plenum.

The most relevant term is the heat flux from particulate debris denoted as q_{Bl} in equation (23). At first, relative velocity between particles and water must be assessed, involving a large friction resistance between the two phases. Particulate velocity

through water can be expressed as follows:

$$v_f = \sqrt{\frac{4}{3} \left(\frac{\rho_f}{\rho_l} - 1 \right) \frac{g d_B}{C_D}} \quad (33)$$

In which C_D represent the resistance factor expressed by Ishii and Zuber equation:

$$C_D = \frac{2}{3} d \left(\frac{g \Delta \rho}{\sigma} \right)^{1/2} \left\{ \frac{1 + 17.67(1-\alpha)^{9/7}}{18.67(1-\alpha)^{3/2}} \right\}^2 \quad (34)$$

Given this, heat flux from molten particles to water is computed as sum of radiative and convective heat transfer. The former is given as:

$$q_{rad} = F \varepsilon \sigma_{SB} (T_f^4 - T_l^4) \quad (35)$$

In which:

T_f	: Temperature of Molten Materials	[K]
T_l	: Water Temperature	[K]
T_s	: Saturation Temperature of Water	[K]
F	: Shape Factor (1.0)	
ε	: Radiation Absorption Rate	
σ_{SB}	: Stefan - Boltzmann Constant	[W/m ² K ⁴]

On the other hand, convective heat transfer is given by:

$$q_{conv} = h(T_f - T_l) \quad (36)$$

In which h is the convection heat transfer assessed by Epstein and Hauser equation considering film boiling:

$$h = 2.5 \frac{\lambda_g \rho_l d |v_f - v_l|}{\mu_l} \left(\frac{\rho_g}{\rho_l}\right)^{1/4} \left(\frac{\mu_l}{\mu_g}\right)^{1/4} \left\{ \frac{1}{24A} + 0.405 \left(\frac{B}{A}\right)^4 \right\}^{1/4} \quad (37)$$

Where:

$$A = \frac{c_{pg}(T_f - T_s)}{Pr_g \Delta h_{lg}}$$

$$B = \left(\frac{\rho_l}{\rho_g}\right)^{1/4} \left(\frac{\mu_l}{\mu_g}\right)^{1/2} \frac{c_{pl}(T_s - T_l)\delta_T}{Pr_l^{1/2} \Delta h_{lg}}$$

$$\delta_T = \begin{cases} 1 & (T_l \leq T_s) \\ 0 & (T_l > T_s) \end{cases}$$

In which T_s is the liquid saturation temperature, whilst T_f is the molten particle temperature computed starting from energy conservation equation:

$$\frac{dT_f}{dt} = \frac{6q_{Bl}}{\rho_f C p_f d} \quad (38)$$

Involving q_{Bl} which is the heat flux transferred from molten particle to water as sum of contribution from radiative and convective heat transfer just discussed in equations (35) and (36):

$$q_{Bl} = q_{conv} + q_{rad} \quad (37)$$

This model was applied to the FARO L-14 geometry of coupled DCA-THA simulation, in order to see whether pressure increase trend could be fitted: simulation results and discussion are reported in next section.

5.5.2 Fragmentation model results and discussion

As extensively described in the previous section, molten jet falling from core plate impinges water surface and travels a certain distance before breaking up into particles. The total heat flux in the fragmentation model is given by two main contributions: one related to continuous jet not yet fragmented and one from particles generated from broken-up jet, the latter involving a higher heat exchange surface which leads to a higher heat flux, hence pressurization. A schematization of the heat transfer process based on equation (23) is reported in figure 5.22.

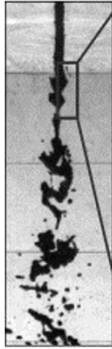
$$Q_{jl} = \underbrace{\pi d_{jl} L_j q_{jl}}_{\text{Heat transfer from remaining jet}} + \underbrace{\pi d_B^2 N_B \int_0^{t_{B,stay}} q_{Bl} dt}_{\text{Heat transfer from broken up particles}}$$


Figure 5.22: Fragmentation model heat flux contributions

Preliminary results of the fragmentation model applied to DCA-THA coupling involving FARO L-14 geometry and boundary experimental conditions are reported in figure 5.23. It should be noted that his simulation involves many fixed parameters

given by experimental data such as breakup ratio, jet diameter, water pool depth, particles diameter and molten jet mass flow rate, in order to check the validity of implemented equations whether reproduction of experimental results was achievable or not. Furthermore, two simulations entailing the same boundary condition except for molten jet mass flow rate were carried out and compared: one involving mass flow rate of 90 Kg/s for a discharge time of 1.39 s (original simulation data used from DCA stand-alone analysis) and another reproducing a longer discharge transient of 52 Kg/s for 2.4 s. The reason behind this was trying to catch as accurately as possible the maximum experimental pressure increase reported at 2.4 seconds. Results of these simulation compared to FARO L-14 outcome is reported in figure 5.23, whilst in figure 5.24 debris particulate and molten phase visualization is reported.

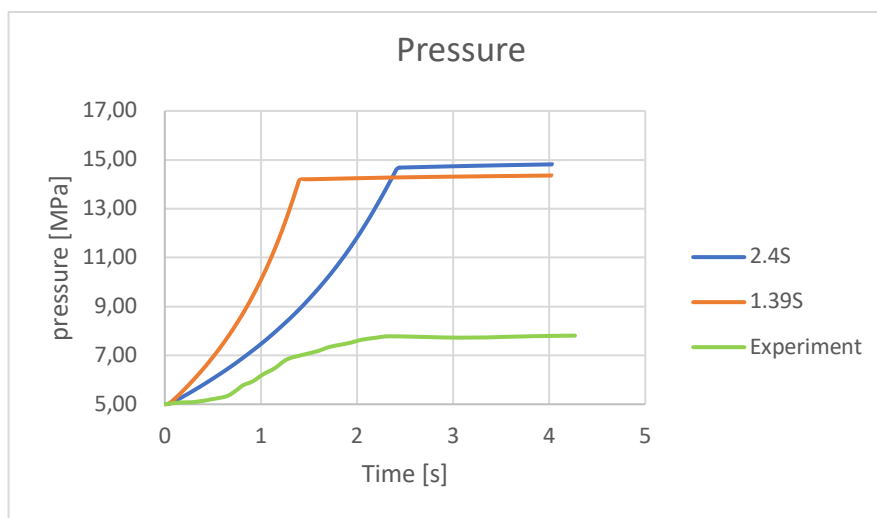


Figure 5.23: Fragmentation model preliminary results

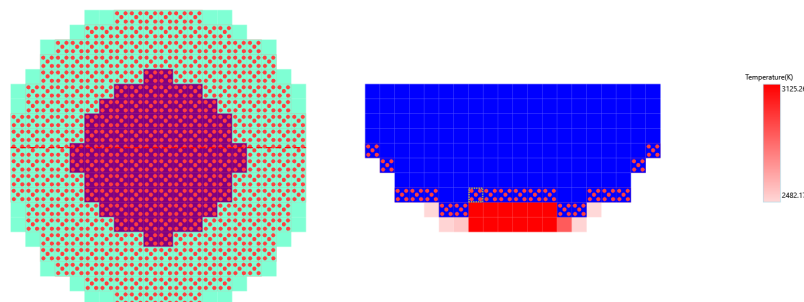


Figure 5.24: Debris visualization in the lower head after fragmentation

As it can be seen from figure 5.23, pressurization resulting by computational analysis is much higher than experimental results even though key model parameters are fixed. Although in IAE records the model resulted as fully implemented and verified but yet not validated, an in-depth analysis of the implemented model must be carried out: as already mentioned throughout this whole dissertation, SAMPSON code is still under development so further analysis is required in order to assess the validity of the implemented model. Since high pressurization is attributable to a high heat exchange, three subroutines involved in this task depending on debris state (particulate, molten or bed) were analyzed:

- DCAMcore: computes the heat exchange both for melt and particles during the transient (fragmentation model) involving film boiling correlations.
- Debflux: computes the heat exchange for the particle bed which is generated at the bottom of the test vessel during relocation involving natural convection heat exchange.

- **Ncdflux:** computes the heat exchange for the melt phase at the bottom of the test vessel during and after relocation time, entailing pool boiling equations for fully developed nucleate boiling.

Following an in-depth analysis of heat exchange values provided by these subroutines, it was assessed that the highest values were delivered by DCAMcore, involving the overall process of fragmentation entailing all equations described in section 5.5.1. Hence, the focus of the study was put primarily on this subroutine, especially on equation (23) for heat exchange mechanism, reported hereafter for simplicity:

$$Q_{jl} = \pi d_{jl} L_j q_{jl} + \pi d_B^2 N_B \int_0^{t_{B,stay}} q_{Bl} dt$$

At first, by simple dimensional analysis, an error was spotted throughout the whole manual: N_B is reported as number of particles generated, whilst instead this value refers to particle generation rate leading to a unit of measure of $[\frac{\text{number of particles}}{s}]$. Furthermore, following the dimensional analysis approach related to the second term of the right-hand side of the equation, the source of the high heat exchange problem was found: even though records stated the fully implementation and verification of the model, on the manual the heat flux given from broken-up particles q_{Bl} is integrated in time in order to provide for a coherent dimension for heat transfer Q_{jl} [W], whilst the implementation of this integral was not taken into account in the code leading to a non-evaluation of the particulate residence time. Given that heat flux was not integrated in time, hence not multiplied by a time step from the computational point of view, the resulting values were much higher than reality.

Since the lacking part in the implementation is the hardest one, at first a trivial attempt of fulfillment was set by multiplying heat flux calculation by the time step. Results of this first attempt are reported in figure 5.25. As it can be seen, even though results are

not fitting the experimental trend a coherent behavior is shown: pressurization is higher than the DCA-THA coupling without the fragmentation model (reference curve is the one at 1.39 s transient time discharge) but lower than experimental behavior, due to the fact that generated particles from broken-up molten jet reach the bottom plate in just one time step, as side effect of lack of residence time accounting. Hence, low pressurization is given as a result of lower heat exchange surface available with respect to the real case during the whole transient.

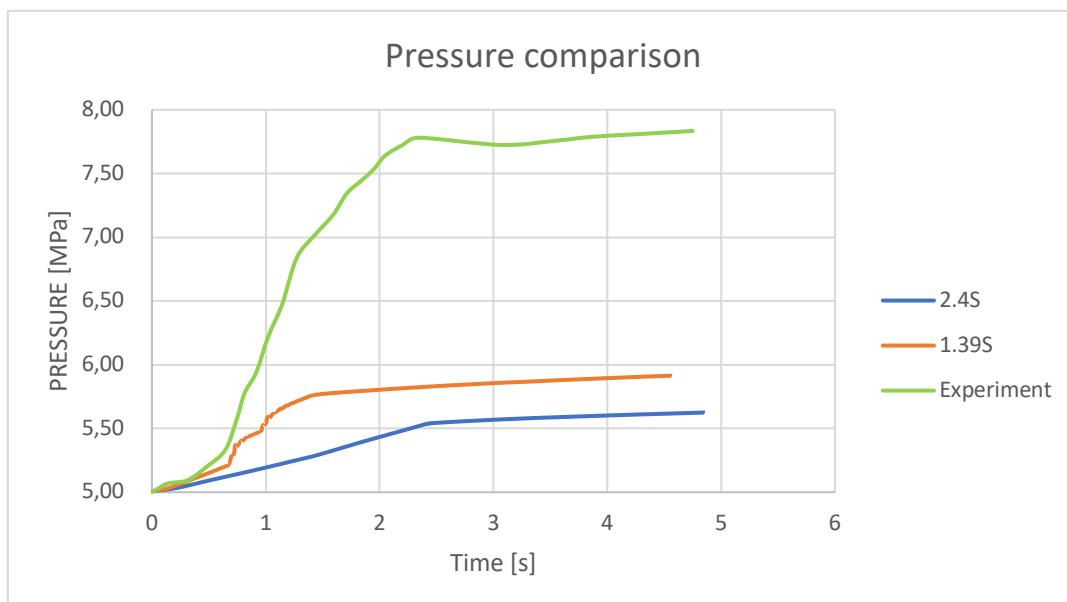


Figure 5.25: Fragmentation model results for trivial implementation

Since residence time of particulate molten broken-up material is essential in order to achieve a consistent simulation of the phenomena, an implementation model strategy was proposed: a complete description can be found hereafter, highlighting hypothesis on which this strategy relies on as well as implementation results.

5.5.3 Implementation strategy proposed for IAE jet fragmentation model

This model, representing a simplified strategy to properly account for residence time, relies its basis on two main assumptions:

- Jet fragmentation occurs as soon as molten material jet reaches water surface, hence jet breakup length is not taken into account.
- By the first hypothesis, residence time is set to be equal to the time needed for the particles to go through the whole pool.

Given these assumptions, expected trend would result in heat flux (hence pressurization) overestimation since time for particle quenching is higher than the real case scenario where breakup length is considered. Final results will be shown in figure 5.27. The idea behind this strategy relies on a layer-type structure for simulation evolution: at each time step, since breakup-ratio is fixed, the same number of particles will be generated from the breakup of the coherent jet: this set of particles is considered as a 'layer'. After a given discharge time, a fixed number of layers (groups of particles) will be formed: the number of these groups are given as:

$$N_{layer} = \frac{t_{discharge}}{\Delta t} \quad (34)$$

As discharge transient ends, the first layer of particles formed will be at a certain height of the water pool (in case of FARO L-14 it will not be at the bottom, since residence time (taken a 3 seconds) is higher than discharge time of 1.39 s): number of layers (hence particles) in the system will remain constant up to the time in which the first layer of generated particles reaches the bottom. At a certain time $t^* = t_{discharge} + \Delta t$ the first layer will disappear from DCAMcore subroutine, appearing as debris bed

involving Debflux subroutine for natural convection heat exchange analysis: from this point on, at each time step layers number will start decreasing up to the time in which the last particle group reaches the bottom. At this given time DCAMcore will no longer be used and heat exchange will be computed only in Debflux for debris bed cooling and Ncdflex for RVP calculation. It should be noted that N_{layer} not only represents particle groups but is an index of time steps number required for fragmentation model heat exchange analysis. A schematization of the above-described process implemented in DCAMcore is given below in figure 5.26.

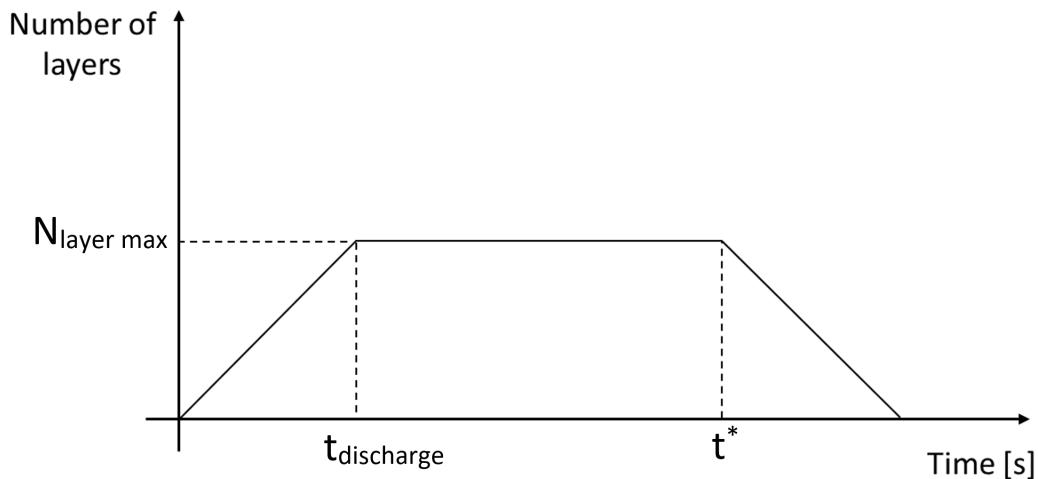


Figure 5.26: Sketch of implementation philosophy for model update

Heat exchange is computed as sum of contributions from all layers in the system at each time step, involving temperature update for each layer at each time step, providing for accurate quenching process analysis. Results of this implementation for FARO L-14 geometry compared to experimental pressure are reported in figure 5.27. As it can be seen, pressure trend is overestimated even though of same order of magnitude of experimental data: this is perhaps due to the assumption concerning

break-up length neglect which leads to a higher residence time of particles inside the lower head with respect to the original case, higher heat exchange thus higher pressurization. It should be noted that this simulation is referring to the original case of 90 Kg/s mass flow rate discharge given experimental data concerning size particle, breakup ratio and velocity as input having fragmentation model's heat exchange and pressurization analysis as purpose.

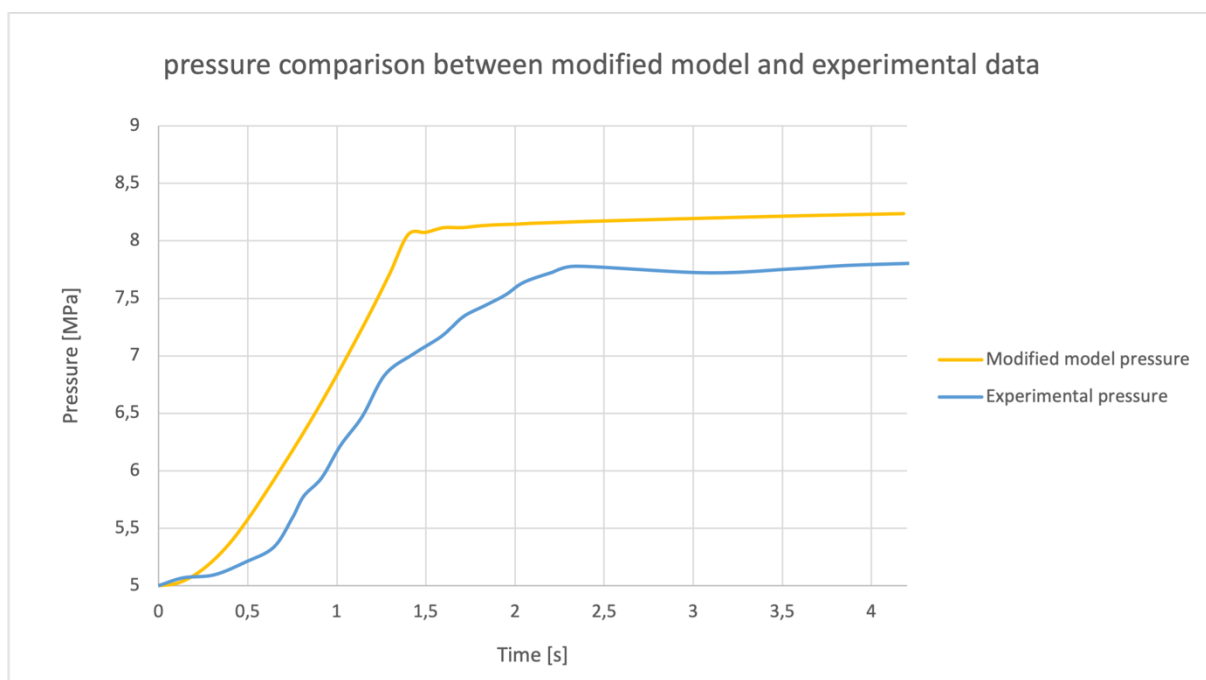


Figure 5.27: Pressure trend comparison between experimental and newly implemented model results

Further developments of this work would take advantage of sensitivity analysis on these parameters to check whether the code is able to match experimental data for other initial values as well as removal of hypothesis on jet break-up length since this is a key parameter for fragmentation model analysis as extensively discussed in chapter 2. Furthermore, it should be pointed out the existence of a dedicated code for

steam explosion known as VESUVIUS code, developed by IAE, which is usually run as a stand-alone code given its capability of prediction of the overall steam explosion process including jet fragmentation, but which may also be coupled to SAMPSON as an extension module in case of necessity. A brief overview of VESUVIUS dedicated code and its models concerning jet fragmentation are reported in next section, providing for a comparison case with SAMPSON code.

5.5.4 Comparison with VESUVIUS steam explosions dedicated code

VESUVIUS dedicated code for steam explosions, developed by NUPEC in the framework of the IMPACT project at the end of the '90s, aims at analyzing the overall process of jet fragmentation leading to steam explosions, involving computation for four different components (liquid phase, gas phase and both molten continuous and dispersed phases) which can be treated individually. One of the peculiar features of VESUVIUS code is the capability of analyzing Kelvin – Helmholtz instabilities, essential traits in fragmentation model analysis as extensively discussed in chapter 2, as part of the breakup process, involving vapor film model conservation equations combined with Epstein and Fauske surface instabilities model as well as break-up rate from molten jet model [79]. Molten jet modeling is treated with a 1D axial symmetric geometry as reported in figure 5.28, involving parabolic shaping for leading edge analysis and cylindrical vertical shape for jet inner core.

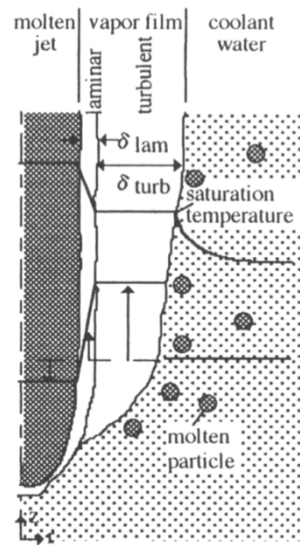


Figure 5.28: VESUVIUS geometry modeling for molten jet

Key parameter for fragmentation modeling resides in the vapor film development analysis: mass and momentum equation are computed to provide for vapor film thickness and velocity, both influencing KHI growth rate at the jet surface. Vapor film involves two separate layers: laminar profile close to jet surface, which thins out at leading edge proximity with respect to turbulent layer, which is instead developed at the external boundary side. Transition point from the former to the latter has been widely investigated but yet an agreement had not been reached: VESUVIUS code involves an intermediate value for turbulent transition Reynolds number between Schlichting [80] and Burger [81] models. It should be noted that this is one of the few user input parameters in a fully mechanistic code. Starting from transition Reynolds number, laminar film thickness is derived leading to evaluation of steam generation and heat flux at vapor-coolant interface. Furthermore, Epstein and Fauske model is taken into account for KHI disturbance wave number and growth, considering solution for the extremes case of thin and thick vapor film. The assessment of these instability waves are essential in the framework of jet fragmentation since during their

growth they may lead to break-up involving particles departure from jet surface, as shown in figure 5.29: when wavelength grows beyond a given amplitude denoted by a_1 , crest breakoff occurs, reducing the wavelength to a_2 , considered to be half of the most probable wavelength during the process [79]. This behavior leads VESUVIUS computations towards jet breakup mass rate Γ by means of the following equation:

$$\Gamma = N \frac{4}{3} \left(\frac{d_b}{2} \right)^3 \rho_j \frac{\Delta z}{\lambda} \quad (35)$$

In which N is the number of particles of a given diameter d_b generated from molten jet of density ρ_j by means of a single wave of length λ , and Δz is the computational cell width. Wavelength value is computed in different ways depending on thin or thick film case following Epstein and Fauske model.

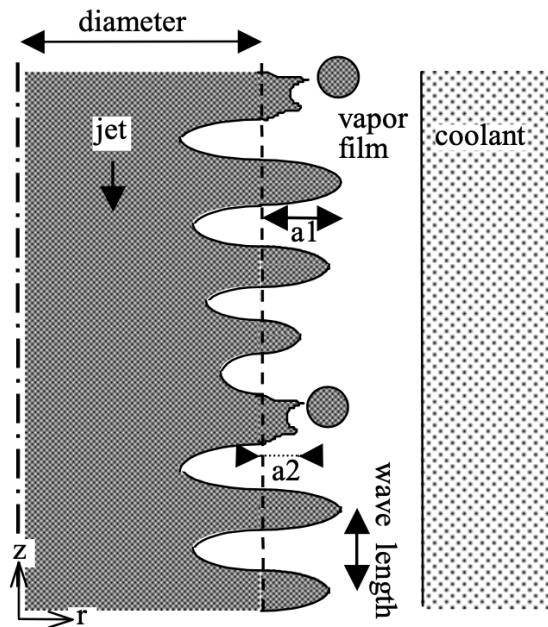


Figure 5.29: Particles break-off from molten jet due to KHI

VESUVIUS code's jet fragmentation model is very detailed and completely mechanistic, involving complex phenomena modeling such as KHI development of jet surface that are not taken into account in SAMPSON model. Since VESUVIUS is already verified and validated against FARO L-28 experiment [82], its fragmentation model could be included in SAMPSON code DCA jet breakup analysis: this would provide a coherent and strong implementation structure, even if computational time would suffer due to the high complexity of this model with respect to the less mechanistic one provided in SAMPSON code.

5.5.5 Concluding remarks

This chapter was devoted to SAMPSON code jet fragmentation model numerical investigation against FARO L-14 experiment. As broadly discussed, SAMPSON is still under development thus many computational instabilities may arise as seen in DCA module stand-alone for debris temperature hotspots. SAMPSON code instabilities are a fundamental issue to be addressed in the near future, by means of numerical algorithms verifications, in order to achieve a strong and stable computational analysis: investigations on these issues are still ongoing, to check whether instabilities are numerical or physical related, being this discrimination a fundamental starting point for code development strategy in terms of convergence and stability achievement. Furthermore, investigation towards heat exchange mechanism implemented in the code must be carried out to improve global simulation results as shown in section 5.5.2, not only strictly related to the present case but to all IAE simulations, as well as various model verification in order to check for their numerical validity and real effective implementation. SAMPSON jet fragmentation model may

provide for good results taking advantage of a strong implementation strategy as shown in section 5.5.3: even though the proposed implementation model was quite able to reproduce experimental pressure trend, this is not enough in order to decide whether the model is validated or not, such that more efforts in implementation direction will be needed. A further step sacrificing in computational time could be the incorporation of VESUVIUS code's jet fragmentation model into SAMPSON. Following the strategy of implemented models' verification and investigation, SAMPSON code's ambitious goal of being a strong mechanistic code could be achieved in the following years.

6. Conclusions and future developments

The present work has focused on jet fragmentation model, an ultimate complex phenomenon to assess in case of severe accident scenario. Starting from IAEA definition of nuclear accident involving events beyond DBA such as a large LOCA, a brief overview of phenomena leading to core failure, hence discharge of molten material in the lower head involving the fragmentation process during FCI, has been given, highlighting the necessity of numerical codes in order to simulate the overall NPP state, during both normal operation and severe accident condition, to provide for both benchmark studies and safety improvement. Starting from the '80s after TMI nuclear accident, several computer codes were developed among which, in this dissertation, MELCOR, ASTEC, MAAP and SAMPSON are taken as references for a computational structure and capability comparison. These codes are referred as 'integral' being able to simulate the overall plant behavior, whilst other codes such as RELAP and VESUVIUS are 'dedicated' codes devoted to simulation of one specific event or part of the NPP. On one hand, some differences may be spotted among the abovementioned codes especially in terms of NPP behavioral phenomena modeling and implementation, depending on whether mechanistic or lumped analysis are taken into account. On the other hand, all codes share the necessity of numerical verification and validation against experimental data: many research centers devoted their efforts

towards experimental studies in order to provide for a consistent set of data for several phenomena investigation and modeling, as well as basis for severe accident codes validation. At first, a brief overview of experimental campaigns was given highlighting differences based on the scope and scale of investigation, whether regarding a single component failure or integral study. Furthermore, among several experimental examined phenomena, focus was given on FCI assessment highlighting the need of crucial investigation aspects for the phenomena description i.e., melt and coolant compositions, steam explosions and premixing stages. Emphasis was later given on FARO L-series experiments, devoted to jet fragmentation of uranium oxide melt occurring during FCI, investigating the influence of fundamental parameters such as melt quantity and composition, water depth and initial pressure on quenching and melt/water mixing behavior by means of comparison between tests denoted by different boundary conditions. Water pool depth seems to influence the breakup ratio: given a constant vessel height, lower pool height, resulting in higher free fall length in gas, led to higher pressurization due to higher jet impingement velocity as entering the pool. This high pressurization effect can be also encountered in tests sharing the same water pool depth hence same fall in gas, but different discharged mass: for low values of molten mass, no appreciable difference was spotted in pressurization and quenching behavior, whilst higher discharged mass resulted in higher pressure increase effect. This result is related to two main mechanisms involved in the jet breakup process: Taylor – Rayleigh instabilities (RTI) occurring at jet leading edge and Kelvin – Helmholtz instabilities (KHI) arising at jet side surface. Higher pressure increases in the high discharged mass case with respect to the lower one is attributed to the latter instability: even though a maximum of pressurization occurred at leading edge bottom contact time, further pressurization behavior is due to the lateral erosion of the jet given by KHI, since RTI at leading edge are no longer available due to the

lack of an actual leading edge, since contact with bottom plate already occurred. KHI can so be considered as an essential process during jet breakup phenomena, such that their inclusion in a jet fragmentation model treatment is essential. As later shown, for the last part of the present dissertation entailing numerical investigation of SAMPSON jet fragmentation model, FARO L-14 was chosen as reference case among L-series experiment due to extensive results availability, lack of natural and external triggered steam explosions and no hydrogen production.

On the heels of these numerous experimental works and pioneering mathematical studies on the global FCI process, many models were developed for jet fragmentation phenomena. Due to the complexity of this process involving many intertwined disciplines, no accordance on a unique model, able to account for all the factors coming into play, is reached by the scientific community. Key effects during breakup events can be summarized as hydrodynamic instabilities effects such as the above-mentioned KHI, RTI and boundary layer stripping, and thermal effects including boiling, internal pressurization and solidification effects. Boiling effects take into account bubble growth and nucleation during molten material quenching process as cause of breakup: one of the most accredited models based on this effect is the one proposed by Henry and Fauske (1976), even though it does not take into account the triggering mechanism for bubble nucleation, acting as a starting point for fragmentation. Hydrodynamics and boiling effects consider only external forces as active mechanism for breakup: this is not enough to explain the extensive fragmentation during FCI, such that other internal effects must be considered. Internal pressurization effects entail the liquid entrapment theory: encapsulation of liquid droplets inside the molten phase may lead to internal pressure increase up to rupture. One of the most accredited models for this theory was delivered by Kim and Corradini (1984): this model is unique, providing not only for physical theoretical explanation of the process but also for a complete

mathematical description of each step of the process. At last, fragmentation may also arise in the solidification phase due to high thermal stresses, caused by change in crystalline structure, or even stress redistribution. This dissertation provided for a global state of art of the factors involved in the breakup process, providing for a complete view of the phenomena which will be useful in the practical numerical investigation of IAE jet fragmentation model implemented in SAMPSON code against FARO L-14 experiment. SAMPSON code is a hierarchic modular code, developed by NUPEC - IAE, involving 11 modules which, if coupled, are able to simulate the overall state of the NPP or eventually accident progression. Main modules taken into account for the present work were THA and DCA, the former devoted to thermal-hydraulics calculation based on RELAP code, whilst the latter dedicated to phenomena occurring in the lower plenum after core failure, involving molten material discharge hence extensive fragmentation of the jet. As shown, DCA and THA stand-alone and coupling analysis were carried out implementing FARO L-14 test vessel geometry and boundary conditions, highlighting the necessity of further development efforts to check for code instabilities and implemented models i.e., debris hotspots in temperature, models for pool boiling mechanism: as extensively pointed out, SAMPSON code is still under development so such issues will be fixed as development phases will proceed in the next years, achieving the ambitious goal of a complete, strong and fully mechanistic code. Furthermore, investigation on jet fragmentation model was carried out: at first the model seemed to overestimate pressure but an in-depth sensitivity analysis on heat flux hence pressurization showed that the manual model was only half-implemented, neglecting the hardest part concerning time evolution of the phenomena. A trial trivial implementation just multiplying by the time step showed a tendency in pressure underestimation due to the fact that particulate debris reached the lower head bottom plate in just one step, hence low heat

flux was considered in the pressurization evaluation. A more evolute implementation strategy was then proposed and implemented, even though ignoring jet breakup length parameter: as expected, pressurization was a bit higher with respect to the experimental one, even though the same order of magnitude was achieved. This tendency can be explained by the hypothesis of jet breakup upon impact with water pool neglecting breakup length, leading to a higher particulate residence time in the water pool, hence higher heat exchange and pressure increase with respect to the real case. Further developments could take advantage of two main strategies depending on computational time costs requirements: on one hand, the implementation of the above-proposed strategy entailing the implementation of breakup length essential feature for phenomena description could lead to consistent result with relatively low computational costs whilst, on the other hand, VESUVIUS steam explosion code's jet breakup model, which is already validated against FARO L-28 experiment, could be merged into SAMPSON code. This latter strategy would surely improve fragmentation phenomena evaluation even though computational time would increase given the complex and high detailed model implemented.

Bibliography

1. **INSAG, International Nuclear Safety Advisory Group.** *Defence in depth in nuclear safety*. Vienna : IAEA, International Atomic Energy Agency, 1996.
2. **Sehgal, Bal Raj.** *Nuclear Safety in Light Water Reactors - Severe accident phenomenology*. s.l. : Academic Press Elsevier, 2012.
3. **IAEA, International Atomic Energy Agency.** *Safety of nuclear power plants: design - safety requirements*. Vienna : s.n., 2000. Vols. Safety Standard Series No. NS-R-1.
4. **S.R. Kinnersly, J.N.Lillington, A. Porracchia, K. Soda, K. Trambauer, P. Hoffmann, Y. Waaranpera, R. A. Bari, C. E. L. Hunt, J. A. Martinez.** *In-vessel core degradation in LWR severe accidents: a state of art report to CSNI*. s.l. : NEA, January 1991.
5. **Peter Hoffmann, Sigfried J. L. Hagen, Gerhard Schanz, Alfred Skokan.** Reactor core materials interactions at very high temperatures. *Nuclear Technology*. September 1989, Vol. 87, 1.
6. **P. Hoffmann, M. Markiewicz.** Chemical behavior of (Ag, In, Cd) absorber rods in severe LWR accidents. *Nuclear Technology*. 1990, Vol. 87.
7. **Yuzuru Iwasawa, Yutake Abe.** Melt jet-breakup and fragmentation phenomena in nuclear reactors: A review of experimental works and solidification effects. *Progress in nuclear energy*. 2018, Vol. 108.
8. **R. M. Summers, R. K. Cole, Jr., R. C. Smith, D. S. Stuart, S. L. Thompson, S. A. Hodge, C. R. Hyman, R. L. Sanders.** *Melcor computer code manuals*. Albuquerque, NM 87185-0739 : Sandia National Laboratories , 1995. Vol. 1.
9. **Siniša Šadek, Davor Grgic, Zdenko ŠimiT.** Application of ASTEC, MELCOR, and MAAP Computer Codes for Thermal Hydraulic Analysis of a PWR Containment Equipped with the PCFV and PAR Systems. *Science and Technology of Nuclear Installations*. 2017.
10. **L.L. Humphries, R.K. Cole, D.L. Louie, V.G. Figueroa, M. F. Young.** *MELCOR Computer Code Manuals Vol. 2: Reference Manual*. Albuquerque, NM 87185-0748 : Sandia National Laboratories, 2015.

11. **P. Chatelard, N. Reinke, S. Arndt, S. Belon, L. Cantrel, L. Carenini, K. Chevalier-Jabet, F. Cousin, J. Eckel, F. Jacq, C. Marchetto, C. Mun, L. Piar.** ASTEV V2 severe accident integral code main features, current V2.0 modelling status, perspectives. *Nuclear Design and Technology*. 2014, Vol. 272.
12. **P. Chatelard, N. Reinke.** *Overview of the integral code ASTEC V2.0*. s.l. : INSTITUT DE RADIOPROTECTION ET DE SURETE NUCLEAIRE, Direction de la Prévention des Accidents Majeurs and GESELLSCHAFT FÜR ANLAGEN- UND REAKTORSICHERHEIT (GRS) mbH, 2009.
13. **R. Wachowiak, EPRI.** *Use of MAAP in Support of Post-Fukushima Applications*. Palo Alto, California : EPRI, June 2013.
14. **A.A. Amsden, F. H. Harlow.** The SMAC method: a numerical technique for calculating incompressible fluid flow. *Journal of Computational Physics*. 1971, Vol. 8, 2.
15. **M. L. Corradini, B. J. Kim, M. D. Oh.** Vapor explosions in light water reactors: a review of theory and modeling . *Progress in Nuclear Energy* . 1988, Vol. 22, 1.
16. **Haraldsson, H. O.** Breakup of jets and drops during premixing phase of fuel coolant interaction. 2000.
17. **M. Burger, S. H. Cho, E. V. Berg, A. Schatz.** Breakup of melt jets as pre-condition for premixing: modeling and experimental verification . *Nuclear Engineering and Design*. 1995, Vol. 155.
18. **G. Charalampous, C. Hadjiyiannis, Y. Hardalupas.** Comparative measurement of the breakup length of liquid jets in airblastatomisers using optical connectivity, electrical connectivity and shadowgraphy. *Measurement*. March 2016, Vol. 88.
19. **Taylor, G. I.** The dispersion of jets of metals at low melting point in water. *The scientific papers of Sir Geoffrey Ingram Taylor* . s.l. : Cambridge University Press , 1963.
20. **M. Saito, K. Sato, S. Imahori.** Experimental study on penetration behaviors of water jet into Freon-11 and liquid nitrogen. *ANL Proceedings: National heat transfer conference* . 1988.
21. **M. Epstein, H. K. Fauske.** Application of the turbulent entrainment assumption to immiscible gas-liquid and liquid-liquid system. *Chemical Engineering Research and Design* . 2001 , Vol. 79.
22. **Y. Iwasawa, Y. Abe.** Melt jet-breakup and fragmentation phenomena in nuclear reactors: a review of experimental works and solidification effects. *Progress in Nuclear Engineering* . 2018, Vol. 108.
23. **K. Moriyama, Y. Maruyama, T. Usami, H. Nakamura.** Coarse breakup of a stream of oxide and metal melt in water pool . *JAERI Research*. 2005-2017.

24. **H. W. Jung, K. Moriyama, H. S. Park.** Experimental revisit of melt jet breakup length correlation for fuel-coolant interaction. *NUTHOS-11*. 2016.
25. **Rayleigh, F. R. S.** On the capillarity phenomena of jets . *Royal Society Publishing*. 1879.
26. **Taylor, F. R. S.** The instability of of liquid surfaces when accelerated in a direction perpendicular to theri planes . *Proceedings of the Royal Society of London* . 1950.
27. **Sharp, D. H.** An overview of Rayleigh - Taylor instability. 1983.
28. **A. Sharon, S. G. Bankoff.** Propagation of Shock Waves Through a Fuel/Coolant Mixture Part I: Boundary Layer Stripping. *ASME*. 1978.
29. **D. L. Swift, L. Baker Jr.** Experimental Studies of the High-Temperature Interaction of Fuel and Cladding Materials with Liquid Sodium. *Proceedings of the Conference on Safety, Fuels, and Core Design in Large Fast Power Reactors*. 1965.
30. **L. C. Witte, T. J. Vyas, A. A. Gelabert.** Heat Transfer and Fragmentation during Molten Metal/Water Interactions. *J. Heat Transfer*. 1973, Vol. 95.
31. **R. P. Anderson, D. R. Armstrong.** Comparison between vapor explosions models and recent experimental results. *AIChE SymposiumSeries*. 1974, Vol. 70, 138.
32. **L. Caldarola, W. E. Kastenberg.** On the Mechanism of Fragmentation during Molten Fuel/Coolant Thermal Interactions. *Proceedings of Fast Reactor Safety Meeting*. April 1974.
33. **Long, G.** Explosions of Molten Aluminum in Water-Cause and Prevention. *Metal Progress*. 1957, Vol. 71.
34. **L. C. Witte, J. E. Cox, A. A. Gelabert, T. J. Vyas.** Rapid Quenching of Molten Metals. *University of Houston Report*. 1971.
35. **F. E. Brauer, N. W. Green, R. B. Mesler.** Metal/Water Explosions. *Nuclear Science and Engineering* . 1968, Vol. 31.
36. **Shins, H.** The Consistent Soiling Model for Fragmentation in Mild Thermal Interaction- Soundary Conditions. *SecondSpecialist Meeting on Fuel/Na Interactions in Fast Reactor*. 1973.
37. **Kazimi, M. S.** Theoretical Studies of Some Aspects of Molten Fuel-Coolant Thermal Interactions. *Science Doctorate Thesis*. 1973.
38. **Zyszkowski, W.** On the Mechanism of Heat Transfer at a Strong Accidents in Reactor Core. *Reactor Heat Transfer. Proc. Int. Mtg*. 1973.
39. **K. H. Hsiao, J. E. Cox, P. G. Hedgecoxe, L. C. Witte.** Pressurization of a Solidifying Sphere. *J. Applied Mechanichs*. 1972, Vol. 72.

40. **R. B. Knapp, N. E. Todreas.** Thermal Stress Initiated Fracture as a Fragmentation Mechanism in UO₂-NaFuel-Coolant Interaction. *Nuclear Engineering and Design*. 1975, Vol. 35.
41. **R. E. Henry, H. K. Fauske.** Nucleation Characteristics in Physical Explosion. *Third Specialist Meeting on Sodium-Fuel Interactions in Fast Reactors*. 1976.
42. **R.E. Henry, H. K. Fauske.** Nucleation processes in large-scale vapor explosions. *J. Heat Transfer*. 1979.
43. **Buchanan, D. J.** Penetration of Solid Layer by a Liquid Jet. *Journal of Physics: Applied Physics*. 1973, Vol. 6.
44. **B. Kim, M. L. Corradini.** Recent Film Boiling Calculations: Implication on Fuel-Coolant Interactions. *Fifth International Meeting on Thermal Nuclear Reactor Safety*. 1984.
45. **B. Kim, L. Corradini.** Modeling of small-scale single droplet fuel-coolant interaction. *Nuclear Science and Engineering*. 1985.
46. *PWR and BWR plant analyses by Severe Accident Analysis Code SAMPSON for IMPACT Project.* **Hiroshi Ujita, Yoshinori Nakadai, Takashi Ikeda, Masanori Naitoh.** Kyoto : s.n., Sept. 15-19 2003. GENES4/ANP2003: International conference on global environment and advanced nuclear power plants. p. 8.
47. **Japan, IAE.** *SAMPSON user manual theory*. Vol. 3.
48. **Jun Wang, Xin Li, Chris Allison, Judy Hohorst.** *Nuclear power plant design and analysis codes, development, validation and application* . s.l. : Woodhead Publishing, 2020.
49. **Hiroshi Ujita, Nobuhide Satoh, Masanori Naitoh, Masataka Hidaka, Noriyuki Shirakawa, Makoto Yamagishi.** Development of Severe Accident Analysis Code SAMPSON in IMPACT Project. *Journal of Nuclear Science and Technology*. 1999, Vol. 36, 11.
50. *Basic Models and verification study on fuel rod heat up and fission product release analysis modules in SAMPSON for the IMPACT project.* **Tadashi Morii, Hiroshi Ujita, Kazuyuki Katsuragi, Hidetoshi Karasawa.** Tokyo, Japan : s.n., Aprile 19-23 1999. ICONE .
51. **V. H. Ransom, et al.** RELAP5/MOD2 Code manual: code structure, system models and solution methods. s.l. : NUREG/CR-4312, 1985, Vol. 1.
52. **L. J. Siefken, C.M. Allison, M. P. Bohn, S. O. Peck.** FRAP-T6: a computer code for the transient analysis of oxide fuel rods. *Nuclear Engineering and Design*. April 1981, Vol. 88.

53. **Louis Baker Jr., Louis C. Just.** *Studies of metal-water reactions at high temperatures. III experimental and theoretical studies of the zirconium-water reaction.* Chemical Engineering and Applied Mathematics, Argonne National Laboratory . s.l. : ANL, May 1962.
54. **Nobuhide Satoh, Hiroshi Ujita, Kazumi Miyagi, Noriyuki Shirakawa, Hideki Horie, Katsuhiko Nakahara, Hiroshi Sasakawa.** Development of Molten Core Relocation Analysis Module MCRA in the Severe Accident Analysis Code in SAMPSON. *Journal of Nuclear Science and Technology.* 2020.
55. **A. Costa, M. E. Ricotti, H. Ninokata.** *Validation of the SAMPSON/MCRA code against CORA 18 experiment.* s.l. : Politecnico di Milano, A. A. 2013/2014.
56. **M. Pellegrini, M. Naitoh.** Three weeks analysis for the Fukushima Daiichi Unit 3 NPP by the SAMPSON code: contribution to the BSAF-2 project. *Nuclear Engineering and Design.* 2020, Vol. 366.
57. **C.D. Fletcher, R.R. Schultz.** *RELAP5/MOD3 code manual.* s.l. : NUREG/CR-5535, 1995.
58. **Hiroshi Ujita, Masataka Hidaka, Akira Susuki, Naoyuki Ishida.** Development of Debris Coolability Analysis module in Severe Accident Analysis code SAMPSON for IMPACT Project. *Journal of Nuclear Science and Technology.* October 1999, Vol. 36, 10, pp. 940-951.
59. **M. Hidaka, T. Fujii, T. Sakai.** Improvement of molten core–concrete interaction model in debris spreading analysis module with consideration of concrete degradation by heat. *Journal of Nuclear Science and Technology.* 2016, Vol. 53, 9.
60. **M. Di Giuli, M. Pellegrini, M. Naitoh.** *Study of molten corium-concrete interaction phenomena using SAMPSON code.* Tokyo : IAE, 2016.
61. **J. Meijerink, H. A. Vorst.** An iterative solution method for linear systems of which the coefficient matrix is a symmetric M-matrix. *Mathematics of Computation.* 1977, Vol. 31, 137.
62. **R. Benz, H. Schins.** Boiling fragmentation of molten stainless steel and copper in sodium. *Nuclear Engineering and Design.* 1982.
63. **H. Shins, F. S. Gunnerson.** Boiling and fragmentation behavior during sodium-fuel interaction. *Nuclear Engineering and Design.* 1986, 91.
64. **T. R. Johnson, J. R. Pavlik, L. Baker Jr.** *Post accident heat removal: large scale molten fuel-sodium interaction experiments.* s.l. : ANL-75-12, 1975.
65. *Fragmentation of molten core material by sodium.* **Chu, T. Y.** Lyon, France : Proceedings of the International Topic Meeting on LMFBR Safety, 1982.

66. *Pouring of 100-kg-Scale Molten UO₂ into Sodium*. **D. Magallon, H. Hohmann, H. Schins**. s.l. : Nuclear Technology, 1992, Vol. 98.
67. *Intermediate scale steam explosions phenomena: experiments and analysis* . **D. E. Mitchell, M. L. Corradini, W. W. Tarbell**. s.l. : NUREG/CR-2145, 1981.
68. *Fragmentation and Quench Behavior of Corium Melt Streams in Water*. **B. W. Spencer, K. Wang, C. A. Blomquist, L. M. McUmber, J. P. Schneider**. s.l. : NUREG/CR-6133, 1994.
69. *Experiments on the mixing of molten uranium dioxide with water and initial comparisons with CHYMES code calculations*. **M.K. Denham, A. P. Tyler, D. F. Fletcher**. s.l. : Nuclear Engineering and Design , 1994, Vol. 146.
70. **K. Sugiyama, F. Sotome, M. Ishikawa**. Thermal interaction in crusted melt jets with large-scale structures. *Nuclear Engineering and Design*. 1999, Vol. 189.
71. **W. Cherdron, F. Huber, A. Kaiser, W. Schuetz**. *ECO steam explosion experiments - Documentation and evaluation of experimental data*. s.l. : FZKA - 7011.
72. **D. Magallon, I. Huhtiniemi, H. Hohmann**. Lessons learnt from FARO/TERMOS corium melt quenching experiments. *Nuclear Engineering and Design*. 1998, Vol. 189.
73. **IAEA**. Thermophysical properties database of materials for light water reactors and heavy water reactors. 2006.
74. **Crowe, Clayton T**. *Multiphase flow handbook*. New York : Taylor and Francis Group, 2006.
75. **P. Di Marco, W. Grassi**. Overview and prospects of boiling heat transfer studies in microgravity. *International Symposium IN SPACE*. 1997.
76. **Rohsenow, W. M**. A method of correlating heat transfer data for surface boiling of liquids. *TRANS. ASME*. 1952, Vol. 74.
77. **Zuber, N**. Hydrodynamic aspects of boiling heat transfer. *PhD thesis*. 1959.
78. **IAE**. SAMPSON 1.6.1 user manual vol.2: input. 2016.
79. **K. Vierow, M. Naitoh, K. Nagano, K. Araki**. Development of the VESUVIUS code for steam explosions analysis part 1: Molten jet breakup modeling. *Japanese Multiphase Flow*. 1997, Vol. 2, 13.
80. **Schlichting, H**. *Boundary Layer Theory*. 1979, Vol. 7th edition.
81. **al., M. Burger et**. *Nuclear Engineering and Design*. 1995, Vol. 155.
82. **T. Moori, K. Araki, M. Naitoh, Y. Nakadai**. Benchamrk analysis of premixing phase of FCI experiment by the VESUVIUS code. *NURETH - 10*. 2003.

List of Figures

Figure 1.1: SAMPSON simulations without fragmentation model compared to experimental data.....	2
Figure 1.2: physical barriers for a typical nuclear reactor configuration	5
Figure 1.3: Temperature regimes for core meltdown.....	10
Figure 1.4: ASTEC modular structure	17
Figure 1.5: ASTEC and MELCOR simplified nodalization for primary and secondary circuits	18
Figure 1.6: MAAP nodalization for primary circuit	23
Figure 2.1: Global phenomena occurring during FCI	33
Figure 2.2: Jet breakup mechanism and regimes	35
Figure 2.3: experimental jet breakup length compared to Saito and Epstein – Fauske model.....	40
Figure 2.4: KHI evolution regimes.....	45
Figure 2.5: KHI stability plot.....	47
Figure 2.6: KHI stability plot including solidification effects	47
Figure 2.7: boiling curve for melt quenching process	49
Figure 2.8: Sketch of coolant jet impingement in fuel	60
Figure 2.9: single droplet analysis stages.....	62
Figure 3.1: Overview of SAMPSON modules	68
Figure 3.2: SAMPSON modules linking and data transfer	70
Figure 3.3: Outline of fission product behavior	71

Figure 3.4: Basic MCRA physical models	74
Figure 3.5: Fukushima THA nodalization based on RELAP5/MOD3 code.....	76
Figure 3.6: Onset of SAMPSON modules in function of accident evolution time.....	77
Figure 3.7: Debris falling and spreading phenomena in the lower head	78
Figure 3.8: Phenomena modeling in DSA module	78
Figure 3.9: DSA computational cells and moving boundaries for debris spreading ..	79
Figure 3.10: examples of PWR containment cells and thermal hydraulics models.....	81
Figure 4.1: FARO test facility external view	88
Figure 4.2: FARO facility with TERMOS vessel.....	90
Figure 4.3: FARO facility with FAT vessel.....	91
Figure 4.4: Cake formed in L-19 test (a) seen from the top (b) seen from below at contact with bottom plate	93
Figure 4.5: Cake formed in L-14 test	93
Figure 4.6: Pressure increase in FARO L-14 experiment from -5s up to 40 s.....	98
Figure 4.7: Pressure increase highlighting melt contact with water and bottom plate	98
Figure 4.8: Pressure increase rate in FARO L-14 experiment	99
Figure 4.9: Water level swell in FARO L-14 experiment	99
Figure 4.10: Temperature increase at bottom plate	100
Figure 5.1: Detailed debris coolability model meshes and coordinates	106
Figure 5.2: Simplified coolability model coordinates.....	106
Figure 5.3: RPV mesh discretization in DCA module.....	107
Figure 5.4: Debris mesh discretization in DCA module	108
Figure 5.5: RPV lower head temperature distribution for DCA stand-alone.....	110
Figure 5.6: Debris spreading and temperature evolution before restart.....	111
Figure 5.7: Debris spreading and temperature evolution at RPV melt time	111
Figure 5.8: Debris temperature for FARO data input and Fukushima vessel geometry	113
Figure 5.9: DCA stand-alone results.....	114
Figure 5.10: Fukushima nodalization in RELAP/MOD3	115

Figure 5.11: FARO test vessel geometry.....	116
Figure 5.12: RELAP 8-volumes input for FARO vessel geometry	118
Figure 5.13: RELAP 2-volumes input for FARO vessel geometry	119
Figure 5.14: Temperature analysis in THA stand-alone	119
Figure 5.15: Pressure analysis in THA stand-alone	120
Figure 5.16: Coupling pressure result (green) compared to experimental one (blue)	122
Figure 5.17: Nukiyama boiling curve	123
Figure 5.18: Comparison between SAMPSON calculation for pool boiling and literature at atmospheric pressure	126
Figure 5.19: Pool boiling calculations at 5 MPa pressure	127
Figure 5.20: Pressure comparison between THA and analytical evaluation.....	129
Figure 5.21: Final result of DCA-THA coupling without fragmentation model comparing experimental, analytical and computational pressure.....	129
Figure 5.22: Fragmentation model heat flux contributions.....	138
Figure 5.23: Fragmentation model preliminary results	139
Figure 5.24: Debris visualization in the lower head after fragmentation.....	140
Figure 5.25: Fragmentation model results for trivial implementation	142
Figure 5.26: Sketch of implementation philosophy for model update	144
Figure 5.27: Pressure trend comparison between experimental and newly implemented model results	145
Figure 5.28: VESUVIUS geometry modeling for molten jet.....	147
Figure 5.29: Particles break-off from molten jet due to KHI	148

List of Tables

Table 1.1: Defence in depth levels.....	5
Table 1.2: defence in depth levels.....	13
Table 1.3: ASTEC modules overview	19
Table 1.4: Severe accident codes comparison.....	26
Table 1.5: Experimental programs for code validations	27
Table 4.1: Experimental works for oxide/sodium interaction.....	84
Table 4.2: Experimental works for metal/sodium interaction.....	85
Table 4.3: Experimental works for metal/water interaction.....	86
Table 4.4: Experimental works for oxide/water interaction	87
Table 4.5: Comparison of L-series test.....	91
Table 4.6: FARO L-14 experimental conditions and results.....	95
Table 5.1: Mesh implementation for DCA stand-alone	109
Table 5.2: FARO L-14 geometry and boundary conditions.....	117

List of Symbols

Variable	Description	SI unit
Bo	Bond number	–
c_p	Specific heat	$\frac{J}{Kg K}$
C_{sf}	Rohsenow surface-liquid coefficient	–
d_B	Diameter of broken-up particles	m
D_j	Jet diameter	m
E_o	Entrainment coefficient	–
F	Shape factor	–
Fr	Froude number	–
g	Gravitational acceleration	$\frac{m}{s^2}$
h	Heat transfer coefficient	$\frac{W}{m^2 K}$
Δh_{lg}	Specific vaporization latent heat	$\frac{J}{Kg}$

H_B	Free fall distance in water	m
H_l	Water level	m
k	Wave number	m^{-1}
K	Thermal conductivity	$\frac{W}{m^2 K}$
L	Characteristic length	m
L_{brk}	Breakup length	m
$\frac{L_{brk}}{D_j}$	Non dimensional jet breakup length	m
L_j	Jet length	m
M_j	Jet mass flow rate	$\frac{Kg}{s}$
N	Number of particles	–
N_B	Generation rate of particles	$\frac{number}{s}$
N_{layer}	Number of layers	–
Pr	Prandtl number	–
q''	Heat flux	$\frac{W}{m^2}$
q''_{CHF}	Critical heat flux	$\frac{W}{m^2}$
Q	Heat transfer rate	W
Re	Reynolds number	–
$t_{B\ stay}$	Particles' residence time in water pool	s

$t_{discharge}$	Time for molten material slumping	s
Δt	Computational time step	s
T	Temperature	K
v	Velocity	$\frac{m}{s}$
We	Weber number	—
γ_t	KHI temporal growth rate	
γ_y	KHI spatial growth rate	
ε	Radiation absorption rate	—
η	Wave function	m
η_0	Wave amplitude	m
λ	Wavelength	m
μ	Viscosity	$\frac{Kg}{m\ s}$
ρ	Density	$\frac{Kg}{m^3}$
σ	Surface tension	$\frac{N}{m}$
σ_{SB}	Stefan-Boltzmann constant	$\frac{W\ K^4}{m^2}$
ω	Frequency	s^{-1}

List of Acronyms

Acronym	Description
ACC	Accumulator Module
ACM	Analysis Control Module
AEAT	Atomic Energy Authority for Technology
ALARP	As Low As Reasonably Possible
ANL	Argonne National Laboratory
ASTEC	Accident Source Term Evaluation Code
BUR	Burn module
CAV	Cavity module
CEA	Commissariat l'Energie Atomique
CFD	Computational Fluid Dynamics
CND	Condenser module
COR	Core module
CVH	Control Volume Hydrodynamics
CVPA	Containment Vessel Phenomena Analysis
CWT	Critical Weber Theory
CVT	Control Volume Thermodynamics
DBA	Design by Basis Accident

DCA	Debris Coolability Analysis
DCH	DeCay Heat
DCRA	Debris-Concrete Reaction Analysis module
DSA	Debris Spreading Analysis
ECCS	Emergency Core Cooling System
EPRI	Electric Power Research Institute
ESF	Engineered Safety Features
FARO	Furnace And Release Oven
FCI	Fuel – Coolant Interaction
FCL	Fan Cooler
FDI	Fuel Dispersal
FPRA	Fission Products Release from fuel Analysis
FPTA	Fission Products Transport Analysis
FRHA	Fuel Rod Heat up Analysis module
FL	Flow path
FP	Fission Product
GRS	Global Research for Safety
HS	Heat Structures
HIS	Heat Interactive Structures
IAE	Institute of Applied Energy
IAEA	International Atomic Energy Agency
ICS	Isolation Condenser System

IDCOR	Industry Degraded Core Rulemaking
IMPACT	Integrated Modular Plant Analysis and Computing Technology
INEL	Idaho National Engineering Laboratory
IRSN	Institut de Radioprotection et de Sûreté Nucléaire
JRC	Joint Research Centre
KHI	Kelvin – Helmholtz Instabilities
KHT	
KIT	Karlsruhe Institute of Technology
LOCA	Loss Of Coolant Accident
LWR	Light Water Reactor
MAAP	Modular Accident Analysis Program
MCCI	Molten Core Concrete Interaction
MCRA	Molten Core Relocation Analysis
MELCOR	Methods for Estimation of Leakages and Consequences of Releases
MP	Material Properties
NCG	Non-Condensable Gas
NPP	Nuclear Power Plant
NUPEC	Nuclear Power Engineering Corporation
ORNL	Oak Ridge National Laboratory
PAR	Passive Autocatalytic hydrogen Recombiner
PCCS	Passive Containment Cooling System

PVC	Primary Containment Vessel
PWR	Pressurised Water Reactor
RCS	Reactor Cooling System
RN	RadioNuclide
RPV	Reactor Pressure Vessel
RTI	Rayleigh – Taylor Instabilities
SAMPSON	Severe Accident analysis code with Mechanistic, Parallelized Simulations Oriented towards Nuclear field
SARNET	Severe Accident Research NETwork
SEM	Scanning Electron Microscopy
SMAC	Simplified Marker And Cell
SNL	Sandia National Laboratories
SPR	containment SPRays
TEPCO	Tokyo Electric Power Company
THA	Thermal Hydraulic Analysis
TMI	Three Mile Island
USNRC	United States Nuclear Regulatory Commission

Ringraziamenti

Desidero ringraziare innanzitutto il Professor Antonio Cammi, relatore di questa tesi, non solo per avermi dato la possibilità di concludere questo percorso con soddisfazione, ma anche per essere stato una figura di riferimento nei momenti di difficoltà. Non è scontato essere ascoltati, consigliati, e non essere considerati un mero numero: la ringrazio infinitamente per tutto.

Vorrei inoltre ringraziare il Professor Hisashi Ninokata e Naitoh San, direttore del gruppo di ricerca, analisi e decommissioning di Fukushima in IAE, per l'enorme opportunità offertami a Tokyo in IAE, sia in termini lavorativi che di crescita personale; un ringraziamento anche a tutti i colleghi e ai dirigenti dei singoli gruppi di ricerca di IAE, per avermi supportata, aiutata e guidata durante tutto l'arco del mio lavoro a Tokyo.

Ai miei genitori: devo tutto a voi. Ci siete sempre stati e ci sarete sempre, nei momenti di gioia ma soprattutto nelle difficoltà: avete sempre creduto in me e nelle mie capacità, supportandomi ogni singolo giorno. Come vi ho già detto più volte, penso davvero di essere fortunata ad avere dei genitori come voi al mio fianco, e se un giorno riuscissi a darvi anche solo la metà del supporto e dell'amore che mi avete dato voi, sarei già soddisfatta. Siete la lanterna luminosa che cerco nei momenti in cui tutto sembra buio pesto, e il conforto di vedere quella lanterna sempre accesa è inimmaginabile. Dal profondo del mio cuore, il più grande ringraziamento va a voi.

Grazie anche a tutta la mia famiglia che mi ha sempre sostenuta e incoraggiata, in particolare al miè nunon Arturo che, nonostante "una dottoressa che non può dare le medicine, non è mica una brava dottoressa", è sempre stato orgoglioso di me. Grazie a Luca, per esserci sempre stato e avermi supportata (e sopportata) soprattutto nel rush finale. Nelle situazioni in cui io perdo le speranze sbinnandola come Seb,

tu invece riuscivi a fare delle magie come Charles riportandola in pista: tanto, alla fine, quel che contava per noi era il risultato di squadra, e la nostra scuderia 'TRIGA racing' ha finalmente vinto. Grazie quindi per avermi sostenuta nei momenti di sconforto in cui volevo gettare la spugna, e per l'eccellente strategia ai box: non so se sarei qui oggi se non fosse stato per te.

Grazie alla Frafe: amiche come te sono rare da trovare e io sono grata di averti incontrata. Grazie per le risate, per le giornate passate in architettura e per la forza che mi hai dato per andare avanti e non mollare. Ovunque ci troveremo, anche se lontane, saremo sempre due rane braccate con il Luminol.

Un ringraziamento alla gang degli impiantisti: Fuma e Silva alfiere dell'uomo del Giappone, Pincio l'imperatore del giro pizza mai sconfitto in battaglia, MikySala, Ste, Pero, Greg, Don Matteo, Ale e Buu (il dio del sole). Con voi ho passato le giornate più divertenti della mia vita, siete riusciti ad alleggerire ogni singolo momento riempiendolo di risate. L'ora esatta, l'inganno della Cina e i cachi del TRIGA sono ricordi indelebili che porterò sempre nel cuore. Una menzione speciale a Masche, il mio 'banco-compagno', vincitore indiscusso della MikySalaCup durante le ore in cui era necessaria una formazione di combattimento a falange oplitica.

Grazie a tutti gli amici del Gypsyan Club, in particolare ad Ermanno, responsabile dell'ufficio sinistri sempre pronto a sollevarmi il morale, Emanuele e Anna, che tra la fornitura di santini di Alessia per passare gli esami e supporto psicologico sono stati un punto fermo negli ultimi anni, e infine Manuel e Amina per esserci sempre stati, pronti a farmi, con garbo, il pieno di Spritz e confortandomi in qualsiasi situazione. Grazie agli amici del CESNEF e a tutti quelli che non ho avuto il tempo di ringraziare ma che ci sono sempre stati durante questo lungo e tempestoso percorso.

E infine a te, che manchi da ormai 23 anni, ma sei sempre stata al mio fianco: grazie.

